Estruturas de Domínios: Técnicas Experimentais e Resultados

Antonio Domingues dos Santos
Laboratório de Materiais Magnéticos
IFUSP

adsantos@if.usp.br

- Introdução e teoria (algumas generalidades)

-Técnicas de observação de domínios: Bitter, MOKE, PEEM, SEMPA, Microscopia Lorentz, MFM, SP-STM, SNOM, SPLEEM, …

-Micromagnetismo (simulações)

- SNOM+MOKE

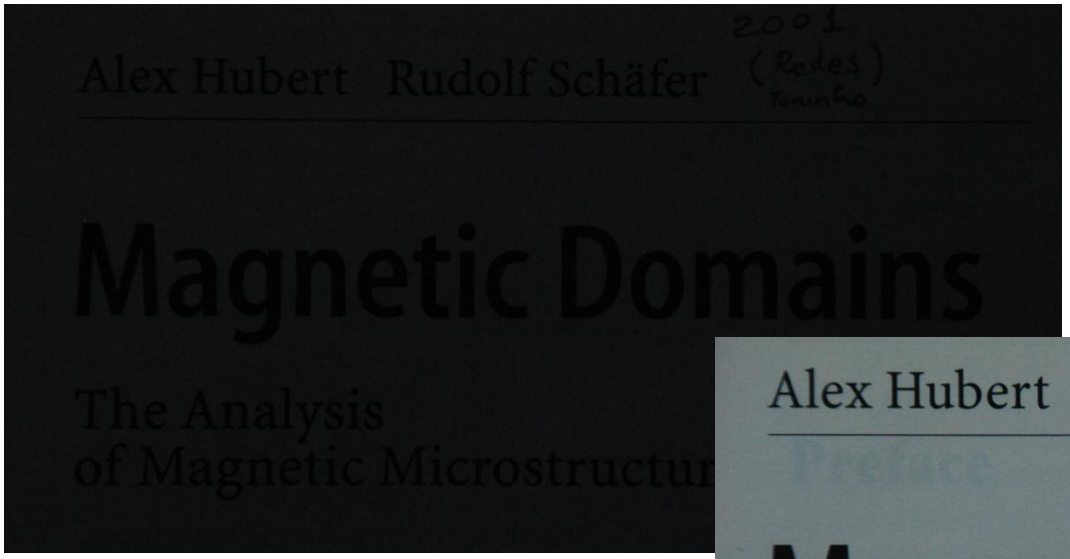
Alex Hubert Rudolf Schäfer
2001
(Redes)
Magnetic Domains
The Analysis
of Magnetic Microstructur

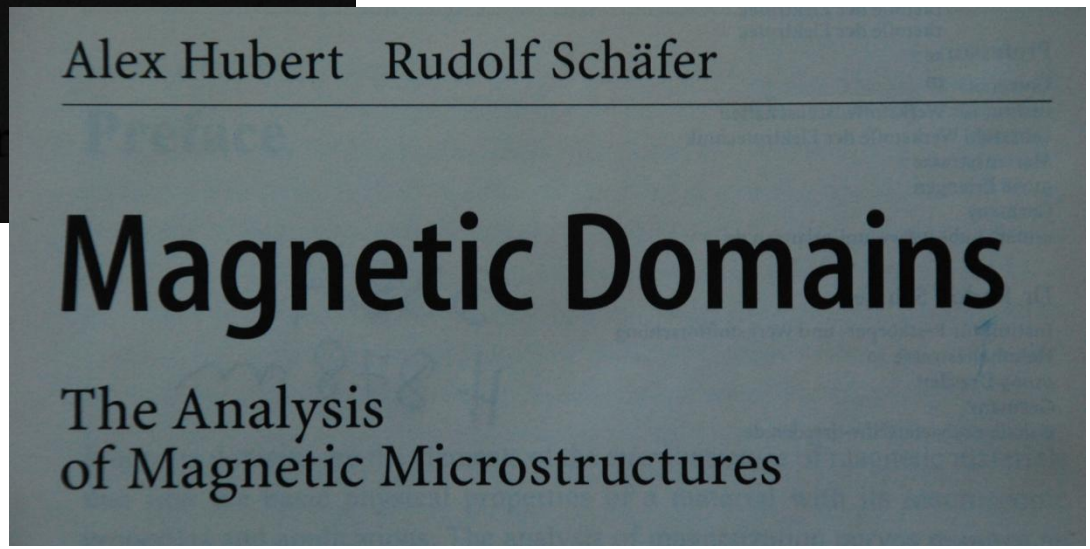
Alex Hubert Rudolf Schäfer
Preface
Magnetic Domains
The Analysis
of Magnetic Microstructures

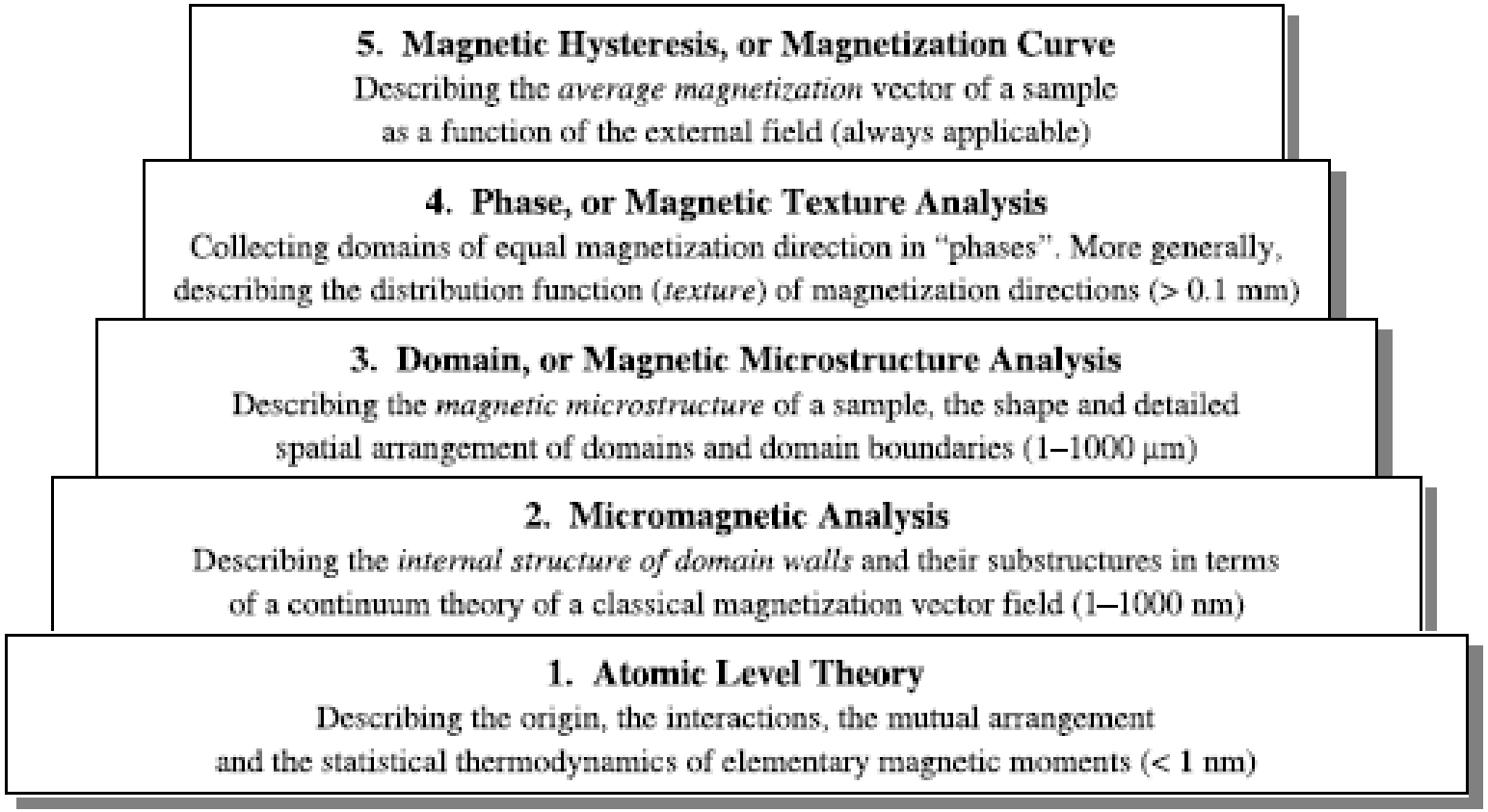

Fig. 1.5. The hierarchy of descriptive levels of magnetically ordered materials. The values in parenthesis indicate the sample dimensions for which the different concepts are applicable

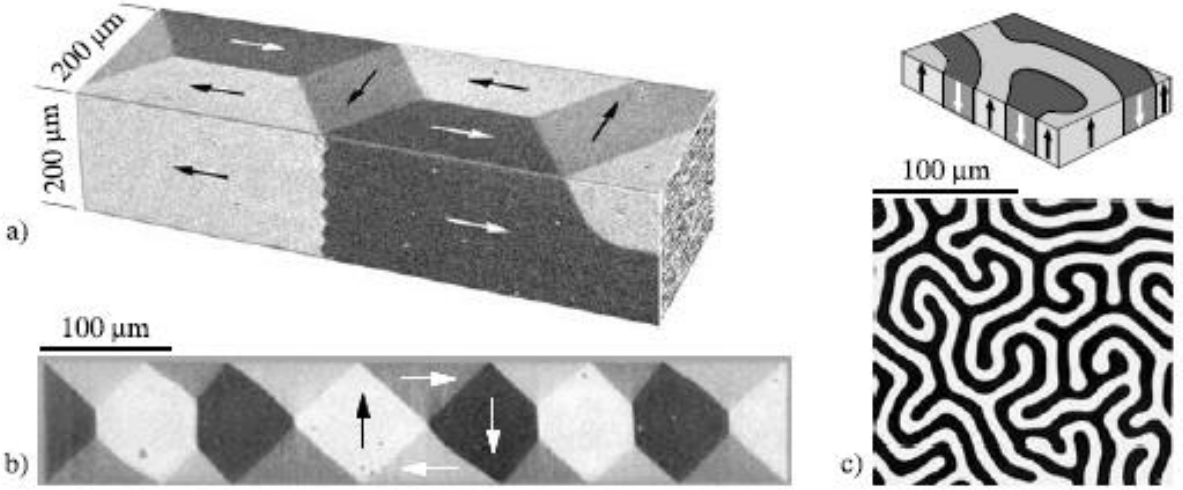

Fig. 1.1. Domains observed with magneto-optical methods on homogeneous magnetic samples. (**a**) Images from two sides of an iron whisker, combined in a computer to simulate a perspective view (sample courtesy *R.J. Celotta*, NIST). (**b**) Thin film NiFe element (thickness 130 nm) with a weak transverse anisotropy (sample courtesy *M. Freitag*, Bosch). (**c**) Faraday effect picture of domains in a single-crystal garnet film with perpendicular anisotropy, together with a schematic of the magnetization

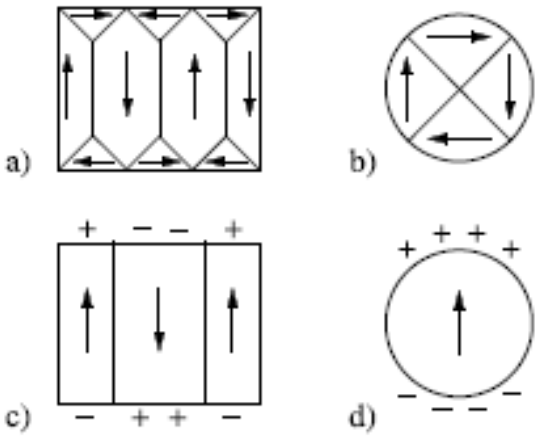

Fig. 1.4. The more or less flux-closed patterns of low-anisotropy cubic particles (**a**) and (**b**), compared to the open domain structures for high-anisotropy uniaxial particles (**c**) and (**d**)

Na teoria micromagnética em geral a energia livre (E) inclui os termos locais:

direção da magnetização

$$\vec{m} = \vec{J} / J_{sat}$$

-energia de anisotropia magnética
(cristalina, uniaxial induzida, "exchange bias", superfície e interfaces)

-energia de troca

$$E_x = A\int \left(\vec{\nabla}\vec{m}\right)^2 dV$$

exchange stifness costant

-energia Zeeman

$$E_H = -J_s \int (\vec{H}_{ext} \cdot \vec{m}) dV$$

e, não locais:

direção da magnetização

$$\vec{m} = \vec{J} / J_{sat}$$

- energia magnetostática desmagnetizante

$$E_d = \frac{1}{2}\mu_0 \int_{tudo} \vec{H}_d^2 dV = -\frac{1}{2} \int_{amostra} (\vec{H}_d \cdot \vec{J}) dV$$

$$onde: \vec{\nabla} \cdot H_d = -\vec{\nabla} \cdot \vec{J} / \mu_0$$

- energia magnetoelástica¨(materiais cúbicos, hexagonais, uniaxiais e isotrópicos e tensões internas e externas)

cte de magnetostricção

deformação

$$E_{me} \alpha (\lambda, \varepsilon, \cos\theta)$$

Complicado ! ! !

Energia livre total:

$E_{tot}=\int$(exchange + anisotropia + Zeeman + desmagnetizante + magnetoelástica)dV

Campo efetivo: $\mathbf{H_{eff}} = -\partial E_{tot}/\partial \mathbf{J}$, em cada ponto do espaço.

A orientação da magnetização é definida pela equação de Landau-Lifshitz-Gilbert:

$$\partial \mathbf{m}/\partial t = -\gamma \mathbf{m}\times\mathbf{H_{eff}} - \alpha(\mathbf{m}\times\mathbf{m}\times\mathbf{H_{eff}})$$

onde γ é o fator giromagnético, α é a constante de amortecimento e $\mathbf{m}\times\mathbf{H_{eff}}$ é um torque, que no equilíbrio deve ser nulo em cada ponto do espaço.

Energia livre total:

$E_{tot}=\int$(exchange + anisotropia + Zeeman + desmagnetizante + magnetoelástica)dV

Energy term	Coefficient	Definition	Range
Exchange energy	A [J/m]	Material constant	$10^{-12}-2\cdot10^{-11}$ J/m
Anisotropy energies	K_u, K_c ... [J/m^3]	Material constants	$\pm(10^2-2\cdot10^7)$ J/m^3
External field energy	$H_{ex}\,J_s$ [J/m^3]	H_{ex} = external field J_s = saturation magnetization	Open, depending on field magnitude
Stray field energy	K_d [J/m^3]	$K_d = J_s^2/2\,\mu_0$	$0-3\cdot10^6$ J/m^3
External stress energy	$\sigma_{ex}\lambda$ [J/m^3]	σ_{ex} = external stress λ = magnetostriction constant	Open, depending on stress magnitude
Magnetostrictive self energy	$C\,\lambda^2$ [J/m^3]	C = shear modulus	$0-10^3$ J/m^3

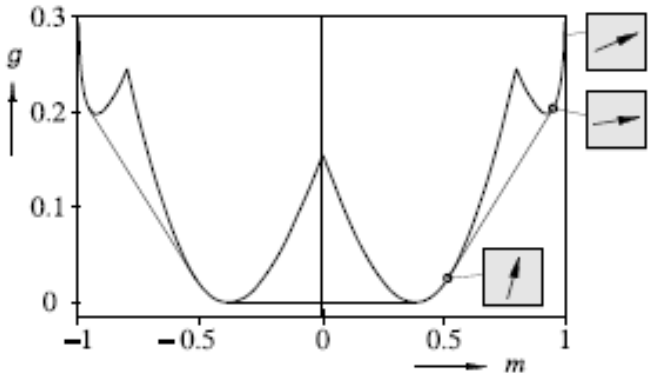

Fig. 3.17. The effective anisotropy energy g as a function of m, the magnetization component along the angle η_h. Of the two possible branches, only the lower energy branch is plotted for every value of m. The chosen parameters are $Q_{c1} = 1$, $Q_{u1} = 0.2$ and $\eta_h = \pi/8$

Dependência com o tamanho

Em função da diminuição do tamanho, temos:

- Organização em multidomínios magnéticos
- Após um certo volume limite V_1 e até um volume V_2 ($V_1 > V_2$) as partículas não formam mais domínios magnéticos e se comportam com um único domínio. Estas partículas são chamadas de *Monodomínios Magnéticos*.
- Para volumes menores que V_2 a partícula se comporta como um material paramagnético, porque o momento magnético da partícula pode variar termicamente. Isto é conhecido como *Superparamagnetismo* e depende da forma da partícula e das anisotropias da mesma.

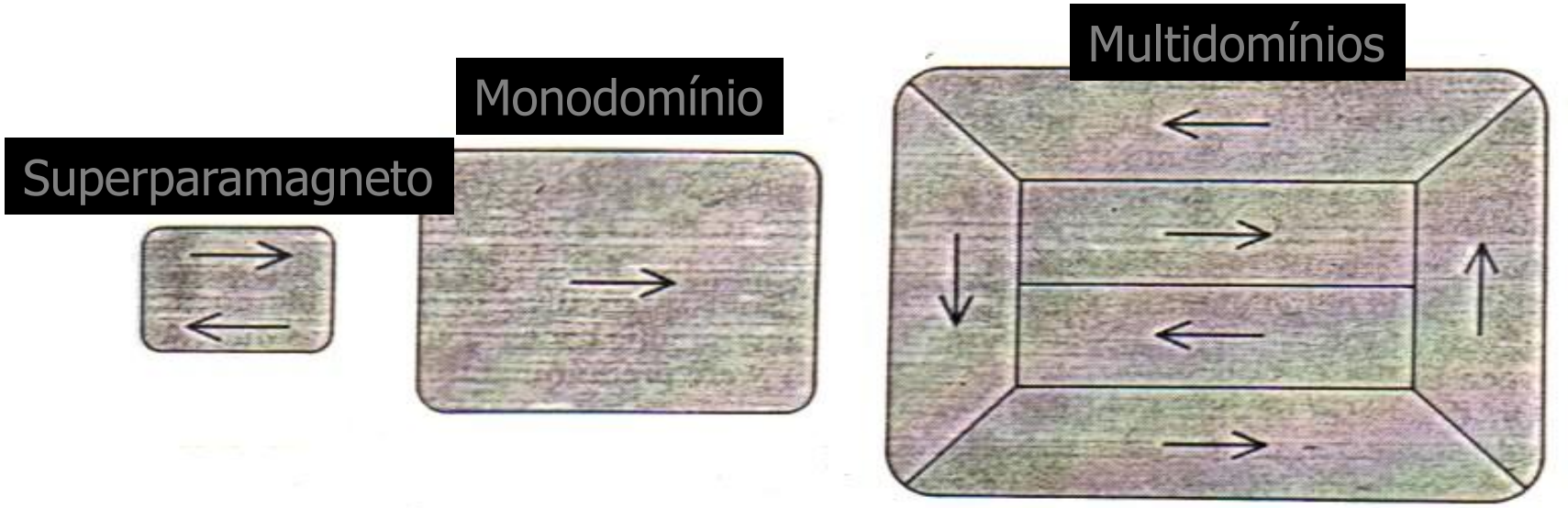

Parede de domínios

Bloch e Néel

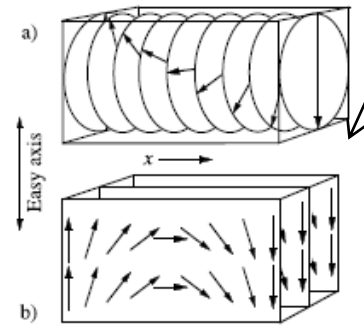

Fig. 3.53. The rotation of the magnetization vector from one domain through a 180° wall to the other domain in an infinite uniaxial material. Two alternate rotation modes are shown: the optimum mode, which is called the *Bloch* wall (**a**), as compared to the *Néel* wall (**b**), which is less favourable here but can be preferred in thin films and in applied fields. For both modes the opposite rotation is equally possible

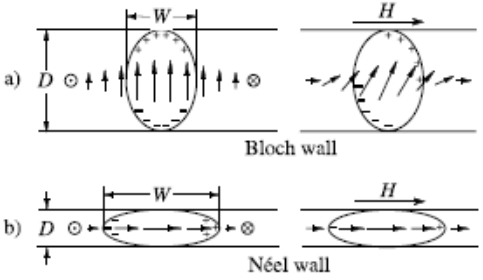

Fig. 3.72. Néel's view of domain walls in thin films. The cross-sections indicate the magnetic charges with and without an external field

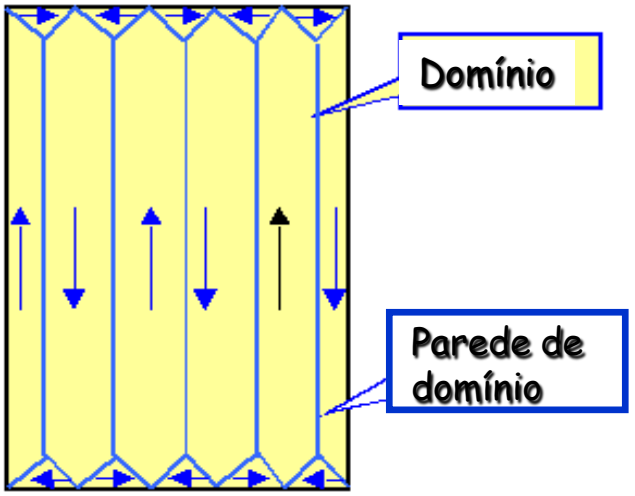

(C) Wall Widths. As demonstrated for example in (3.110), domain walls form a *continuous* transition between two domains. For this reason there can be no unique definition of a domain wall width. The classical definition introduced by *Lilley* [633] is based on the slope of the magnetization angle $\varphi(x)$, as shown in Fig. 3.55. Its value is $W_L = \pi\sqrt{A/K}$ in our example. In another definition, also indicated in this figure, the slope of the magnetization component $\sin\varphi$ in the origin is considered. It leads to $W_m = 2\sqrt{A/K}$.

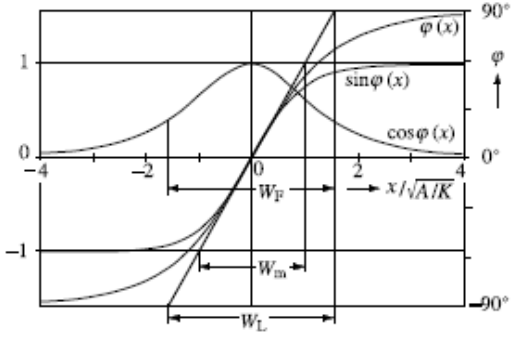

Fig. 3.55. The calculated wall profile of a 180° Bloch wall and different wall width definitions (see text)

Espessura da parede $\alpha\sqrt{A/K}$

Regras de Van den Berg para materiais moles

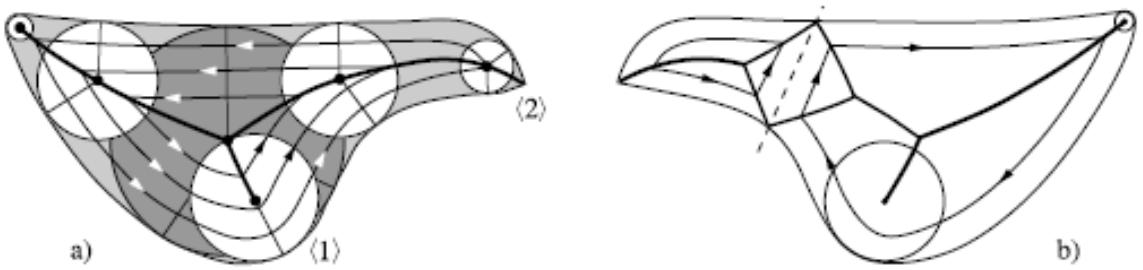

Fig. 3.22. (**a**) Van den Berg's construction of a stray-field-free planar magnetization pattern in a simply connected soft magnetic film element. (**b**) A more complicated variant obtained by introducing a virtual cut along the *dashed line*

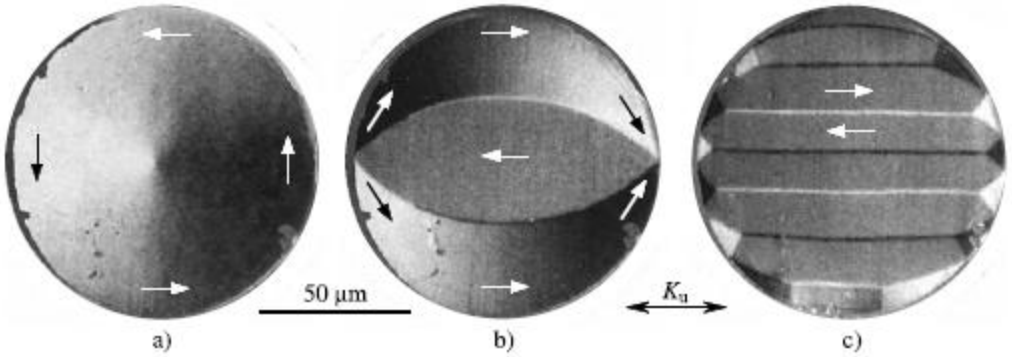

Fig. 3.29. A disk-shaped thin film element displays an isotropic magnetization pattern (**a**) following van den Berg's principles. A compressive stress introduces anisotropy (**b**, **c**) [591]. The domain patterns were brought to equilibrium by demagnetization in an alternating field oriented parallel to the stress-induced easy axis (**b**) and perpendicular to it (**c**). Although the resulting domain pattern depends on the demagnetization history, both (**b**) and (**c**) can be classified as domain patterns in the classical sense, in contrast to (**a**). The sample is a nanocrystalline iron-Permalloy multilayer system of 300 nm total thickness behaving like a single film [597]. The images were taken with the magneto-optical Kerr effect with a vertical sensitivity direction

- Círculos tangentes às paredes definem as posições das paredes.
- As linhas de campo devem ser paralelas às bordas.

Caracterização dos Materiais

Energia / Momento Matéria → Fótons(luz) Íons Átomos Elétrons Neutrons Prótons → **Propriedade a ser caracterizada** → Fótons (luz) Elétrons Íons Átomos Neutrons Prótons → Energia / Momento Matéria

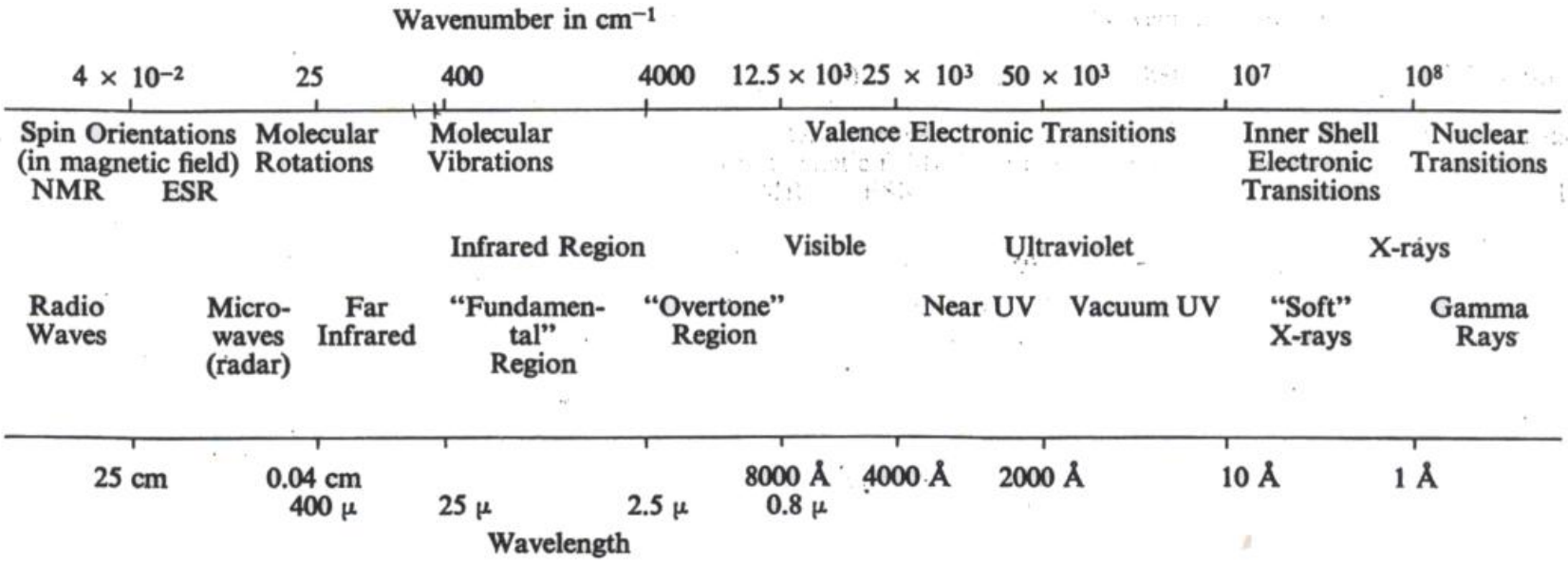

Usa microscopia ótica com polarização e uma suspensão coloidal de partículas magnéticas (ferro-fluido).

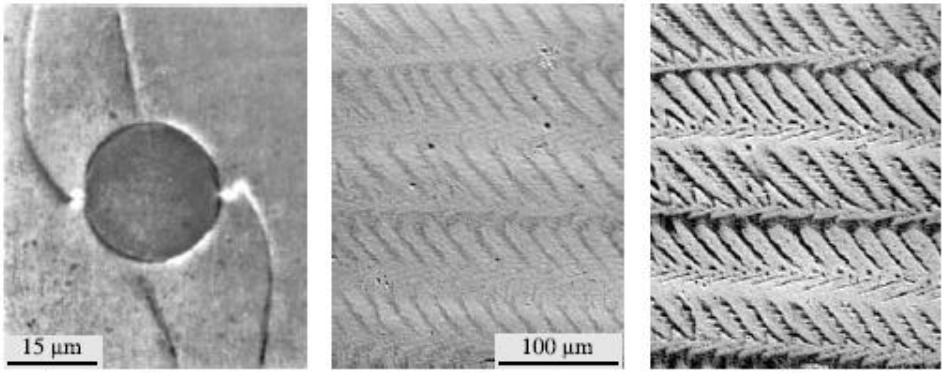

Fig. 2.1. (**a**) Domains in an ion-implanted garnet layer made visible by Ferrofluid® (courtesy *D.B. Dove*, IBM Yorktown Heights [54]). The circular shape is unimplanted. (**b**, **c**) Stress-induced domains on a $Ni_{55}Fe_{45}$ crystal revealed by Lignosite FML®. A perpendicular field of 1.5 kA/m was applied in (**c**) to improve the contrast of the same pattern. The NiFe crystal has ⟨100⟩ easy directions and a near (100) surface

Técnica de Bitter

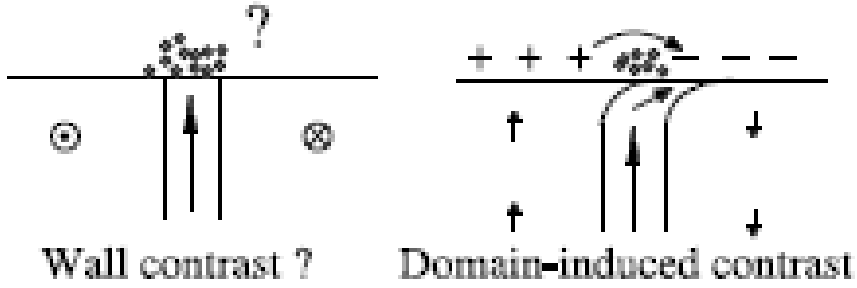

Efeitos Kerr magnetoóticos

Como obtemos o sinal magnetoóptico?

Efeito Kerr magnetoóptico (MOKE - *Magneto-optical Kerr Effect*): é a dependência da polarização ou da intensidade da luz refletida com a magnetização apresentada pela superfície. Há três tipos de Efeito Kerr:

- **Kerr Polar:** incidência normal, qualquer polarização.
- **Kerr Longitudinal:** sensível a magnetização paralela tanto a superfície de reflexão quanto ao plano de incidência da luz.
- **Kerr Transversal:** polarização é paralela ao plano luminoso.

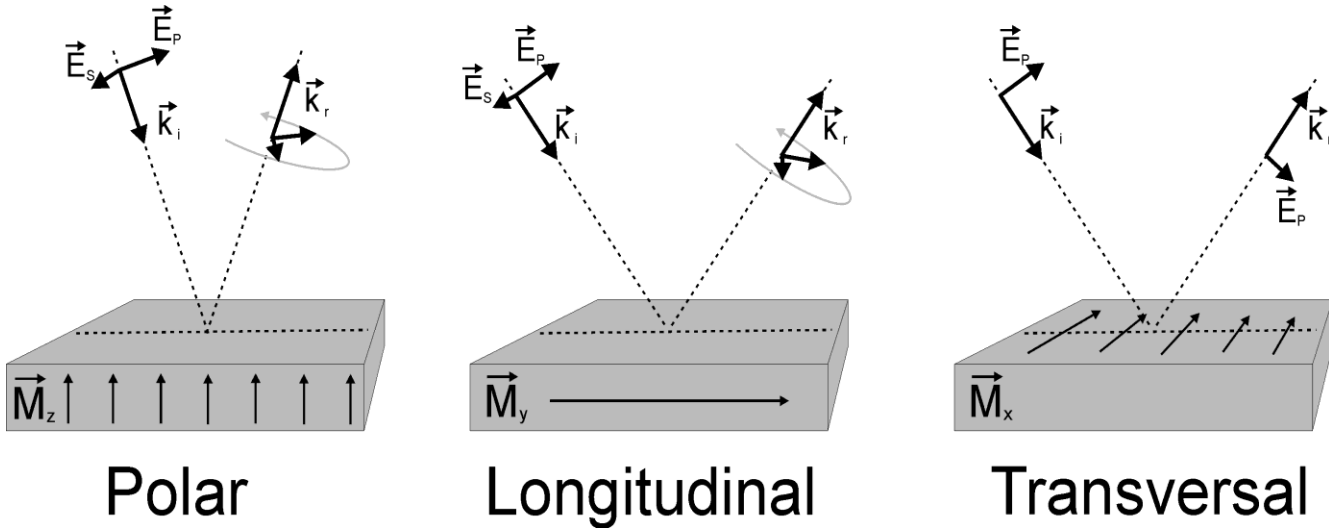

EFEITOS KERR MAGNETOÓTICOS

- Ondas planas em meios metálicos

$$\vec{k}*(\vec{k}*\vec{E}) = -\frac{\omega^2}{c^2}\hat{\varepsilon}\vec{E}$$

- Tensor Permissividade

$$\hat{\varepsilon} = \begin{pmatrix} \varepsilon & -iQ\varepsilon m_z & iQ\varepsilon m_y \\ iQ\varepsilon m_z & \varepsilon & -iQ\varepsilon m_x \\ -iQ\varepsilon m_y & iQ\varepsilon m_x & \varepsilon \end{pmatrix}$$

$$r_{pp} = \frac{n_2\cos\theta_1 - n_1\cos\theta_2}{n_2\cos\theta_1 + n_1\cos\theta_2} + \frac{2in_1n_2\cos\theta_1 sen\theta_2 m_x Q}{(n_2\cos\theta_1 + n_1\cos\theta_2)^2}$$

- Matriz de Fresnel

$$\begin{pmatrix} E_p^r \\ E_s^r \end{pmatrix} = R_F \begin{pmatrix} E_{op} \\ E_{os} \end{pmatrix}$$

$$r_{ss} = \frac{n_1\cos\theta_1 - n_2\cos\theta_2}{n_1\cos\theta_1 + n_2\cos\theta_2}$$

$$r_{ps} = -\frac{in_1n_2\cos\theta_1(m_y sen\theta_2 + m_z\cos\theta_2)Q}{\cos\theta_2(n_2\cos\theta_1 + n_1\cos\theta_2)(n_1\cos\theta_1 + n_2\cos\theta_2)}$$

$$R_F = \begin{pmatrix} r_{pp} & r_{ps} \\ r_{sp} & r_{ss} \end{pmatrix}$$

$$r_{sp} = \frac{in_1n_2\cos\theta_1(m_y sen\theta_2 - m_z\cos\theta_2)Q}{\cos\theta_2(n_2\cos\theta_1 + n_1\cos\theta_2)(n_1\cos\theta_1 + n_2\cos\theta_2)}$$

EFEITOS KERR MAGNETOÓTICOS

- Expressão geral polarização p

$$\frac{\Delta R}{\sqrt{R}} = (e^{i\theta_p} A^* n_2^* \sin^* \theta_2 + e^{-i\theta_p} A n_2 \sin\theta_2) m_x Q \cos\theta_a +$$
$$-[(e^{i\theta_p} B^* n_2^* \sin^* \theta_2 + e^{-i\theta_p} B n_2 \sin\theta_2) m_y +$$
$$+ (e^{i\theta_p} B^* n_2^* \cos^* \theta_2 + e^{-i\theta_p} B n_2 \cos\theta_2) m_z] Q \sin\theta_a$$

polarização s

$$\frac{\Delta R}{\sqrt{R}} = +[(e^{i\theta_s} B^* n_2^* \sin^* \theta_2 + e^{-i\theta_s} B n_2 \sin\theta_2) m_y +$$
$$-(e^{i\theta_s} B^* n_2^* \cos^* \theta_2 + e^{-i\theta_s} B n_2 \cos\theta_2) m_z] Q \cos\theta_a$$

Efeitos Kerr magnetoóticos

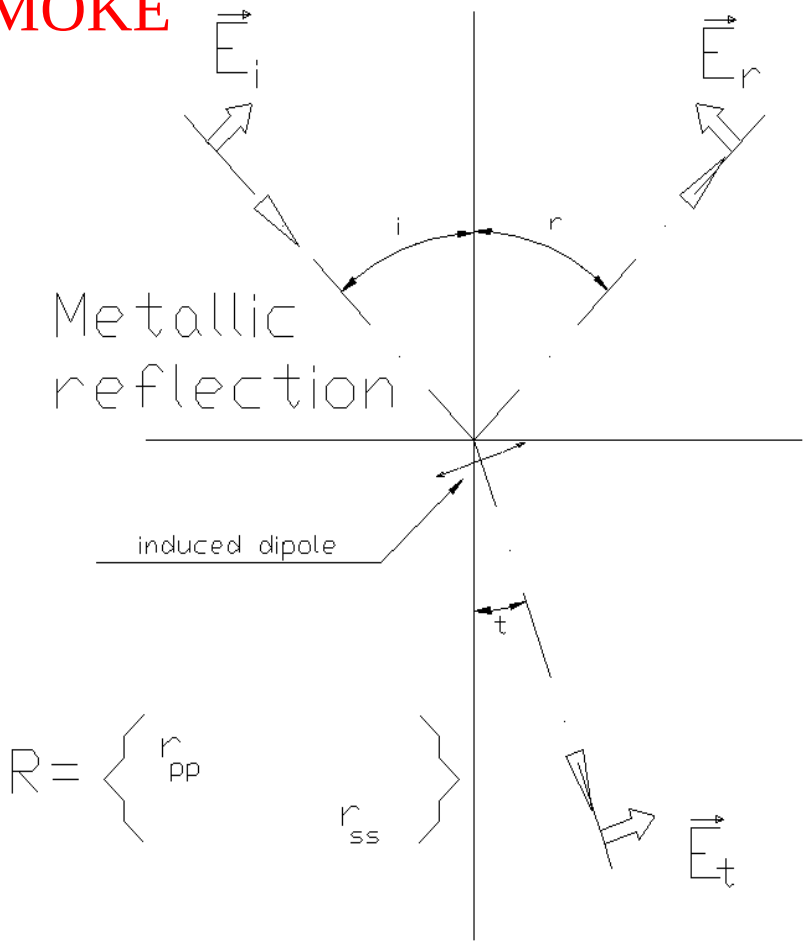

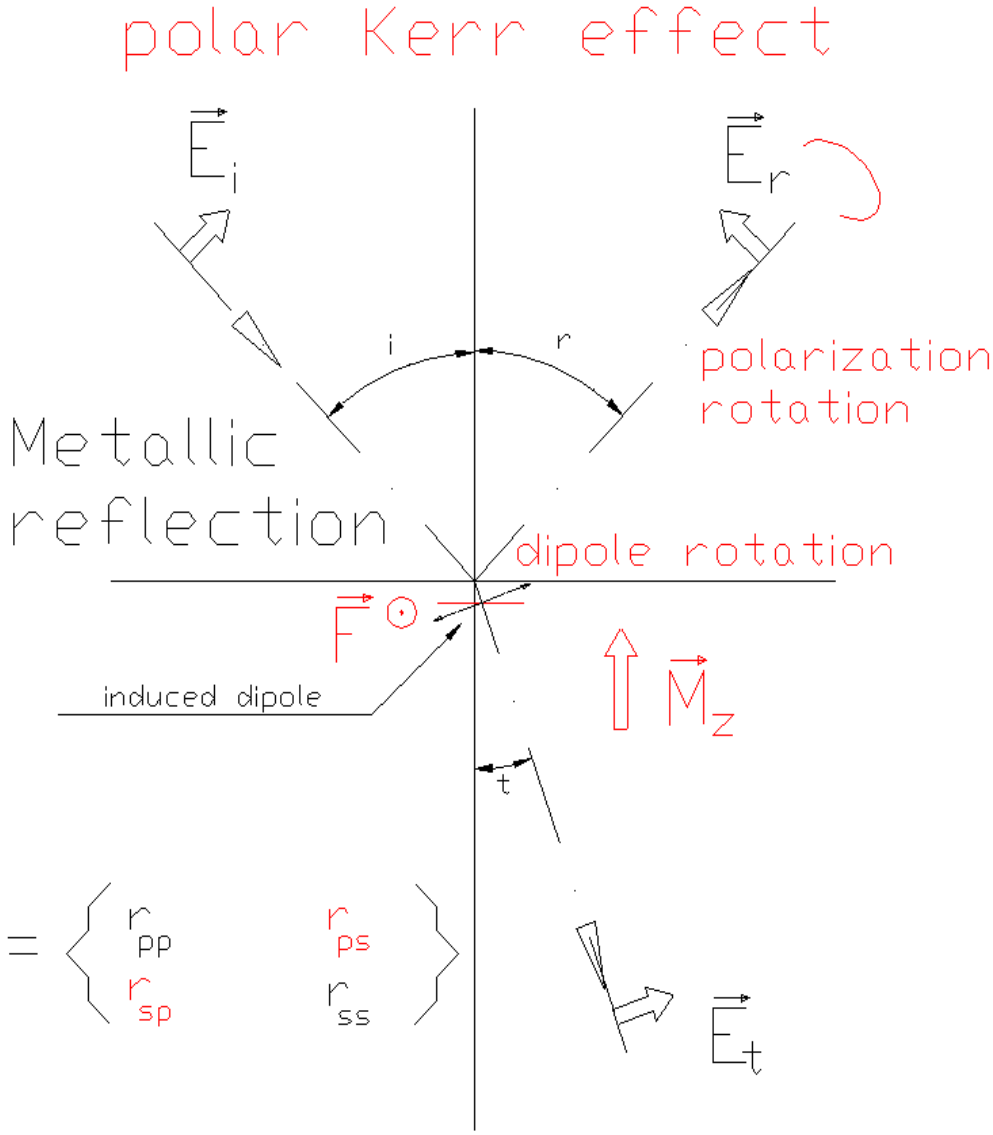

Efeitos Kerr magnetoóticos

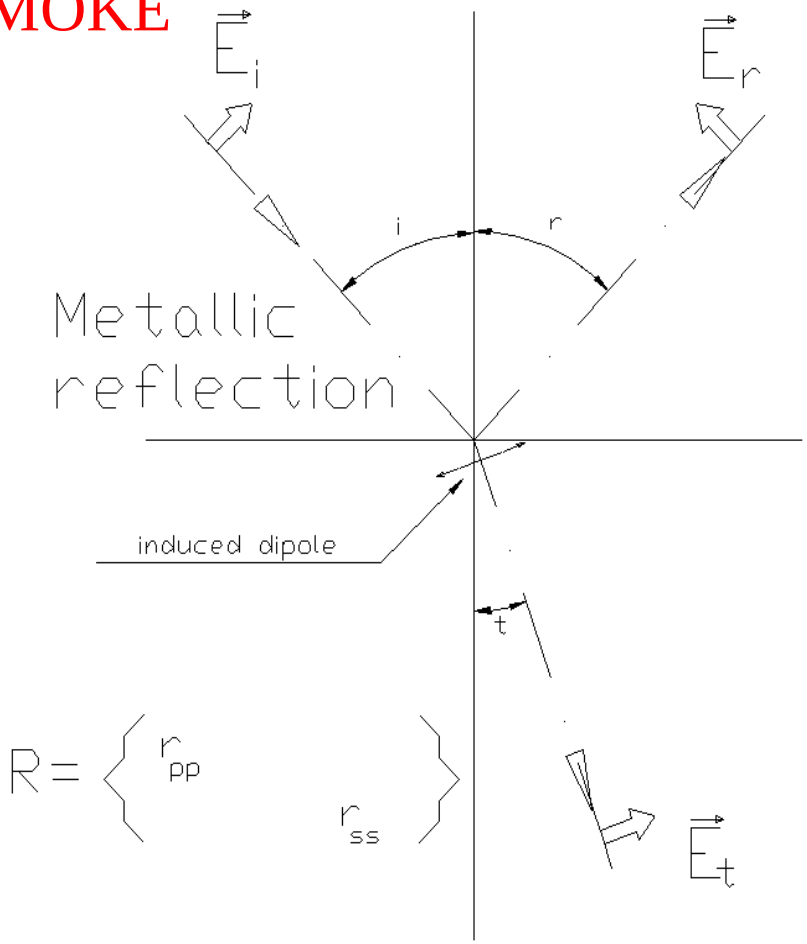

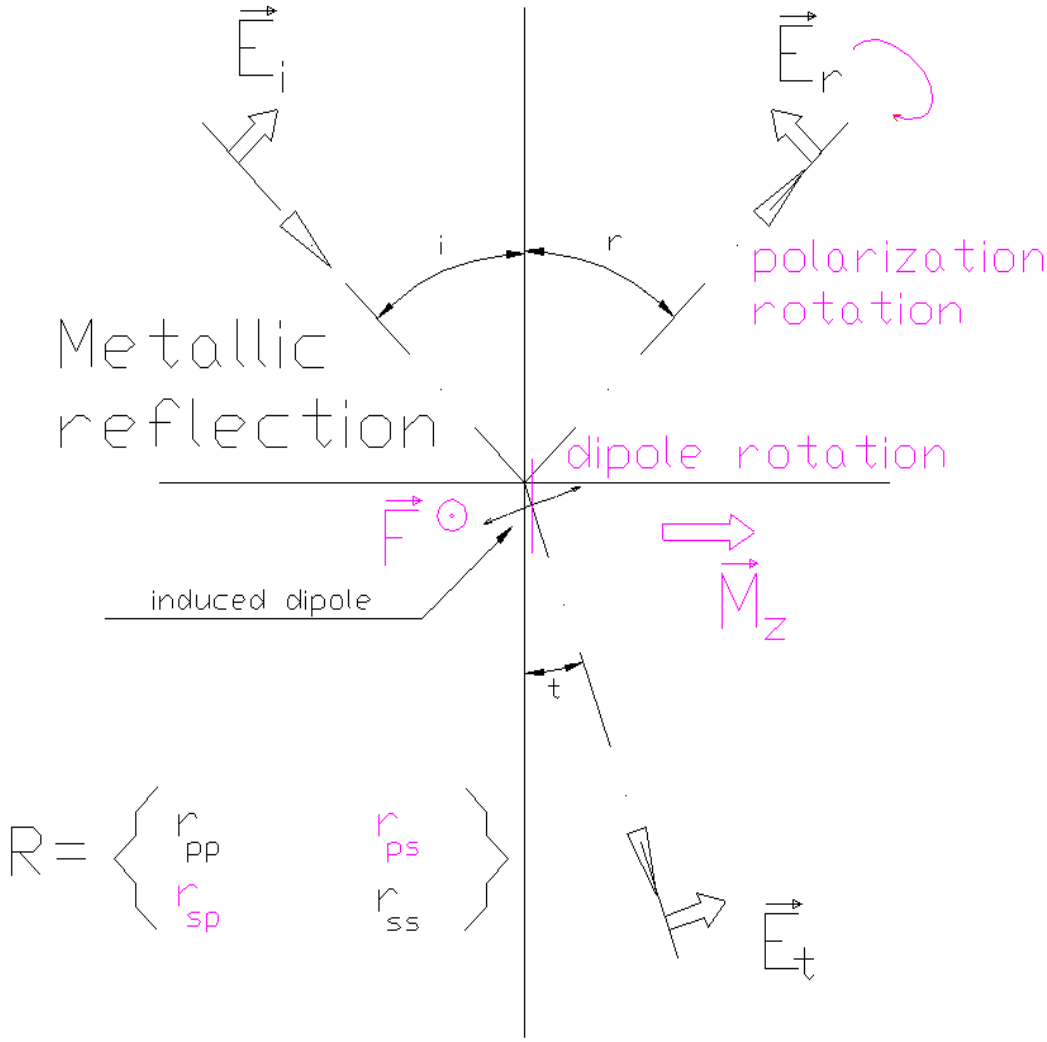

Efeitos Kerr magnetoóticos

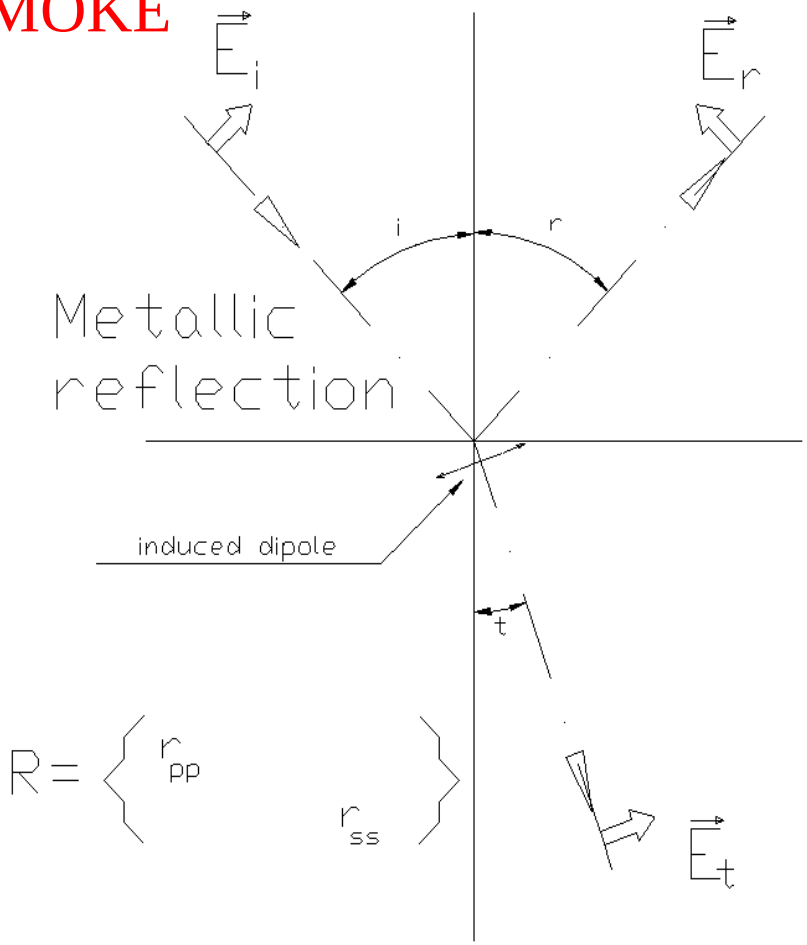

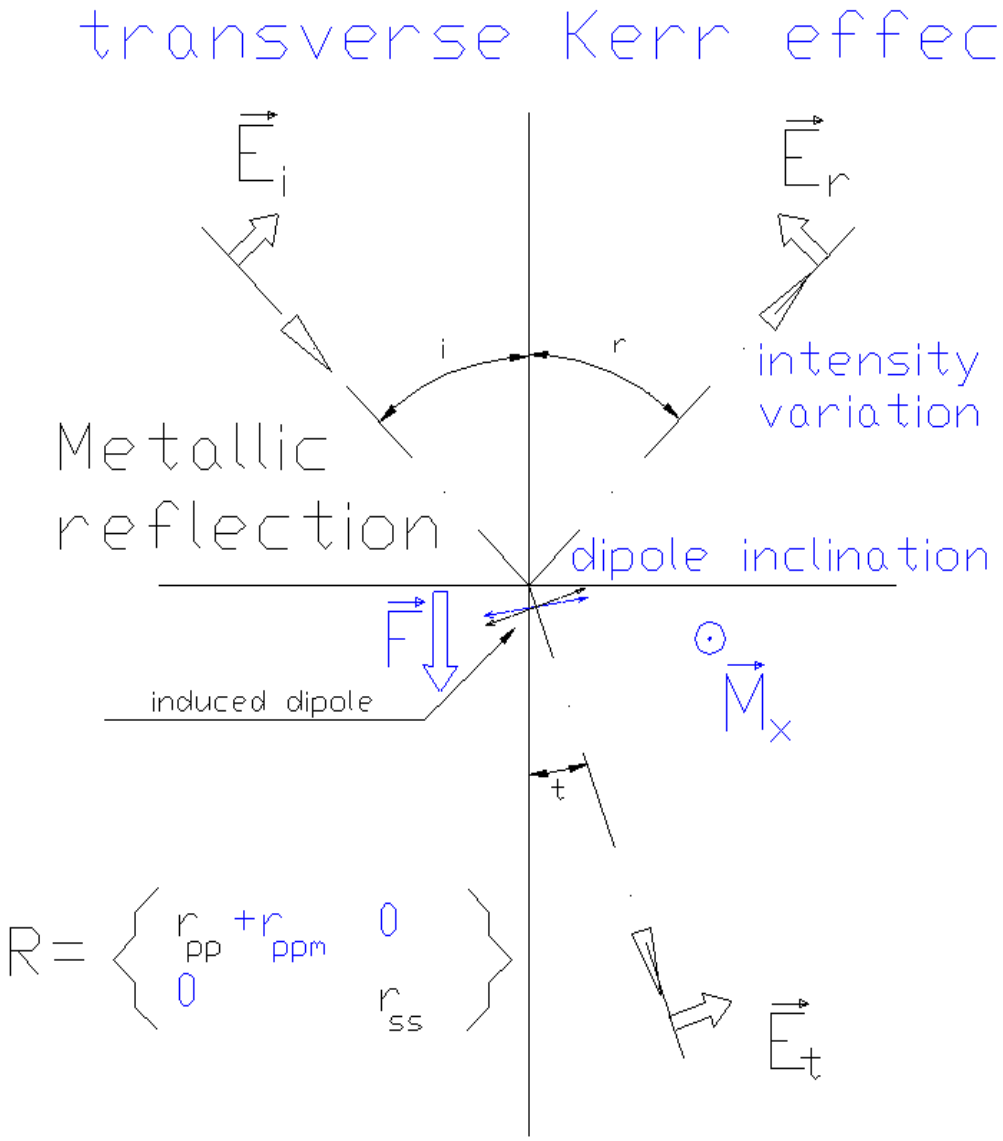

Magnetômetro TMOKE

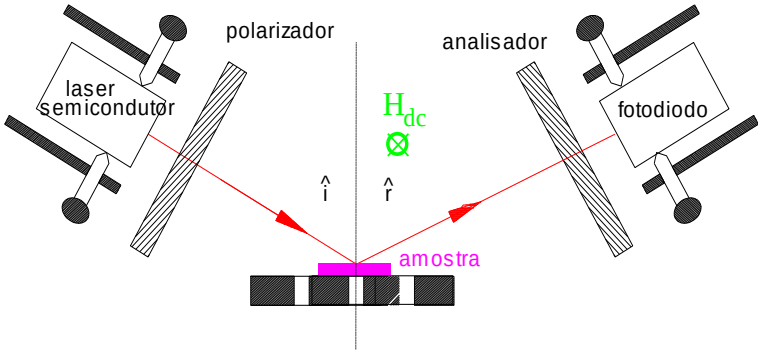

Microscópio LMOKE

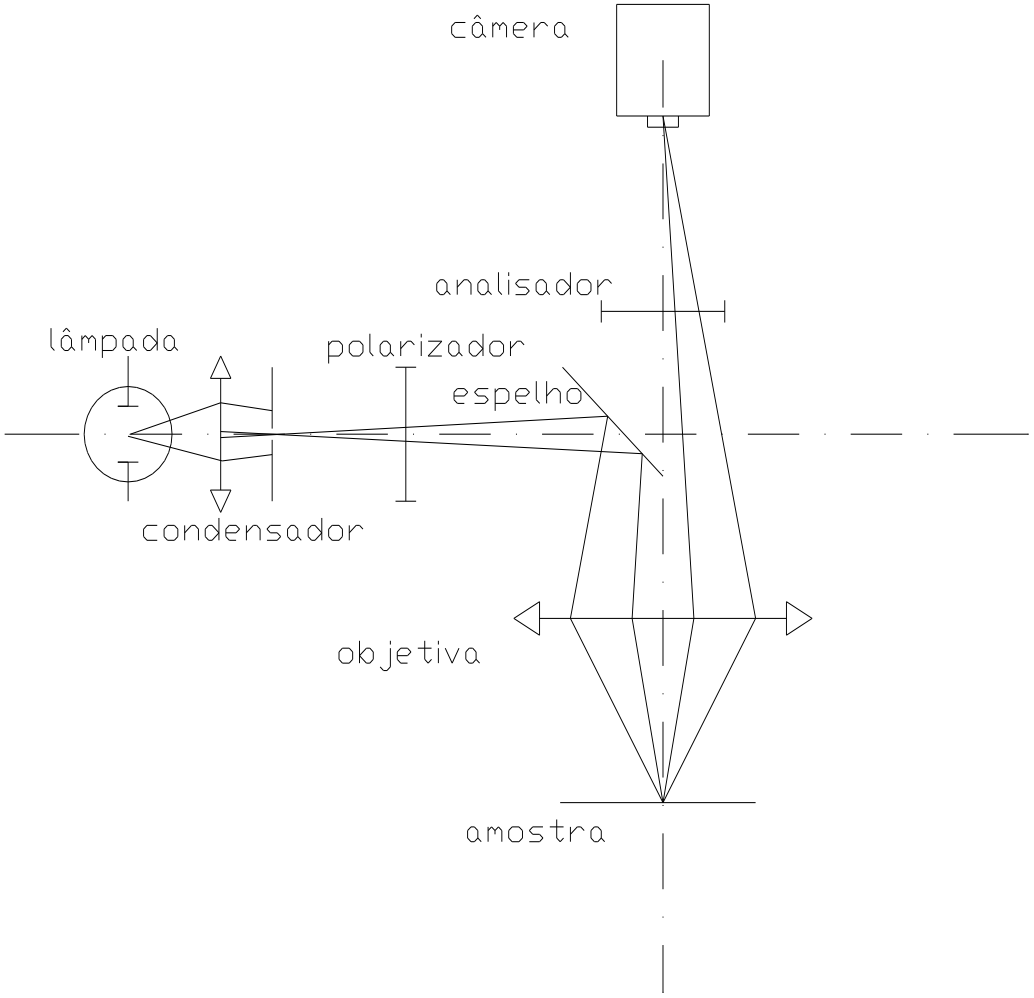

Técnicas de Polarização

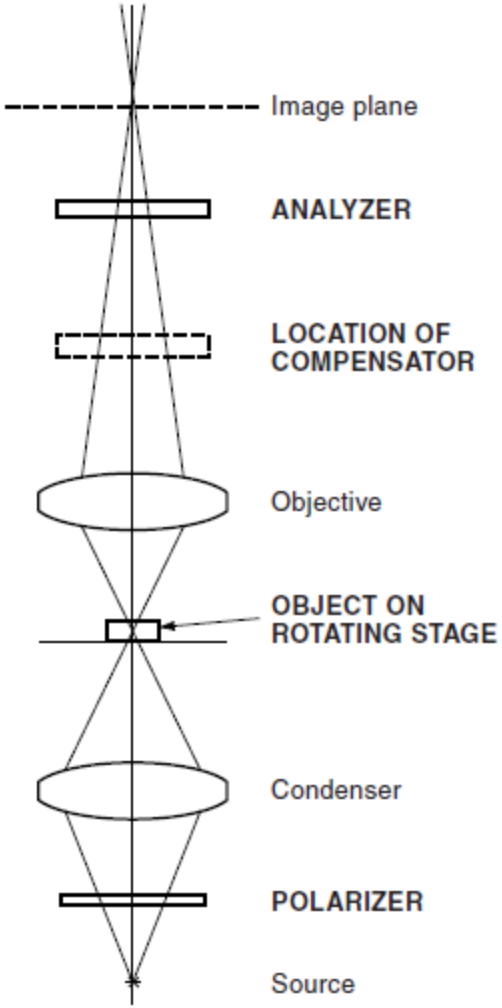

Figure 9-2

Optical components of a polarizing microscope. Notice the presence of a polarizer and analyzer, a rotatable stage, and a slot for accommodating a compensator. Polarization microscopy requires an intense light source.

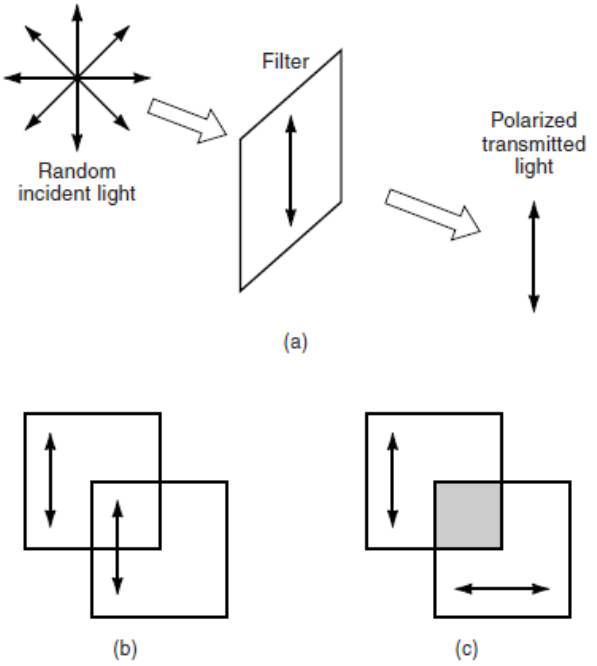

Figure 8-3

A Polaroid sheet generates linearly polarized light. (a) Only rays whose E vectors vibrate in a plane parallel with the transmission axis of the sheet are transmitted as a linearly polarized beam; other rays are partially transmitted or blocked. (b) A second overlapping polar transmits light of the first polar if its transmission axis is parallel to that of the first polar. (c) Transmission is completely blocked if the transmission axes of the two polars are crossed.

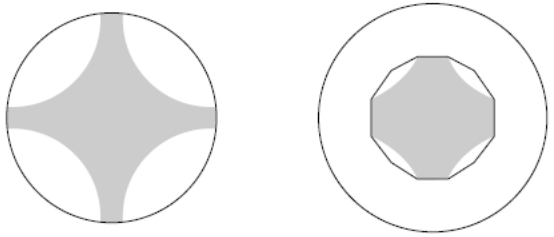

Figure 9-3

View of the polarization cross in the back aperture of the objective lens. Views before (a) and after (b) proper adjustment of the condenser aperture diaphragm.

MOKE

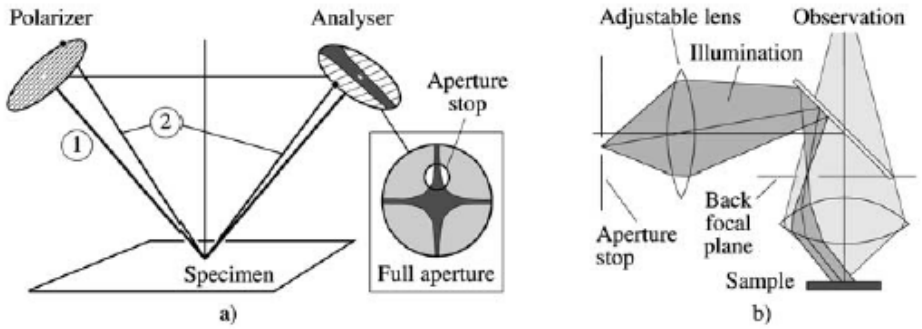

Fig. 2.15. Schematics of the illuminating aperture, polarizer and analyser (**a**). *If* the polarizer is set parallel to the central plane of incidence, the central beam (1) is reflected without a phase shift from any metallic surface. This is not true for an off-centre beam (2) with its different plane of incidence. This beam is reflected in an elliptical and rotated polarization state in general, and is thus not fully extinguished by an analyser oriented perpendicular to the central plane of incidence. The zone of extinction in the full aperture, observable in the back focal plane of a microscope (**b**), is indicated in the inset (**a**) for this case. An effective aperture stop is chosen to select an illumination with a good extinction ratio

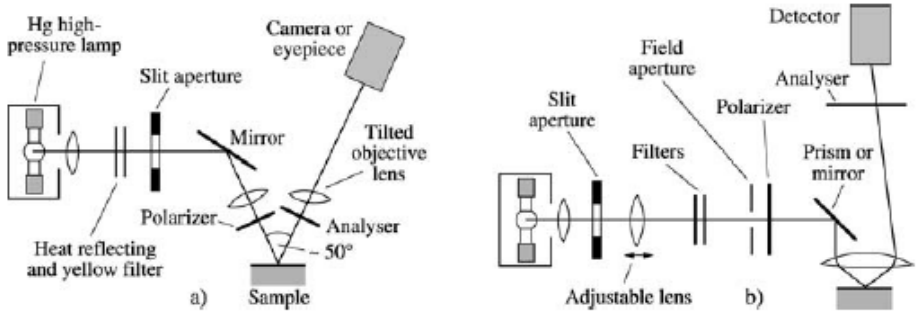

Fig. 2.14. Two Kerr microscopes. (**a**) A low resolution and high sensitivity version. In this case a wide angle objective lens, which can be tilted to reduce distortion, works best. (**b**) A high resolution, distortion-free Kerr microscope. To avoid depolarization, the objective lens and the mirror element must be strain-free

Reforço de contraste com uma camada dielétrica

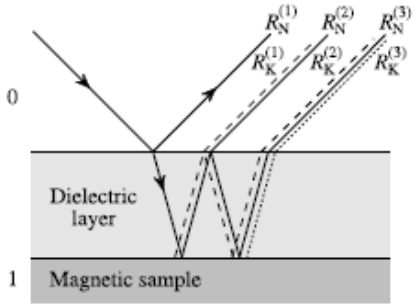

Fig. 2.13. A simple view of the enhancing effect of a dielectric layer [147]. The layer thickness is adjusted so that the normal reflectivities R_N cancel. It can be shown that in this case the Kerr amplitudes R_K (*dashed*) add up by constructive interference

- # Algumas aplicações

Fitas amorfas de $Co_{70.4}Fe_{4.6}Si_{15}B_{10}$

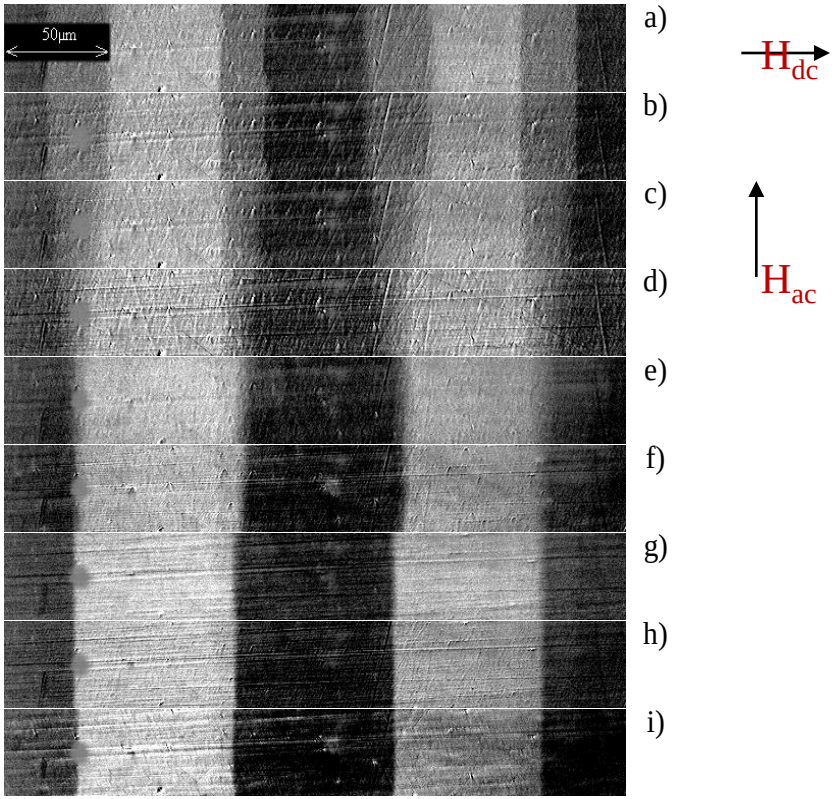

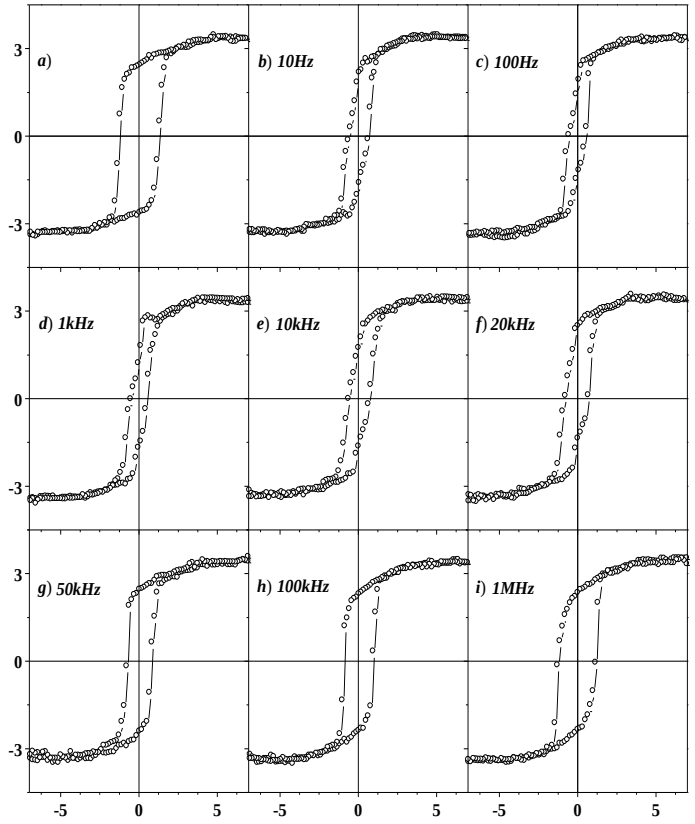

Estrutura de Domínios e Curvas de Histerese Magnetoóticas

Para uma corrente elétrica alternada de amplitude 10 mA e frequências a)10 Hz, b)1kHz, c)10 kHz, d)25 kHz, e)50 kHz, f)100 kHz, g)200 kHz, h)500 kHz and, i)1 MHz.

- Algumas aplicações

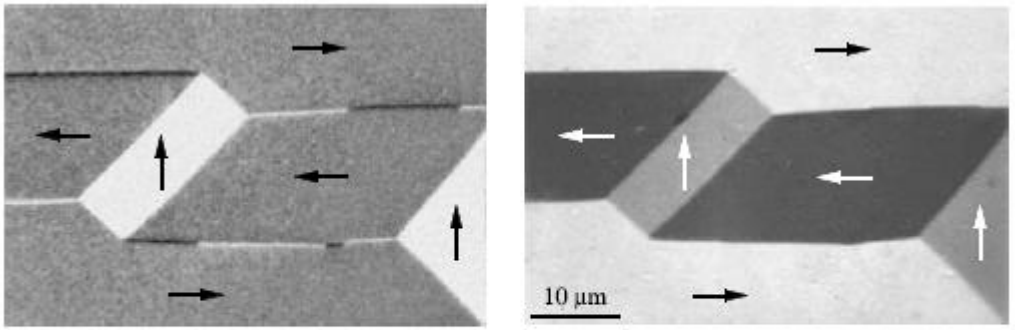

Fig. 2.18. Domain and wall images from a (100)-oriented silicon-iron crystal. With a vertical plane of incidence (**a**) the structure of the horizontal walls becomes visible. In (**b**) the sensitivity axis at oblique incidence is chosen horizontally, displaying mostly domain contrast and only indications of the wall substructure pattern

Bitter MOKE

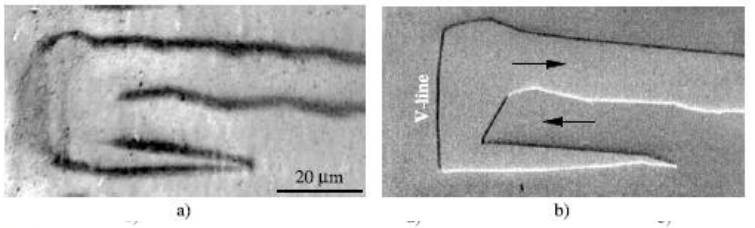

Fig. 2.6 A comparison of Bitter (a) and Kerr (b) images of similar domain patterns on a 3% Si-Fe crystal that is slightly misoriented with respect to the (110) crystal plane. The side walls of the "lancet" domains are displayed in the Bitter image, but the V-lines at the blunt ends are invisible or almost so, depending on the experimental conditions (dilution of the colloid, waiting time).

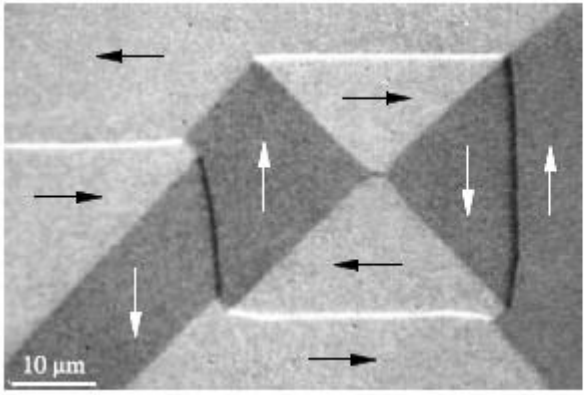

Fig. 2.23. Contrast observed at perpendicular incidence on a (100)-oriented silicon-iron crystal. The polarizer and analyser are oriented at ±45° relative to the horizontal direction, so that the Voigt effect shows up between the 90° domains, while the magneto-optic gradient-contrast becomes visible on the 180° domain boundaries

Microscopia Eletrônica de Varredura e de Transmissão

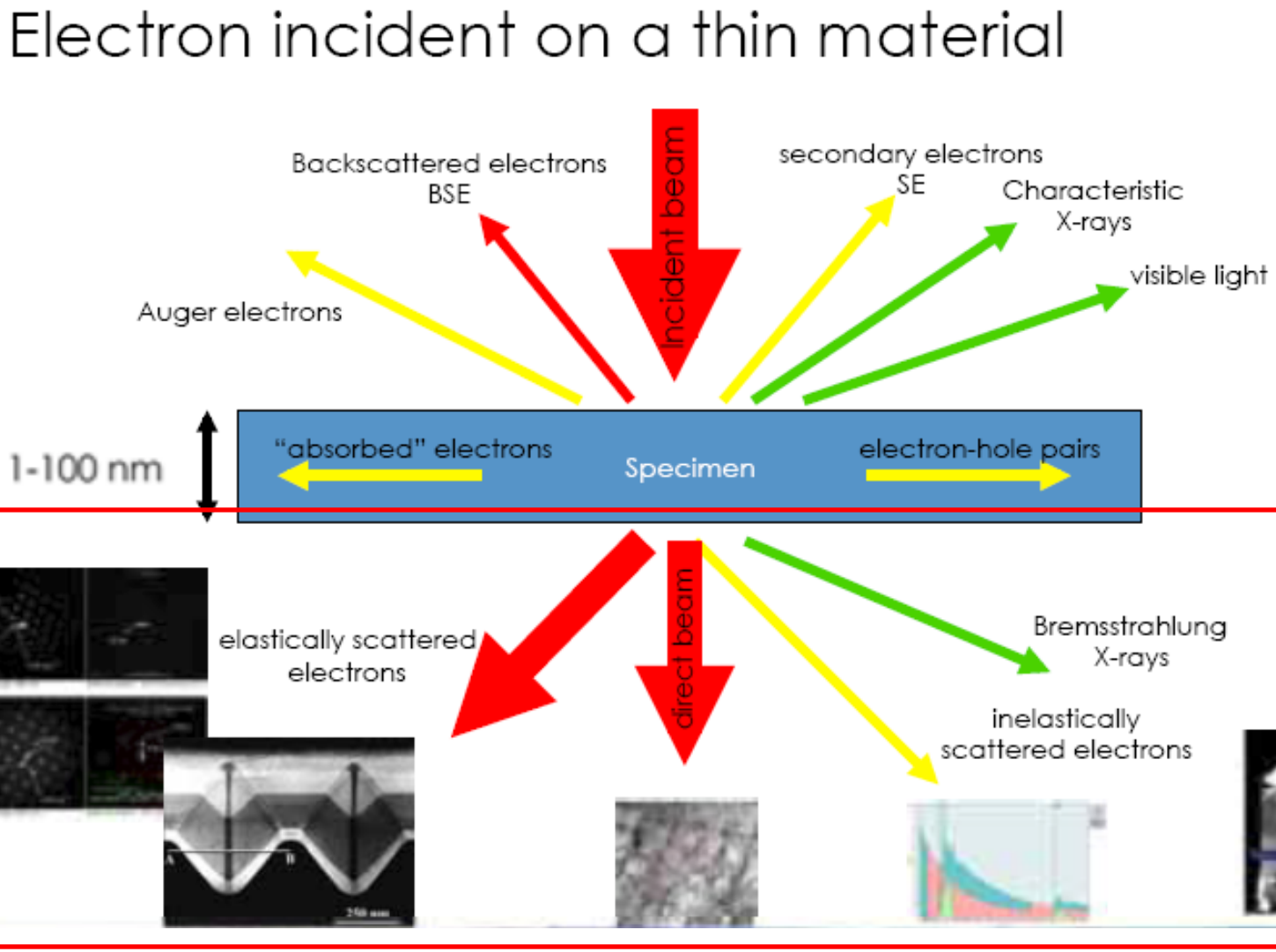

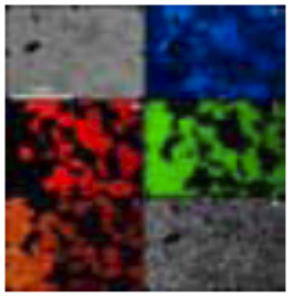

Microscopia Lorentz para observação magnética

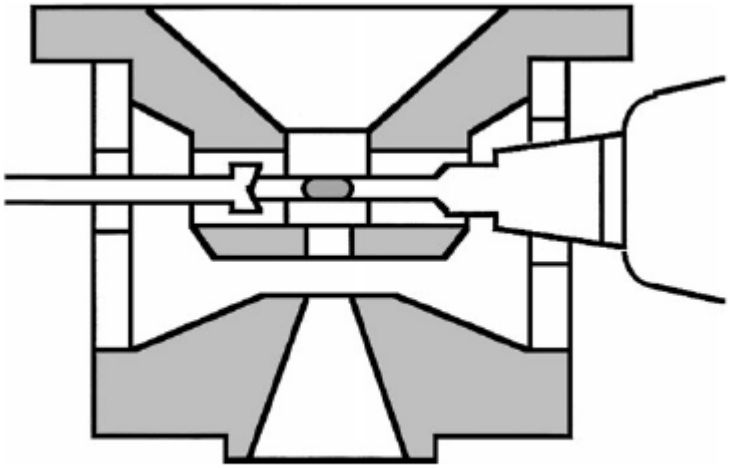

Figure 1. Cross-sectional view of the magnetic-shield lens which reduces the vertical field to 5 Oe. The specimen is set above the lens gap. The focal length is 8.6 mm [24].

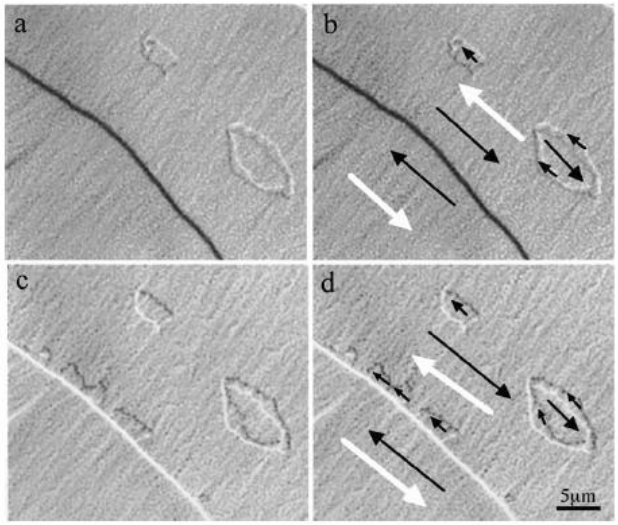

Figure 3. Lorentz microscopy of a spin valve film. Underfocused images (a, b) and overfocused images (c, d) inform the direction of induction in a thin CoFeB layer (black arrows) and that in a thick CoFeB layer which is pinned with an NiO layer (white arrows). Domain walls in the unpinned layer moved with a slight variation of the magnetic field.

desfocalizado

Modo de Fresnel

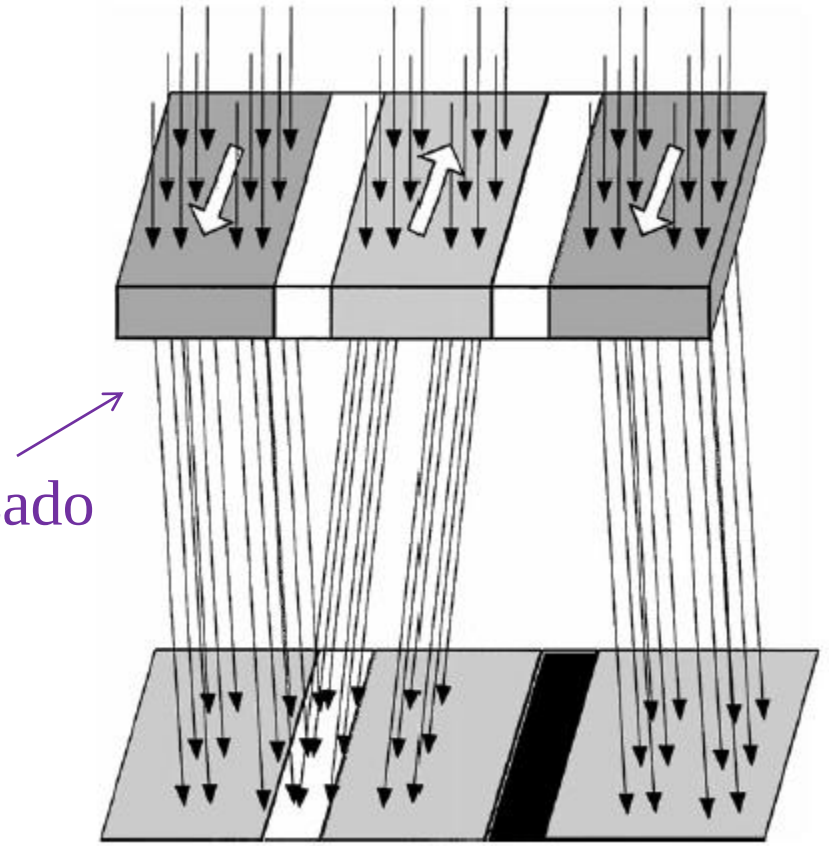

Figure 2. Fresnel mode Lorentz microscopy makes bright or dark contrast on domain walls.

Microscopia Lorentz para observação magnética

Modo de Fresnel

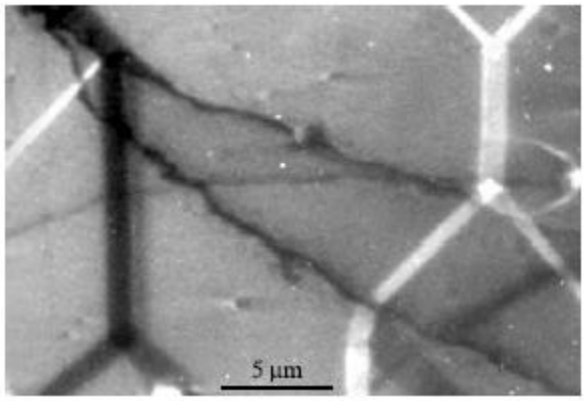

Fig. 2.27. A defocused mode Lorentz picture from a (100)-oriented single-crystal iron sample of unknown thickness. Note the asymmetric profile of the divergent (black) wall which reflects the internal structure of the asymmetric Bloch wall (Sect. 3.6.4D). The irregular lines are lattice contrasts. (Courtesy *S. Tsukahara* [261])

Modo de Foucault

focalizado

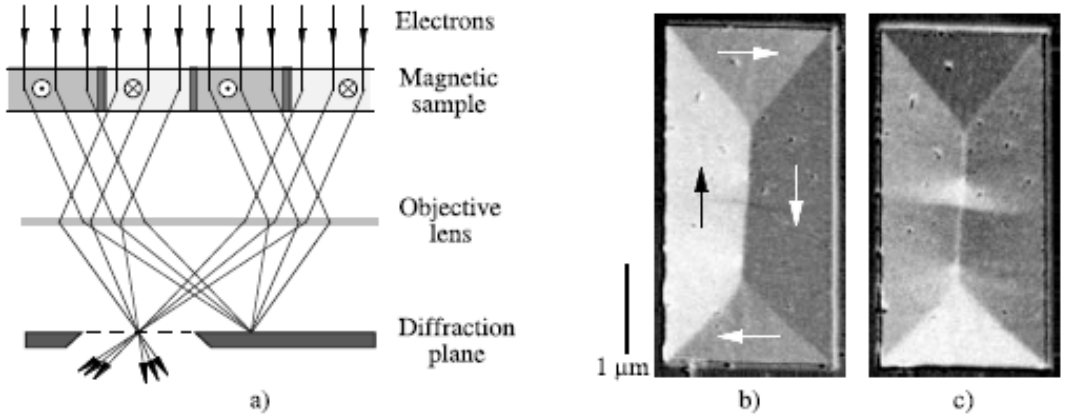

Fig. 2.28. The principle of the Foucault technique of Lorentz microscopy (**a**) and an example of two aspects of a domain pattern obtained with this technique on a thin Permalloy element of 24 nm thickness, displaying the longitudinal (**b**) and the transverse magnetization component (**c**). (Courtesy *K.J. Kirk* and *J.N. Chapman*)

Microscopia Eletrônica de Varredura

Elétrons secundários

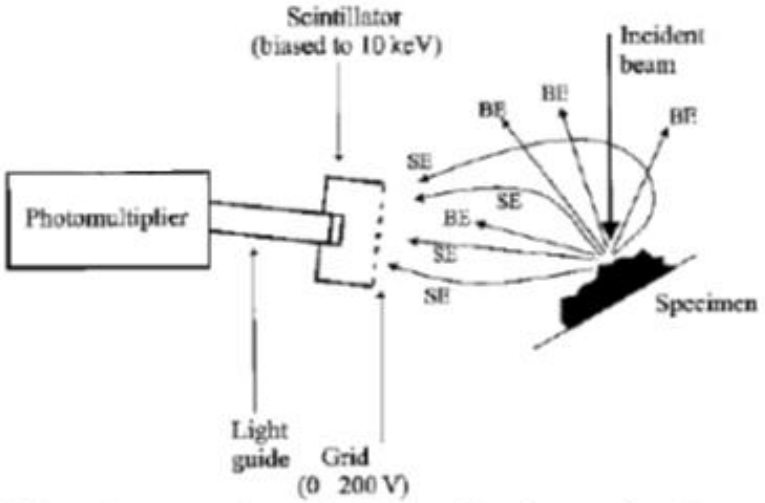

5.9 Schematic representation of the Everhart–Thornley secondary electron detector, showing the paths of secondary (SE) and backscattered (BE) electrons.

Elétrons retroespalhados

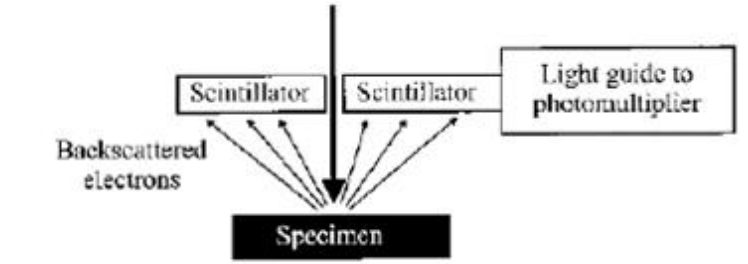

(a)

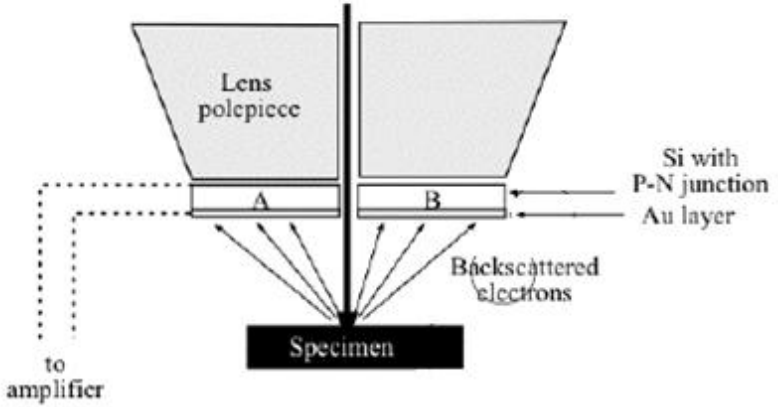

(b)

.10 (a) A large area, Robinson type scintillator detector. (b) A solid state silicon detector with two elements A and B.

- Algumas aplicações

Elétrons secundários

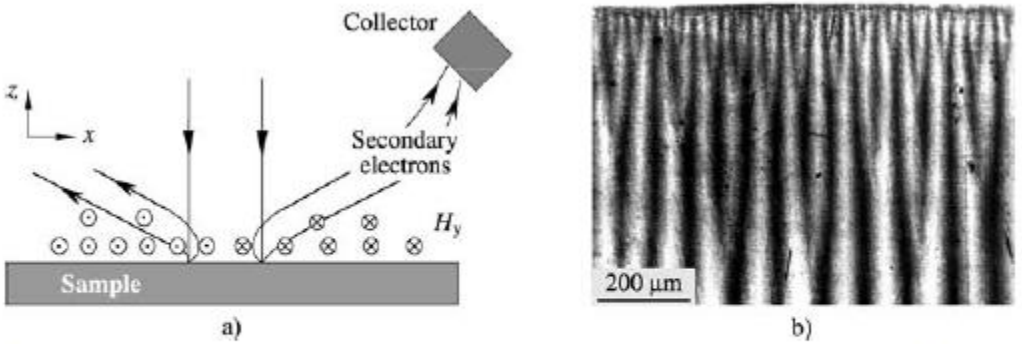

Fig. 2.33. Schematic of Type I contrast (**a**). The secondary electrons of the two beams see different fields and are deflected into different directions. (**b**) Domains on a cobalt crystal (edge view) as a typical example for this technique. (Courtesy *J. Jakubovics* [312])

Elétrons retroespalhados

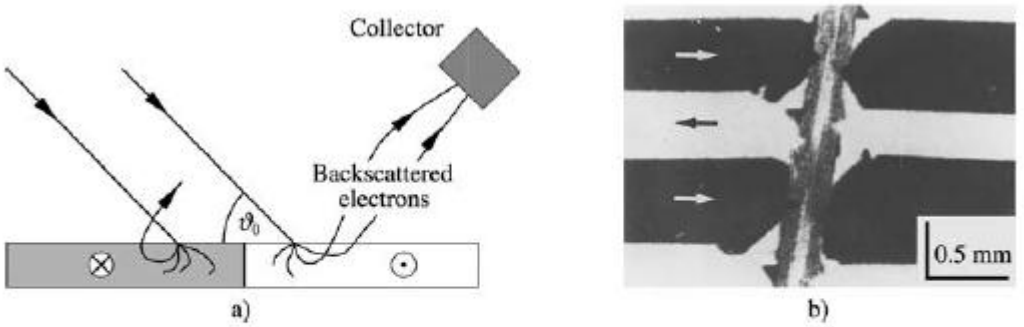

Fig. 2.34. Backscattering contrast in the SEM (**a**) with some typical electron paths inside the sample, and an image of a silicon-iron transformer steel sample (**b**) showing domains near a scratch introduced for the purpose of domain refinement. (Courtesy *T. Nozawa* [332])

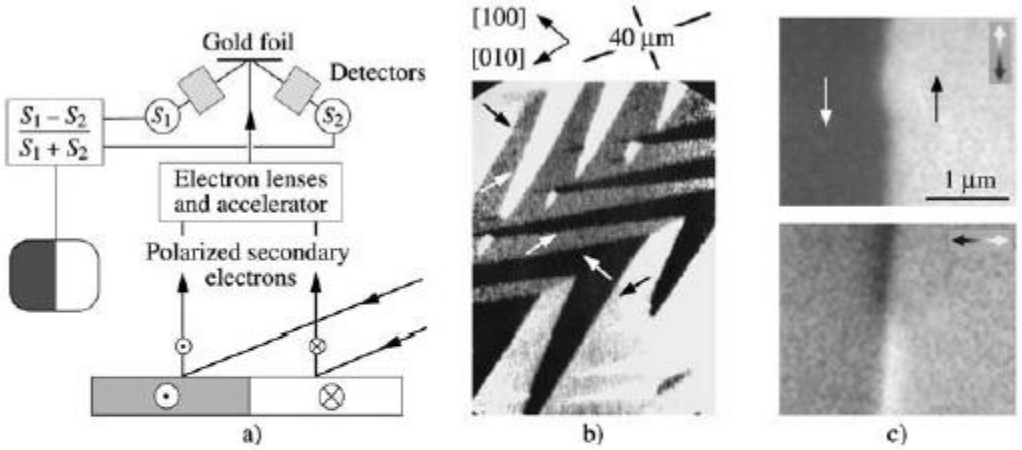

Fig. 2.38. (**a**) Detecting polarized electron contrast in an ultra high vacuum SEM. The magnetic information is extracted by a signal processing unit connected to a polarization detector. (**b**) Domains on a (100) SiFe crystal. (Courtesy *K. Koike*.) (**c**) High-resolution picture of the transition in the surface structure of a domain wall in an iron whisker, shown with two different sensitivity directions. (Courtesy *J. Unguris* and *R. Celotta*)

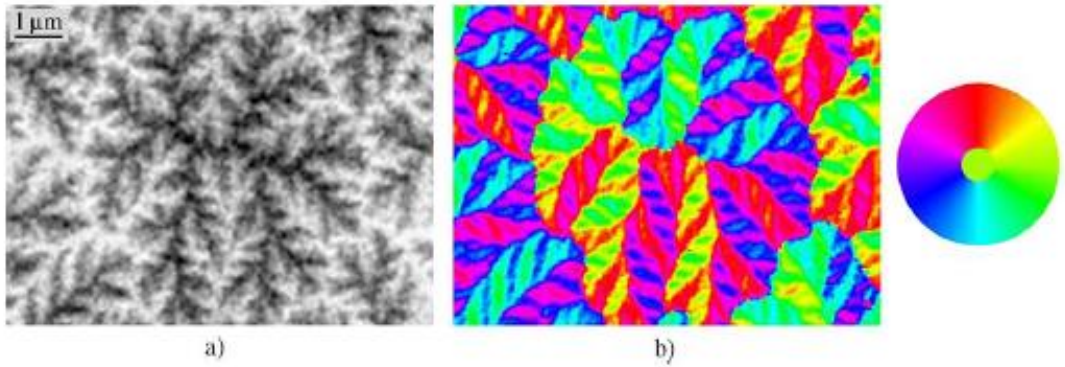

Fig. 2.39. Polar (**a**) and in-plane (**b**) magnetization components of a cobalt crystal cut parallel to the basal plane, made visibly with electron polarization techniques. A colour code is used in the representation of the in-plane components (Courtesy *J. Unguris NIST*)

Scanning electron microscopy with polarization analysis (SEMPA)

M. R. Scheinfein, J. Unguris, M. H. Kelley, D. T. Pierce, and R. J. Celotta
National Institute of Standards and Technology, Gaithersburg, Maryland 20899

2501 Rev. Sci. Instrum. 61 (10), October 1990

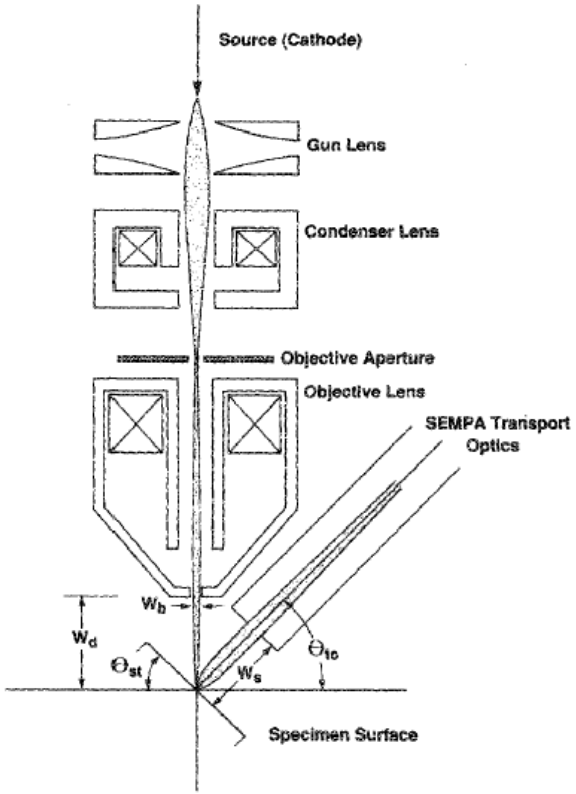

FIG. 3. A cross section of a generic electron optical column illustrating some key design parameters such as the working distance W_d, the exit lens bore W_b, distance of approach of SEMPA extraction optics W_s, stage tilt angle Θ_{st}, and SEMPA transport optics angle Θ_{to}.

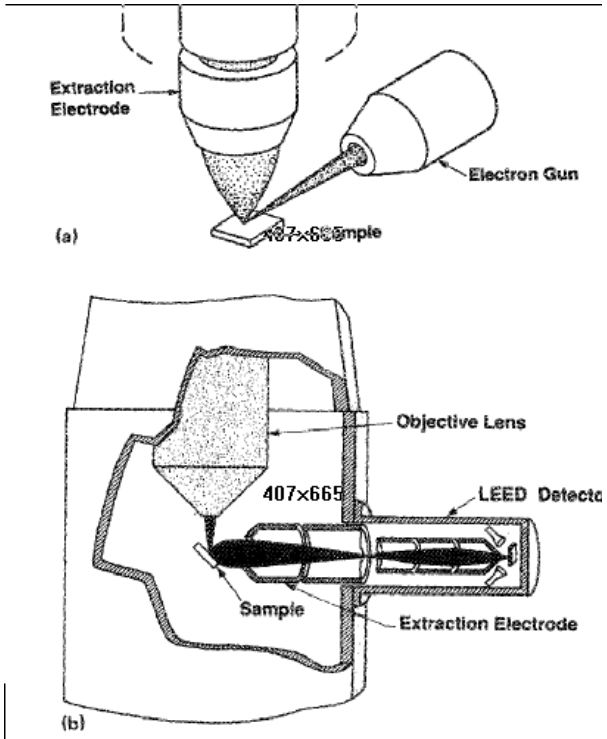

FIG. 9. (a) SEMPA system developed by Koike and co-workers (Ref. 13) (b) SEMPA system developed by Kirschner and Oepen (Ref. 14).

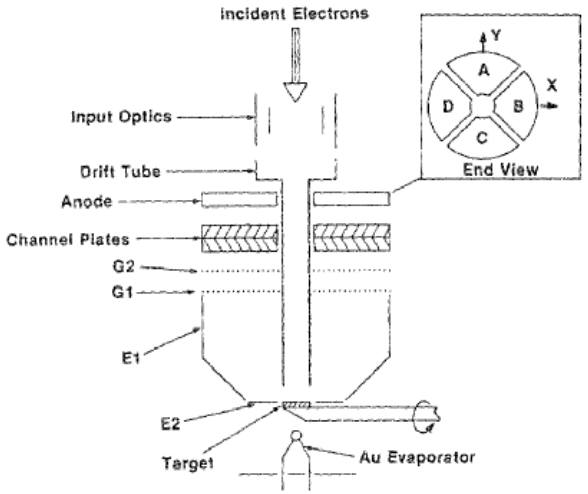

FIG. 4. A cross section of the LEDS detector. The divided anode assembly is shown in the inset as viewed from the Au target.

Scanning electron microscopy with polarization analysis (SEMPA)

M. R. Scheinfein, J. Unguris, M. H. Kelley, D. T. Pierce, and R. J. Celotta
National Institute of Standards and Technology, Gaithersburg, Maryland 20899

2501 Rev. Sci. Instrum. 61 (10), October 1990

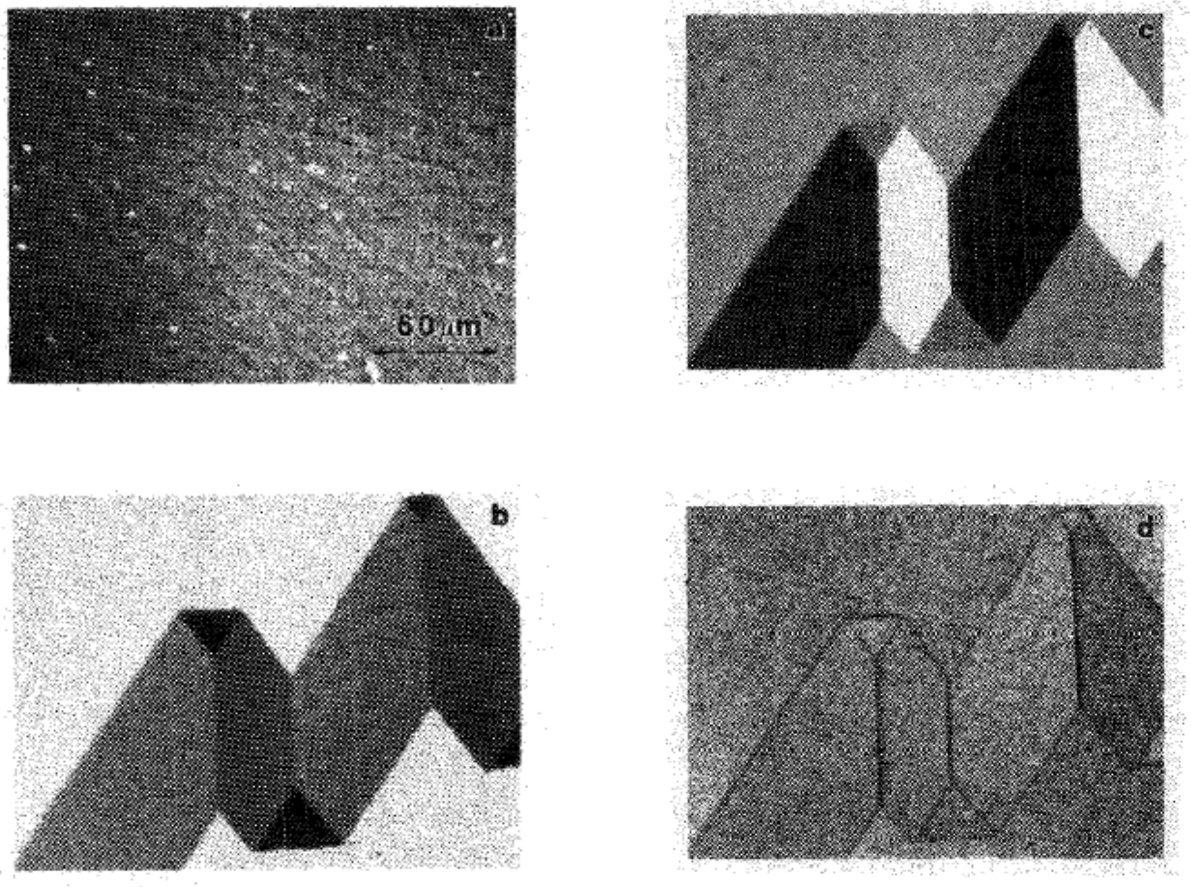

FIG. 10. Images of FeSi (100) surface. Images are 253 μm across. (a) Secondary electron intensity image, (b) M_x, (c) M_y, and (d) $|M|$ images.

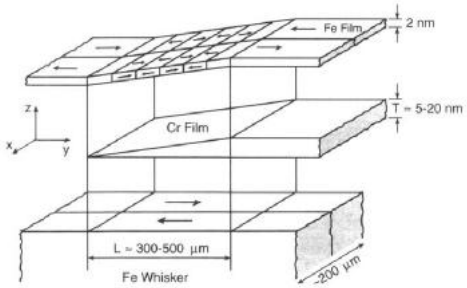

FIG. 1. A schematic exploded view of the Fe/Cr/Fe(100) sample structure showing the Fe(100) single-crystal whisker substrate, the Cr wedge, and the Fe overlayer. The arrows show the magnetization direction in each domain. The z scale is expanded approximately 5000 times.

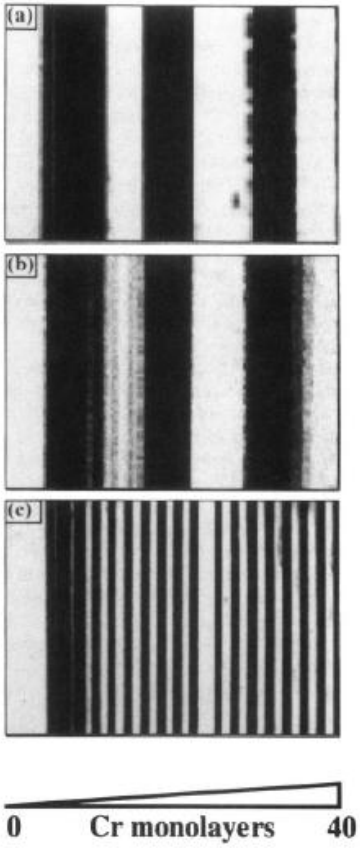

FIG. 2. SEMPA magnetization images of the Fe overlayer coupled through Cr spacer layers grown at Fe substrate temperatures of (a) 30, (b) 200, and (c) 350 °C, respectively. The Cr spacer layer increases in thickness from 0 to 40 monolayers, as indicated, from the left to the right of the images. The magnetization of the Fe overlayer is parallel (ferromagnetically coupled) to the substrate in the white regions, and antiparallel (antiferromagnetically coupled) in the black regions.

PHYSICAL REVIEW B VOLUME 49, NUMBER 20

Influence of Cr growth on exchange coupling in Fe/Cr/Fe(100)

D. T. Pierce, Joseph A. Stroscio, J. Unguris, and R. J. Celotta

Surface Review and Letters, Vol. 5, No. 6 (1998) 1213–1219

SPIN-POLARIZED LOW ENERGY ELECTRON MICROSCOPY

TH. DUDEN and E. BAUER
Department of Physics and Astronomy, Arizona State University,

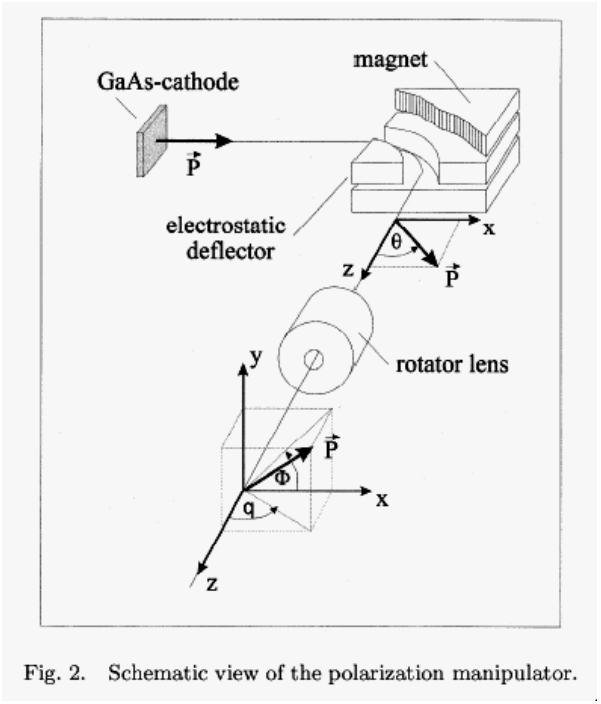

Fig. 2. Schematic view of the polarization manipulator.

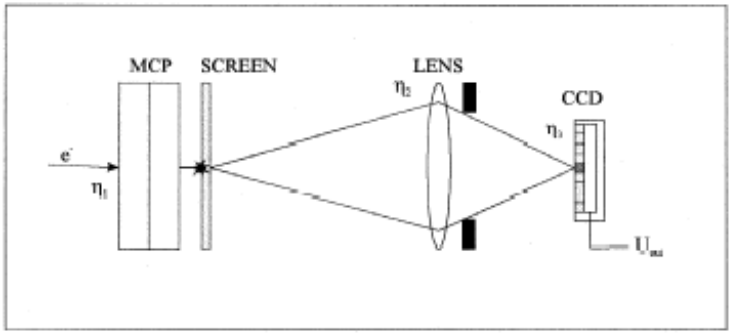

Fig. 3. Simplified schematic of the detection system.

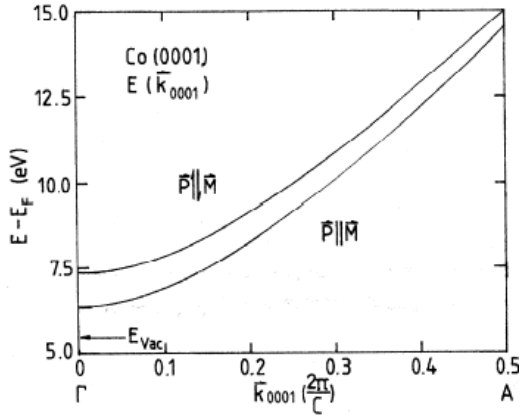

Fig. 1. Band structure of Co above the vacuum level

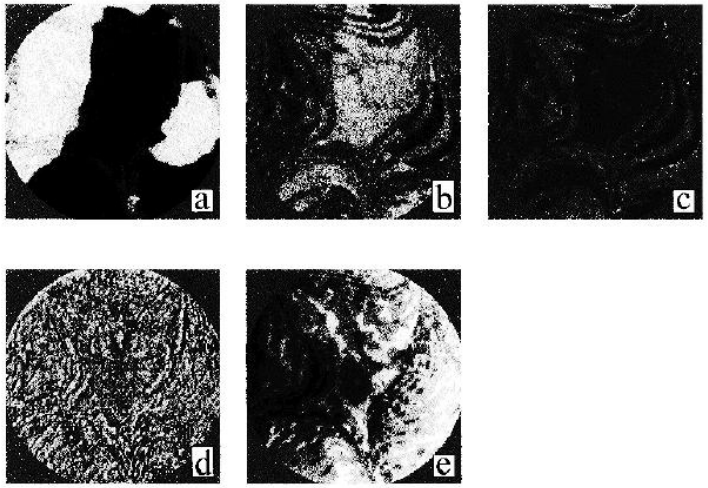

Fig. 5. 5 ML Co/W(110), field of view approximately 6 μm, energy for (a)–(d) 1.2 eV, for (e) 3 eV. (a), (b) Magnetic in-plane and out-of-plane images. (c) Angular distribution. (d), (e) Topography.

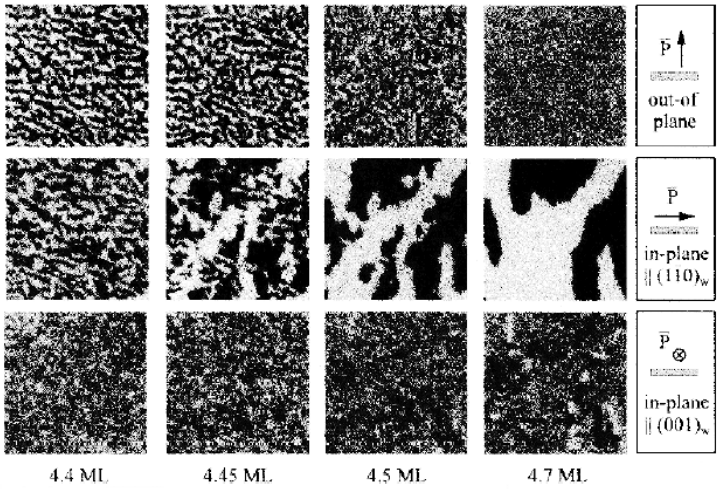

Fig. 6. The evolution of the magnetic domain structure of a Co film deposited on top of 10 Au(111)/W(110). The Co film thickness is given below the image columns. Field of view 7×7 μm, energy 1.2 eV.

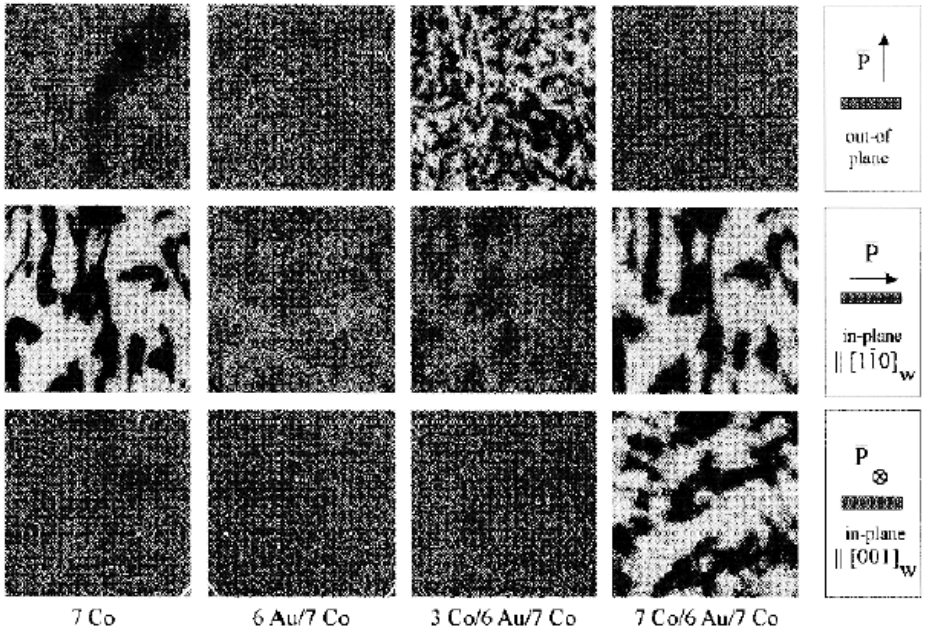

Evolution of the magnetic domain structure of a sandwich layer during top layer growth. (For

Caracterização dos Materiais

Energia / Momento Matéria → Interação matéria-matéria, (ou radiação-matéria) → Propriedade a ser caracterizada → Detectam-se forças ou corrente elétrica (ou intensidade luminosa) → Energia / Momento Matéria

+

•Microscopias de Sonda Local (SPM)

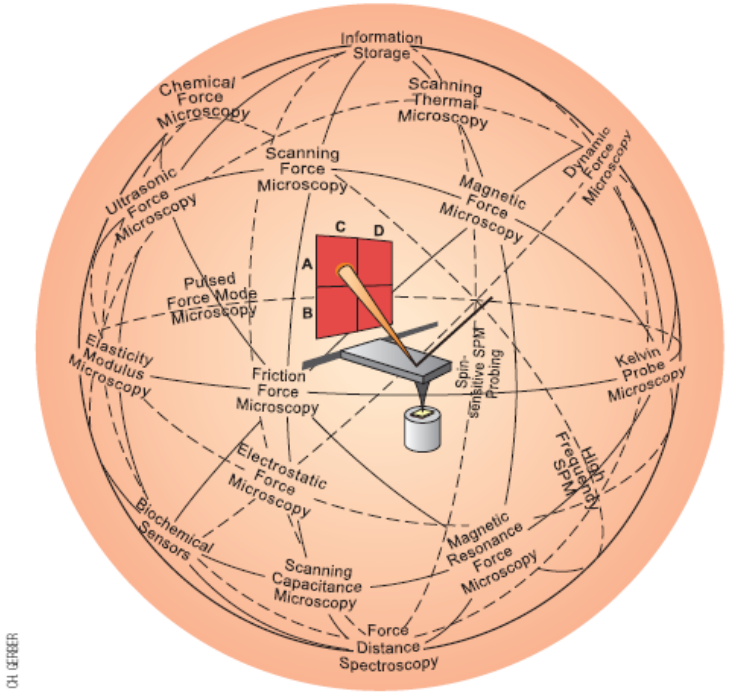

Figure 2 World of possibility. The AFM (centre) has inspired a variety of other scanning probe techniques. Originally the AFM was used to image the topography of surfaces, but by modifying the tip it is possible to measure other quantities (for example, electric and magnetic properties, chemical potentials, friction and so on), and also to perform various types of spectroscopy and analysis.

Nature Nanotechnology, 1 (2006) 3

Interação Ponta-Amostra

Microscópio de tunelamento eletrônico (STM)

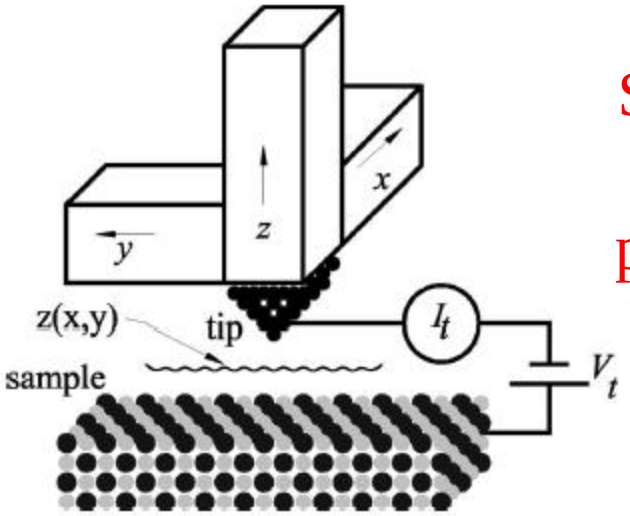

FIG. 2. A scanning tunneling microscope (schematic).

Se a ponta for magnética (Gd) os elétrons serão parcialmente polarizados

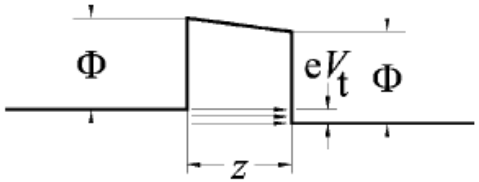

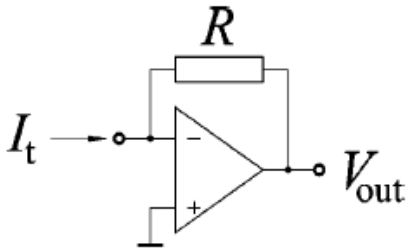

FIG. 4. A simple current-to-voltage converter for an ST for the qPlus sensor shown in Fig. 11. It consists of an tional amplifier with high speed, low noise, and low inp current, as well as a feedback resistor (typical imped $\approx 10^8\ \Omega$) that has low parasitic capacitance. The outpu age is given by $V_{out} = -R \times I_t$.

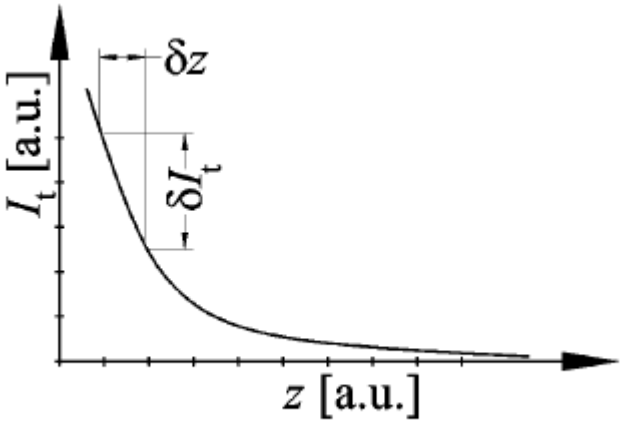

FIG. 5. Tunneling current as a function of distance and

Microscópio de força atômica (AFM)

- **Modo de contato**
- **Modo "tapping" (intermitente)**

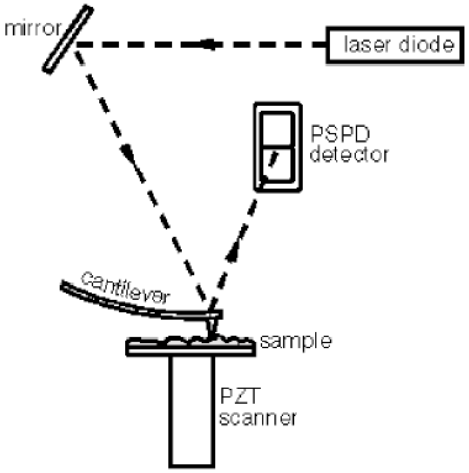

Figure 1-5. The beam-bounce detection scheme.

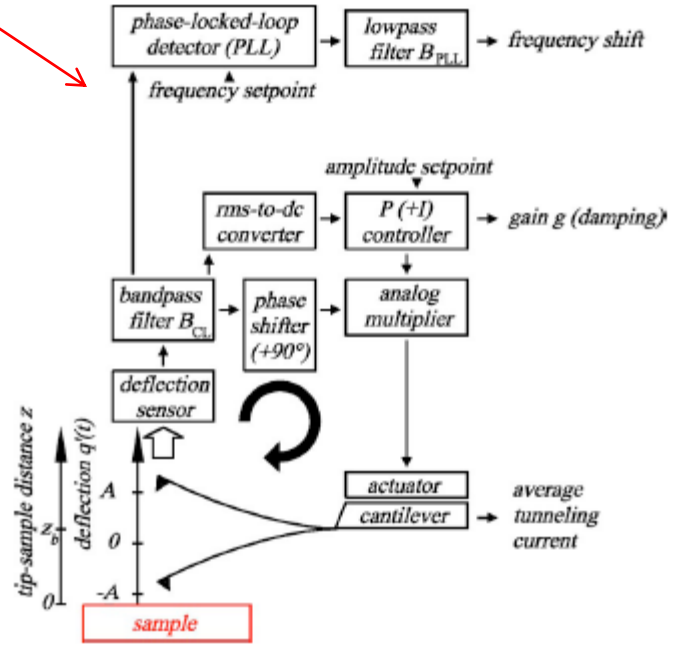

FIG. 25. (Color in online edition) Block diagram of the frequency-modulation AFM feedback loop for constant amplitude control and frequency-shift measurement. Three physical observables are available: frequency shift, damping signal, and (average) tunneling current.

Microscópio de força atômica (AFM)

- Força normal
- Força lateral

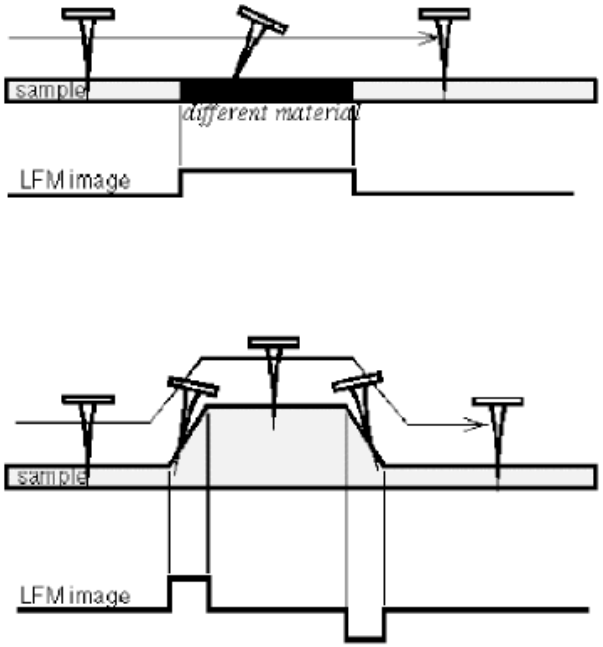

Figure 1-9. Lateral deflection of the cantilever
from changes in surface friction (top) and from changes in slope (bottom)

Microscópio de força magnética (MFM)

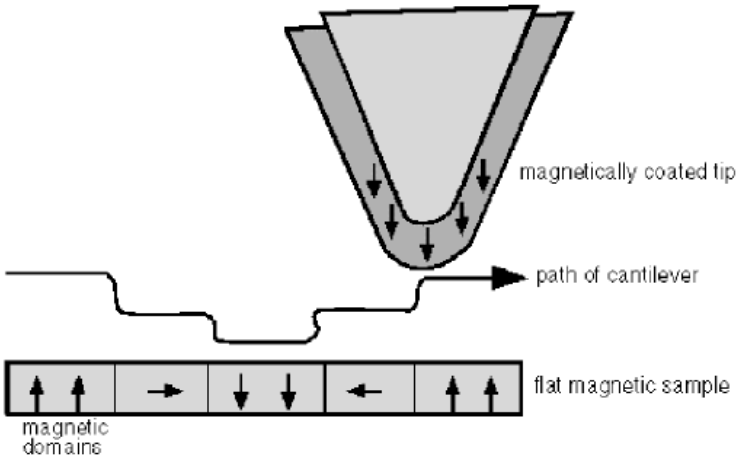

Figure 1-7. MFM maps the magnetic domains of the sample surface.

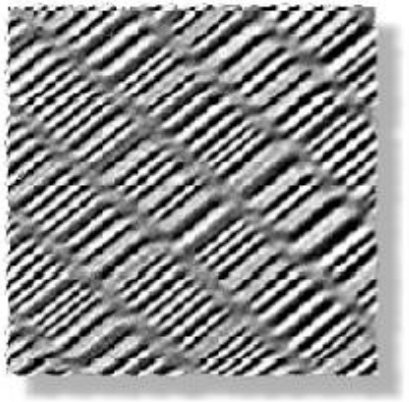

MFM image showing the bits of a hard disk.
Field of view 30μm.

MFM

Técnicas

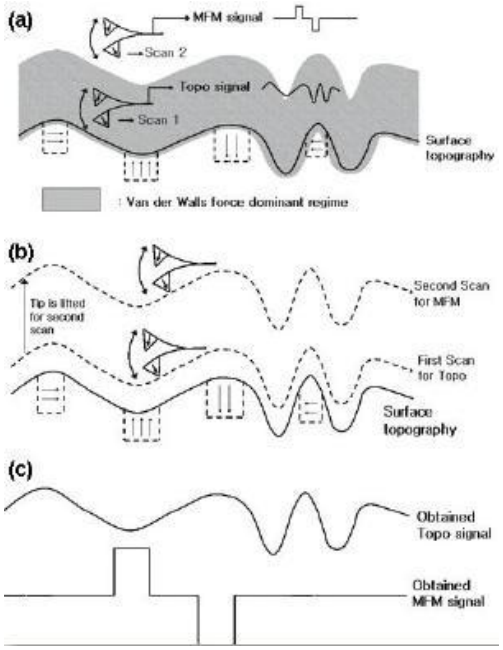

Fig. 2.40. Written longitudinal recording track pattern observed in a magnetic force microscope, displaying the magnetic charges at the transitions. (Courtesy *D. Rugar*, IBM Research)

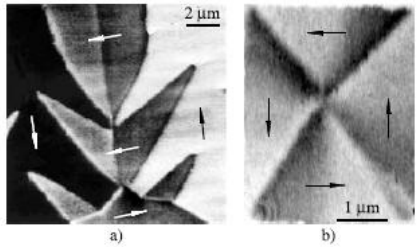

Fig. 2.41. MFM images of domains on soft magnetic materials: (**a**) bulk silicon-iron and (**b**) FeTaN thin film element of 30 nm thickness. (Courtesy *L. Belliard* and *J. Miltat* [393, 394])

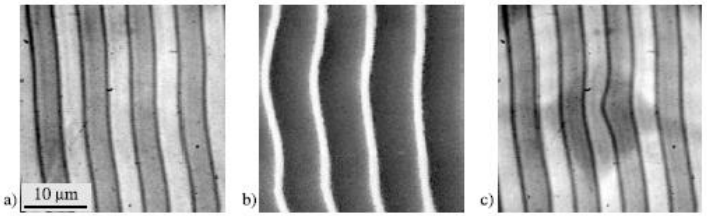

Fig. 2.44. Combined magnetic force and Faraday effect observations on a transparent magnetic garnet film with perpendicular anisotropy. (**a**) Undisturbed band domain pattern as seen by the Faraday effect. (**b**) The same pattern as observed in MFM contrast. The discrepancy between (**a**) and (**b**) is explained in (**c**), where the local distortion of the domain wall caused by the MFM tip is observed simultaneously in the Faraday effect image through the transparent substrate [the pyramidal shape of the probe can be seen as a shadow in (**c**)]. (Courtesy *J. Miltat* and *L. Belliard*, Orsay)

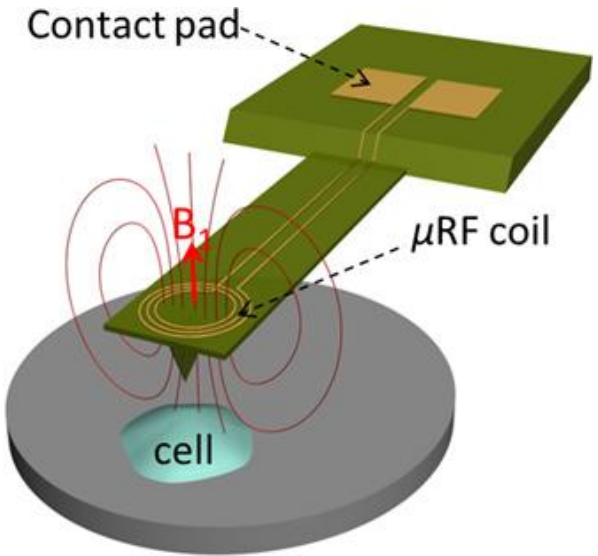

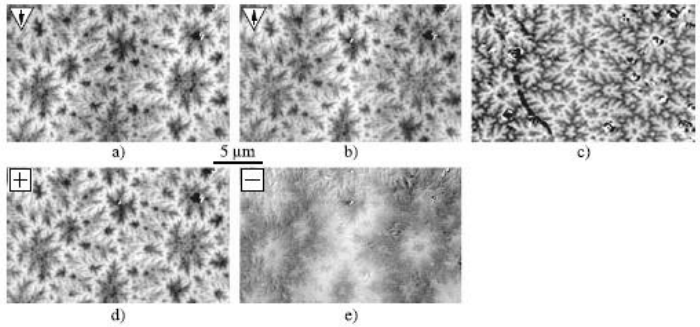

Fig. 2.43. Comparing magnetic force images for opposite tip polarities (**a**, **b**) of the branched domain pattern on the basal plane of a cobalt crystal with a Kerr image of the same pattern (**c**). The MFM images display a better resolution than the optical image, but are not identical because of the superposition of two contrast mechanisms, that of charge and of susceptibility imaging, which can be separated in digitally generated sum and difference images (**d**, **e**) as explained in the text (together with *W. Rave* and *E. Zueco*, Dresden [390]).

PEEM

Técnicas

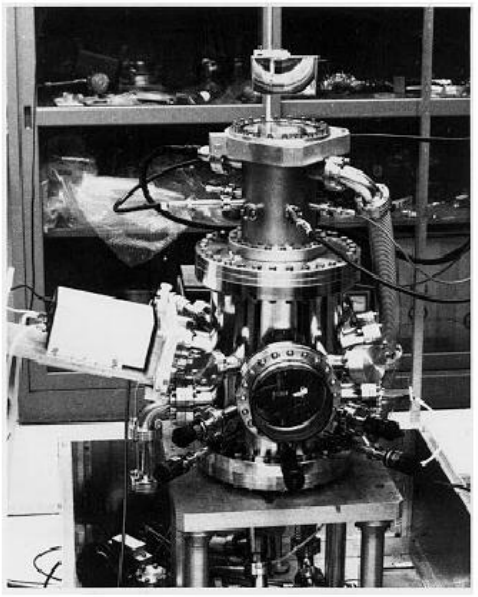

Fig. 1. The photoelectron microscope built at Bowling Green. Electrostatic electron optics are mounted vertically on top of an ultrahigh vacuum chamber. An ultraviolet Hg lamp is mounted on the left.

Surface Review and Letters, Vol. 5, No. 6 (1998) 1269–1274

IMAGING OF MAGNETIC DATA BITS AND FERROMAGNETIC DOMAINS WITH PHOTOELECTRON EMISSION MICROSCOPY

M. MUNDSCHAU and J. ROMANOWICZ
J. Y. WANG, D. L. SUN and H. C. CHEN

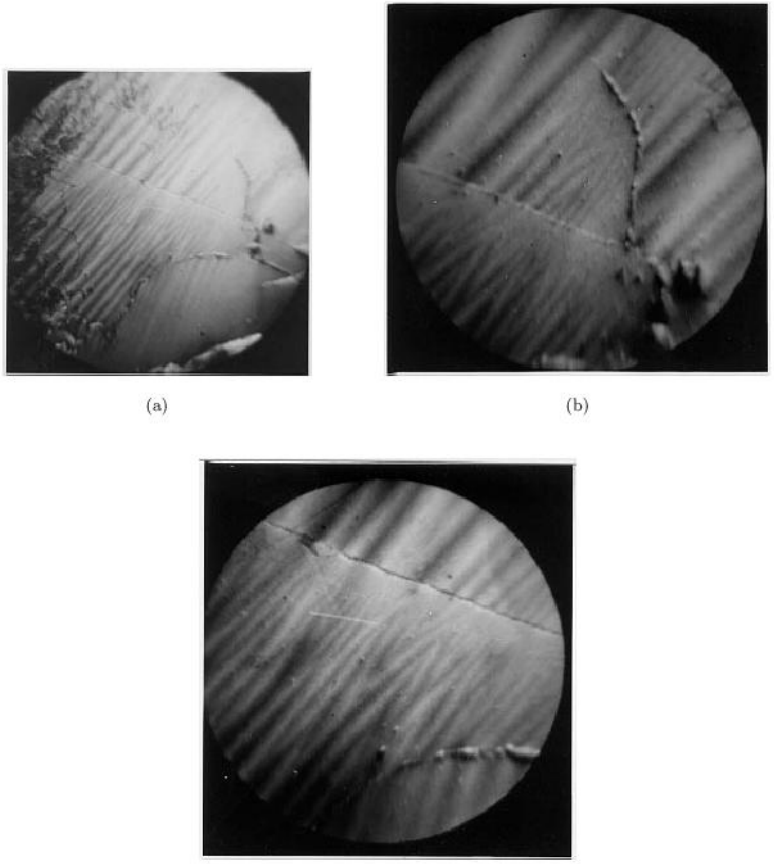

Fig. 3. Photoelectron images of ferromagnetic domains near grain boundaries and defects of a sample of neodymium–iron–boron. (a) Diameter 500 microns; (b), (c) areas in (a) further magnified. Both diameters are 200 microns. Reversal domains at grain boundaries are similar to those seen in other ferromagnetic materials, such as cobalt and Fe-4% Si alloys.

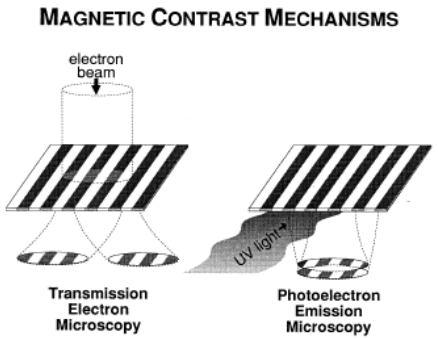

Fig. 4. Schematic showing the origin of magnetic contrast in (a) a transmission electron microscope in which magnetic forces within the bulk of the sample split the transmitted beam into two and (b) the photoelectron emission microscope in which magnetic fields outside the sample deflect electrons. The areas of the edges yielding magnetic contrast contrast are greatly exaggerated.

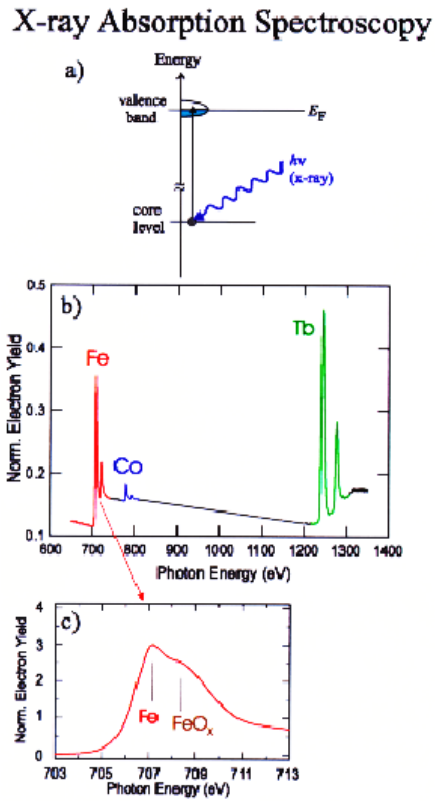

Fig. 2. (a) Principles of X-ray absorption spectroscopy, using a one-electron model for the case of L edge absorption in a d band transition metal.[14] In the X-ray absorption process an electron is excited from the core shell to empty valence states. This results in pronounced resonances at the absorption thresholds, as illustrated in (b) for the $2p_{3/2} \rightarrow 3d$ (L_3 edge) and $2p_{1/2} \rightarrow 3d$ (L_2 edge) excitations in Fe and Co and the $3d_{5/2} \rightarrow 4f$ (M_5 edge) and $3d_{3/2} \rightarrow 4f$ (M_4 edge) excitations in Tb. Here the X-ray absorption spectrum for a $Tb_{24.5}Fe_{70.5}Co_{5.0}$ alloy is shown, recorded by means of total electron yield detection. The L edge resonances for Fe and Co and the M edge resonances for Tb are indicated in different colors. (c) Fine structure of the Fe L_3 resonance in a partially oxidized Fe thin film, illustrating the chemical specificity of X-ray absorption spectroscopy.

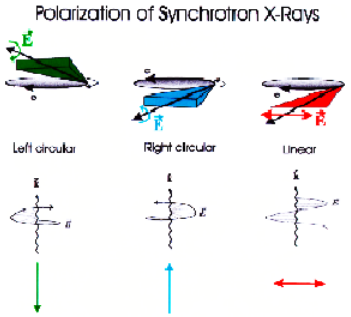

Fig. 3. Origin of polarized synchrotron radiation from a bending magnet source. If radiation in the plane of the electron orbit is selected by a suitable aperture, linearly polarized radiation is obtained as illustrated on the right side of the figure. By selecting radiation below or above the orbit plane, right- or left-handed circularly polarized radiation is obtained, as explained in the text. Linear polarization can be described by a biaxial vector and handed circular polarization by a vector, the photon spin.

Surface Review and Letters, Vol. 5, No. 6 (1998) 1297–1308

PRINCIPLES OF X-RAY MAGNETIC DICHROISM SPECTROMICROSCOPY

H. A. PADMORE, S. ANDERS and T. STAMMLER

J. STÖHR M. R. SCHEINFEIN

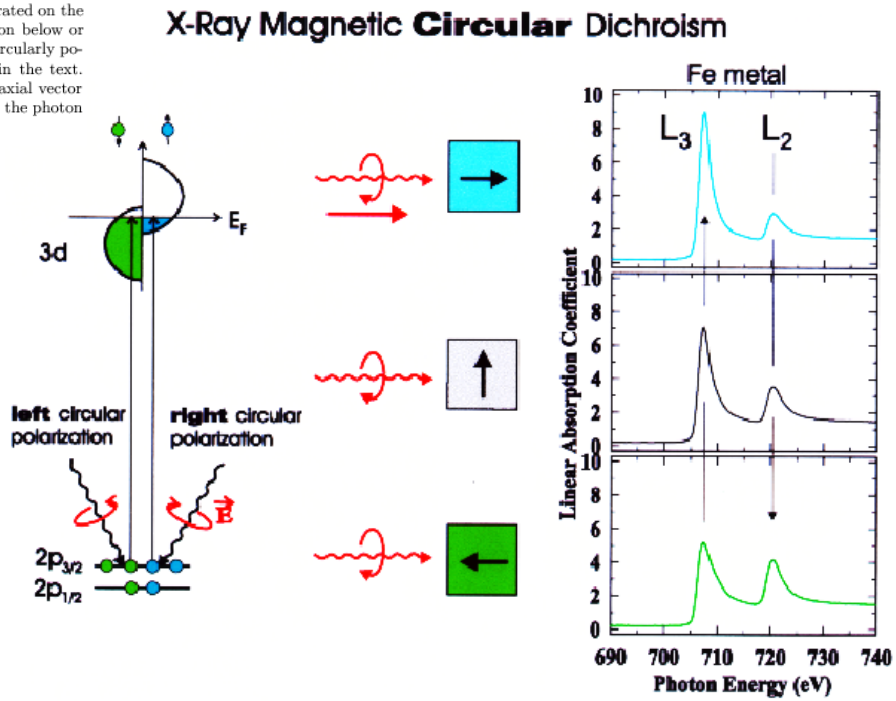

Fig. 4. Principles of X-ray magnetic circular dichroism spectroscopy, illustrated for the case of L edge absorption in a d band transition metal. In a magnetic metal the d valence band is split into spin-up and spin-down states with different occupation. Absorption of right (left) circularly polarized light mainly excites spin-up (spin-down) photoelectrons. Since spin flips are forbidden in X-ray absorption, the measured resonance intensity directly reflects the number of empty d band states of a given spin. In XMCD spectroscopy it is equivalent whether the photon polarization is changed and the magnetization direction is kept fixed or whether the magnetization direction is changed and the photon helicity is fixed. The corresponding XMCD spectra for Fe metal[44] are shown on the right for three different orientations of the magnetization directions relative to the fixed photon spin (right circular polarization).

X-PEEM

Técnicas

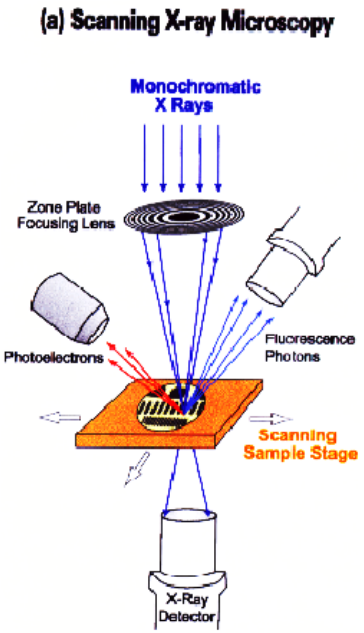

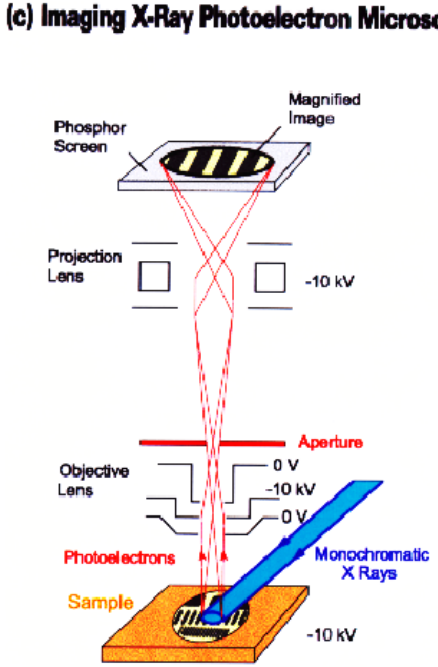

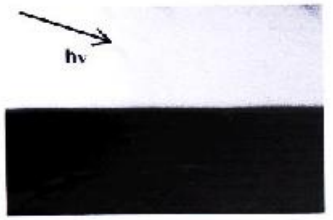

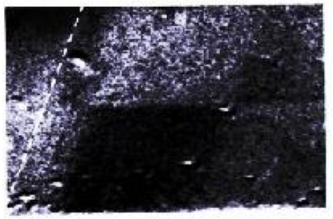

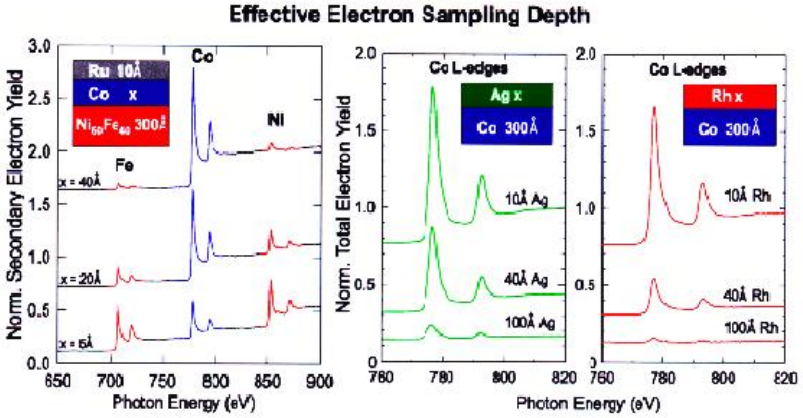

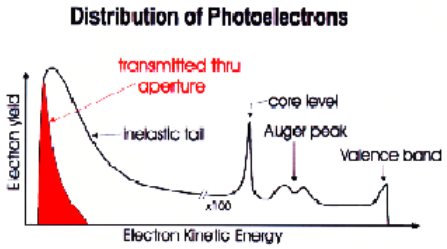

Fig. 7. (a) Schematic illustration of the photoelectron energy distribution from the sample after X-ray excitation. The photoemission spectrum is dominated by the low energy, scattered electrons (inelastic tail). The aperture in the backfocal plane of the PEEM shown in Fig. 6(c) leads to an electron-energy-filtering effect, so that only the electron intensity shown in red is transmitted.

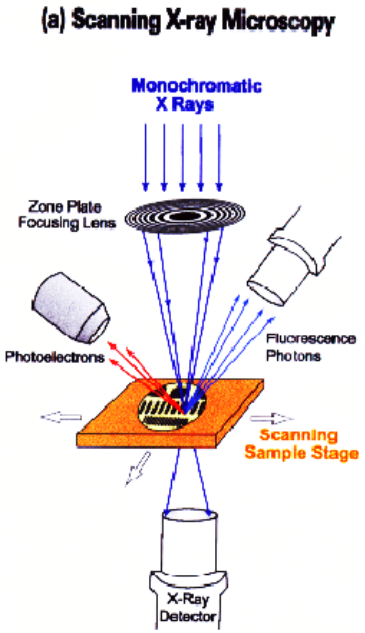

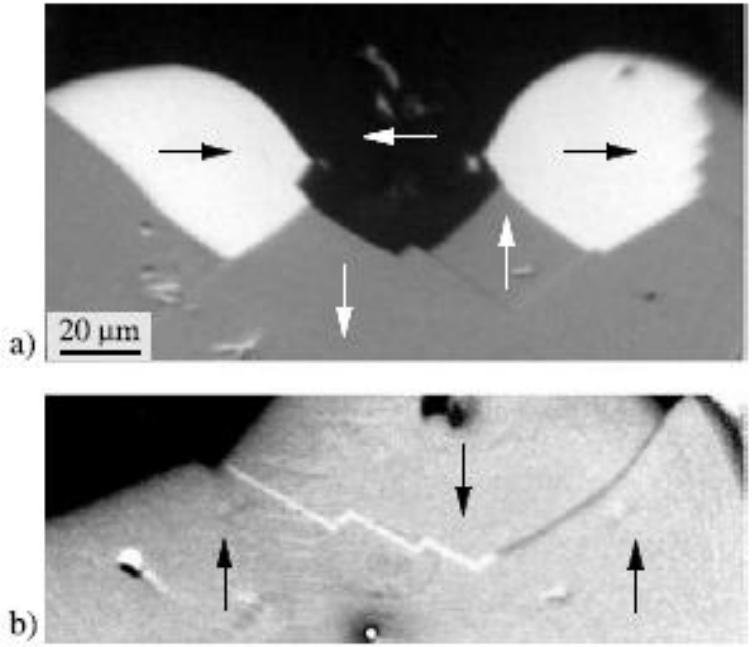

Fig. 2.51. Domain image on a mechanically stressed iron whisker, generated by circularly polarized soft X-rays from the ESRF synchrotron (Grenoble) entering in the picture from the right. The produced photoelectrons (of several eV energy) are collected by an advanced photoemission electron microscope [465]. (**a**) An overview of the domain pattern. (**b**) Details of V-line walls. (Courtesy *R. Frömter* and *C.M. Schneider* [459])

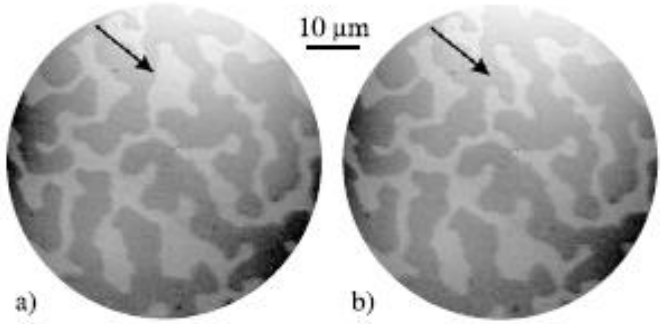

Fig. 2.52. Domains on an amorphous $Fe_{72}Gd_{28}$ film of 60 nm thickness and perpendicular anisotropy, made visible using X-ray dichroism on the Fe L_3 edge. Each picture was recorded in 3.5 sec, (**b**) 100 sec later than (**a**), thus displaying the process of domain creeping. (Courtesy *P. Fischer* and *T. Eimüller*, Augsburg; [471])

X-PEEM

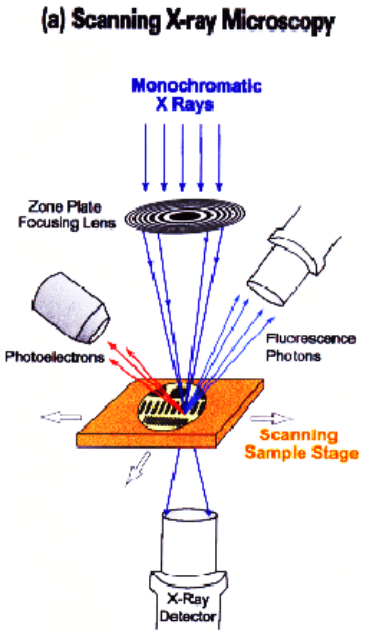

APPLIED PHYSICS LETTERS 97, 022501 (2010)

Tailoring magnetic vortices in nanostructures

F. Garcia,[1,a)] H. Westfahl,[1] J. Schoenmaker,[1] E. J. Carvalho,[1] A. D. Santos,[2] M. Pojar,[3] A. C. Seabra,[3] R. Belkhou,[4,5] A. Bendounan,[4] E. R. P. Novais,[6] and A. P. Guimarães[6]

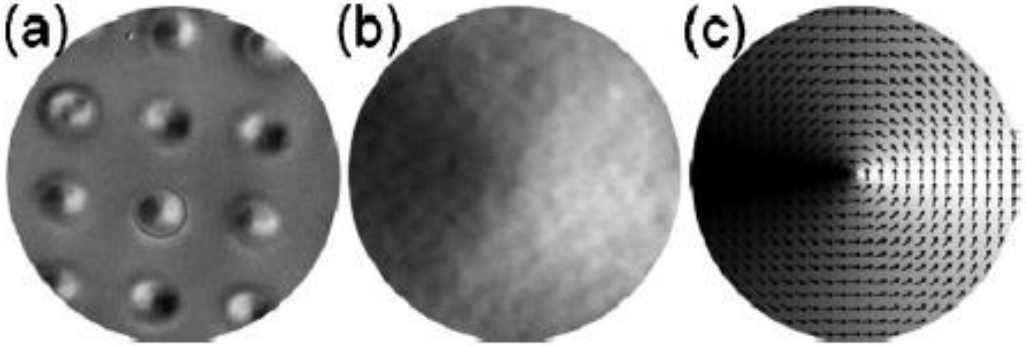

FIG. 2. (a) Image obtained by XMCD-PEEM of the $[Co_2/Pt_2]\times 6$ 1 μm disk array. (b) Detail of the disk highlighted by the red circle, presenting a typical vortex pattern. (c) OOMMF simulation of a disk with the same characteristic, showing a good agreement with (a).

Elettra Synchrotron, Italy.

MO-SNOM

Técnicas

Microscópio ótico de varredura em campo próximo – modo magnetoótico

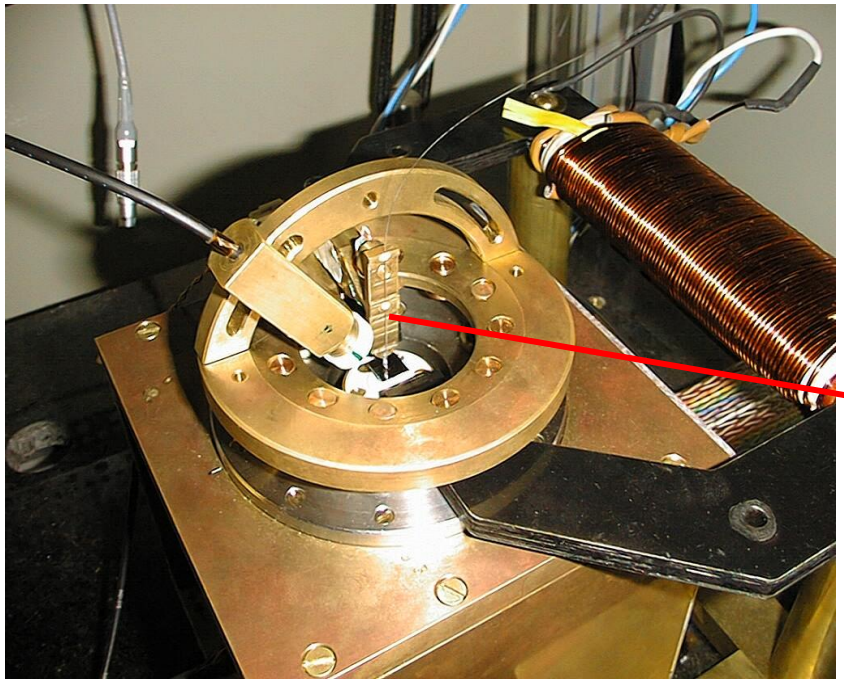

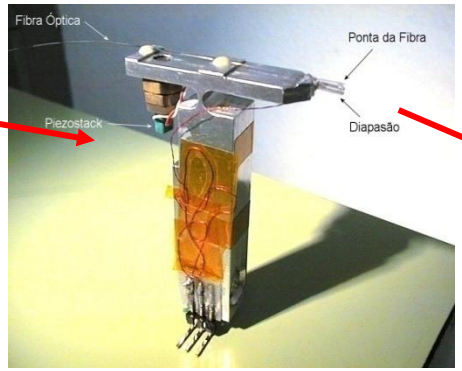

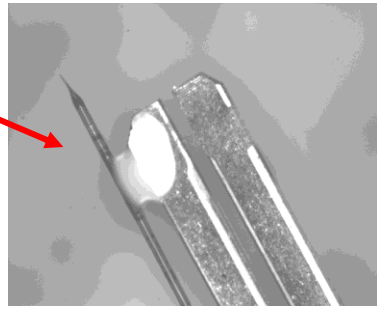

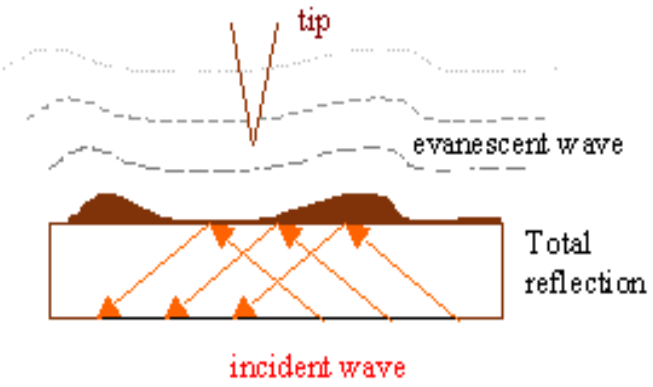

Distância ponta-amostra << λ (tipicamente ~ λ/60)

SNOM baseia-se em ondas evanescentes (não propagativas)

Resolução não é limitada pelo critério de Rayleigh

- ✓ Alta resolução ótica
- ✓ MOKE fornece alta sensibilidade magnética
- ✓ Possibilidade de aplicação de campos magnéticos durante as medidas
- ✓ Baixo Custo

Características Gerais

Técnicas

Method of domain observation	Sensitivity to small variations in magnetization	Evaluation of the magnetization vector	Allowed magnetic field range	Sample preparation quality requirements	Necessary capital investment
Bitter	very good	indirect	100 A/cm	moderate–low	low
Magneto-optic	fair	direct	any	high	moderate
Digital MO	good	quantitative	any	moderate	high
Defocused TEM	very good	indirect	3000 A/cm	high	high
Differential TEM	good	quantitative	1000 A/cm	high	very high
Holograph. TEM	good	quantitative	100 A/cm	very high	very high
Secondary SEM	poor	indirect	100 A/cm	low	high
Backscatt. SEM	poor	rather direct	300 A/cm	moderate–low	high
Pol. SEM	good	quantitative	100 A/cm	very high	very high
X-Ray topography	poor	indirect	any	moderate	extremely high
Neutron	poor	indirect	any	low	extremely high
MFM	good	indirect	3000 A/cm	low	moderate

Fig. 2.57. Qualitative comparison between different domain observation methods

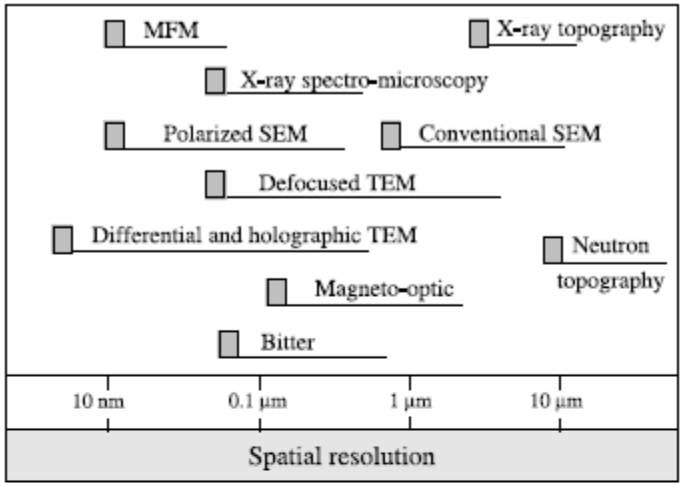

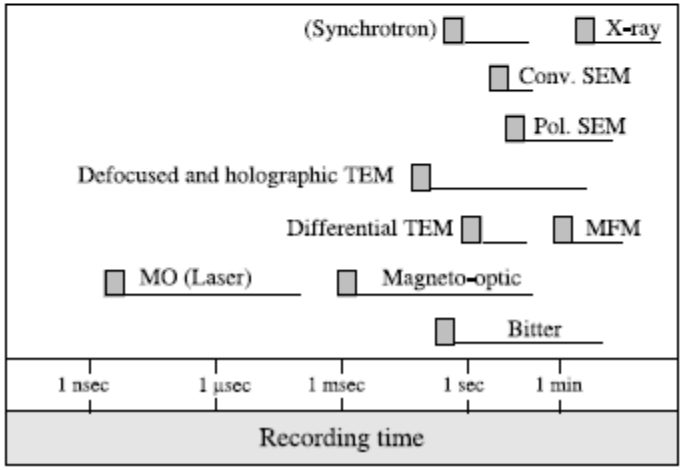

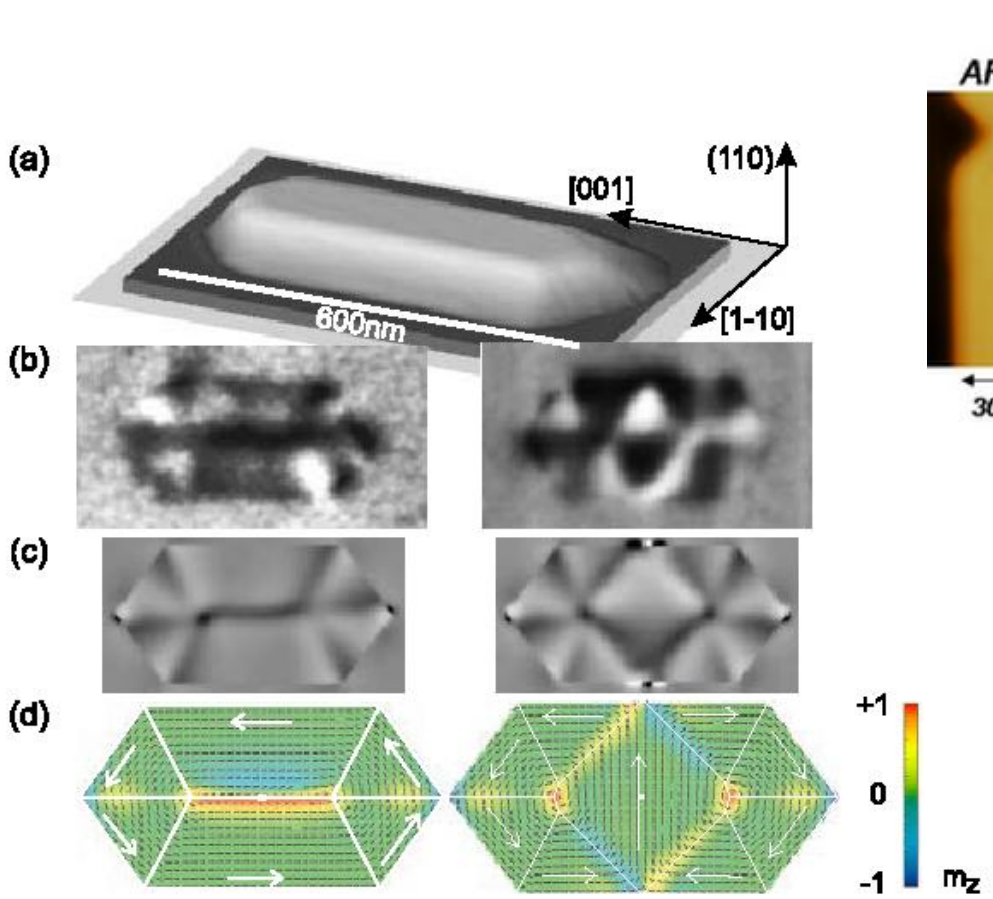

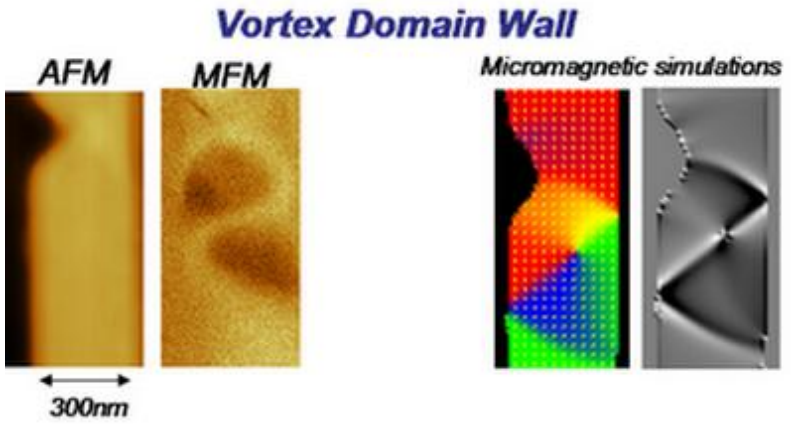

Fig. 1 – (a) 3D AFM image of a $600 \times 300 \times 60$ nm Fe dot (true vertical scale). Below are shown (b) experimental MFM images after saturation along [001], (c) simulated $\mathrm{d}H/\mathrm{d}z$ maps over the dot with a lift height of 30 nm, and (d) simulated configurations superimposed here with the Van den Berg construction, for both Landau (left) and diamond (right) states. Note the bipolar contrast of Néel walls and the unipolar contrast of the Bloch wall in (b)-(c). In (d) the color reveals the perpendicular component of magnetization of the mid-height plane, while white arrows sketch the in-plane magnetization direction.

Europhys. Lett., **63** (1), pp. 132–138 (2003)

MO-SNOM

Microscópio ótico de varredura em campo próximo – modo magnetoótico

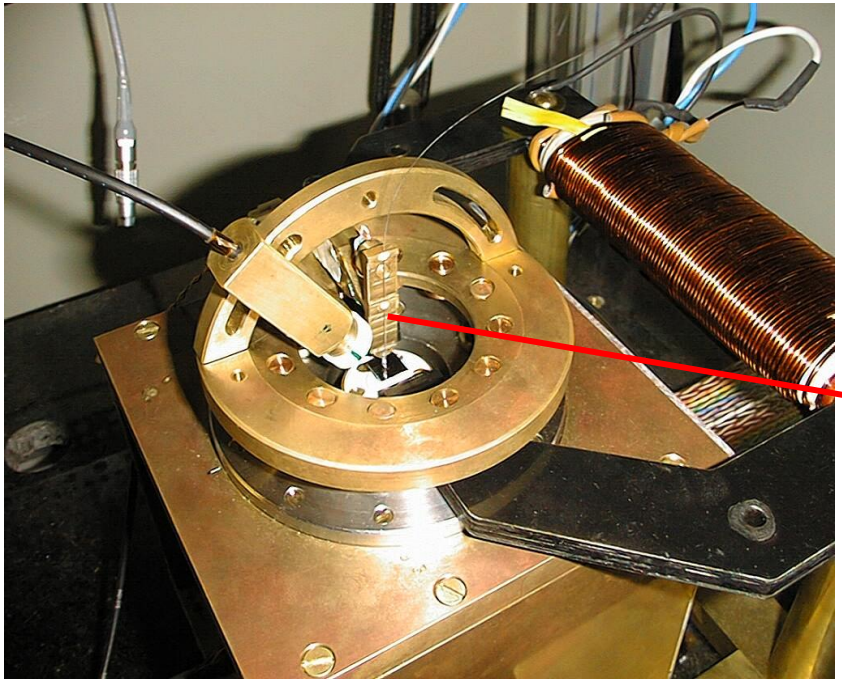

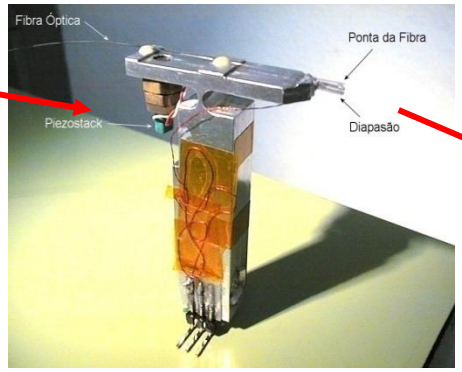

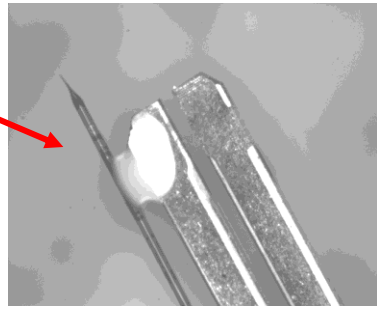

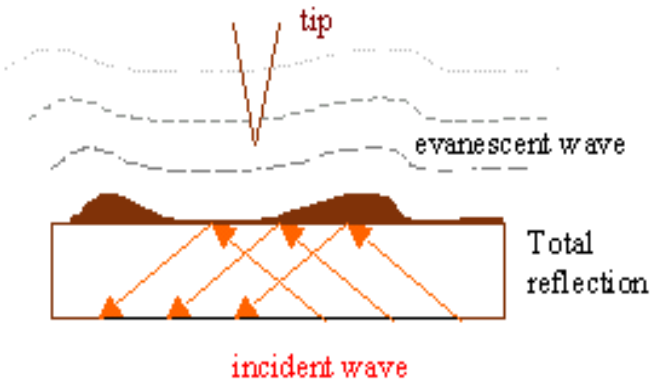

Distância ponta-amostra << λ (tipicamente ~ λ/60)

SNOM baseia-se em ondas evanescentes (não propagativas)

Resolução não é limitada pelo critério de Rayleigh

- ✓ Alta resolução ótica
- ✓ MOKE fornece alta sensibilidade magnética
- ✓ Possibilidade de aplicação de campos magnéticos durante as medidas
- ✓ Baixo Custo

MO-SNOM

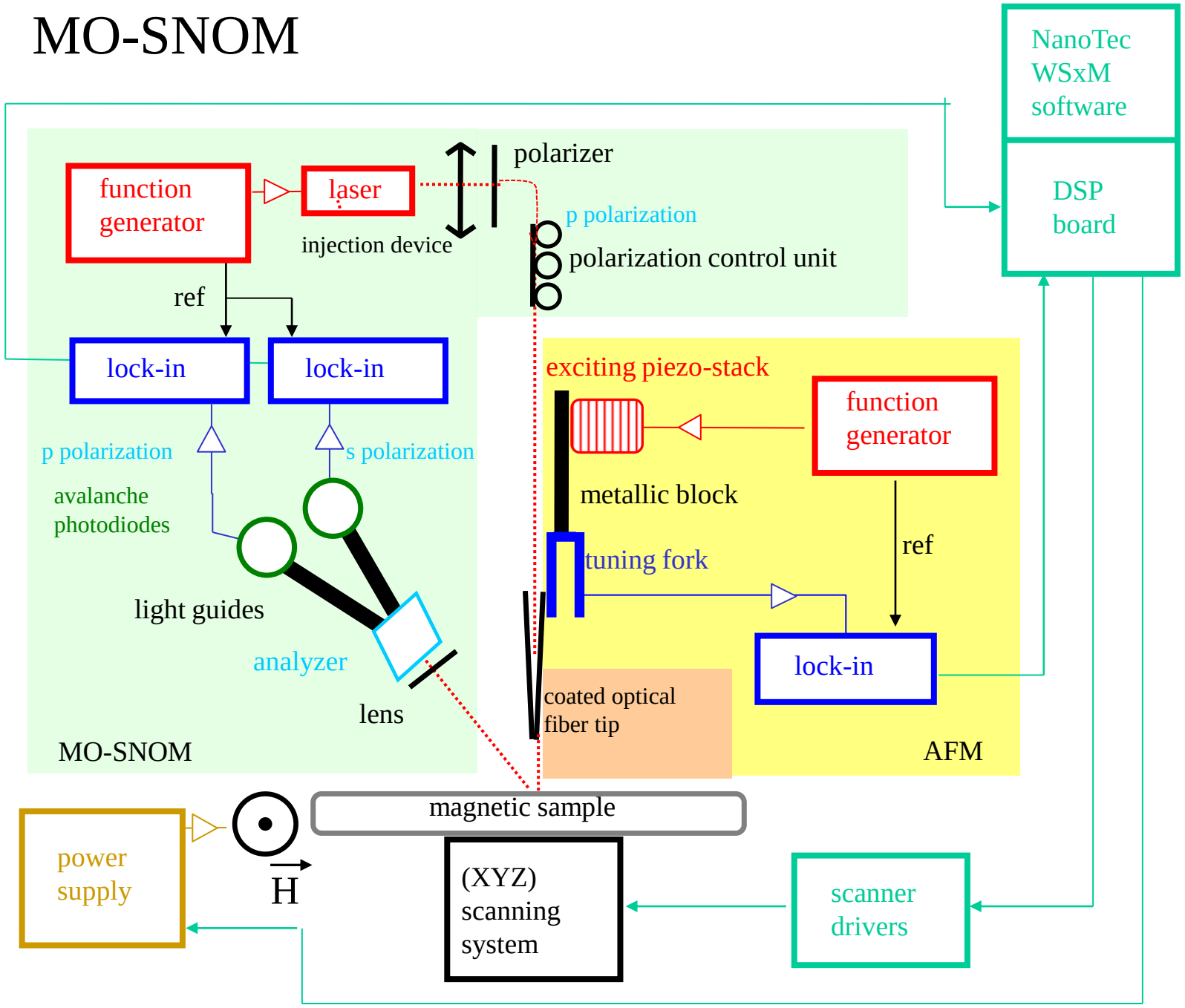
NanoTec
WSxM
software
DSP
board
function
generator
laser
injection device
polarizer
p polarization
polarization control unit
ref
lock-in
lock-in
p polarization
s polarization
avalanche
photodiodes
light guides
analyzer
lens
MO-SNOM
exciting piezo-stack
function
generator
metallic block
tuning fork
ref
lock-in
coated optical
fiber tip
AFM
magnetic sample
power
supply
H
(XYZ)
scanning
system
scanner
drivers

Preparação das Pontas

Ataque químico seletivo
NH_4F (40%): HF (48%): H_2O – 5:1:1

Camada de Au

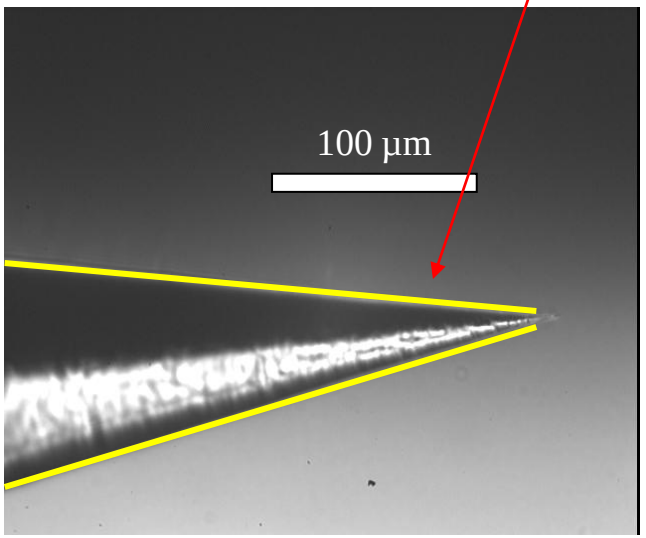

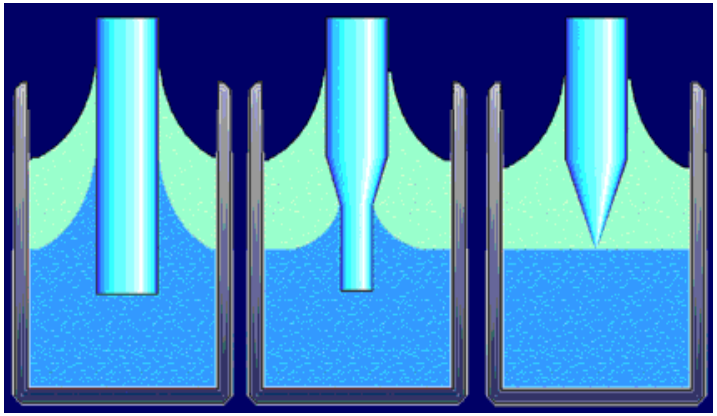

Microsc. Microanal., **11-3** (2005) 18

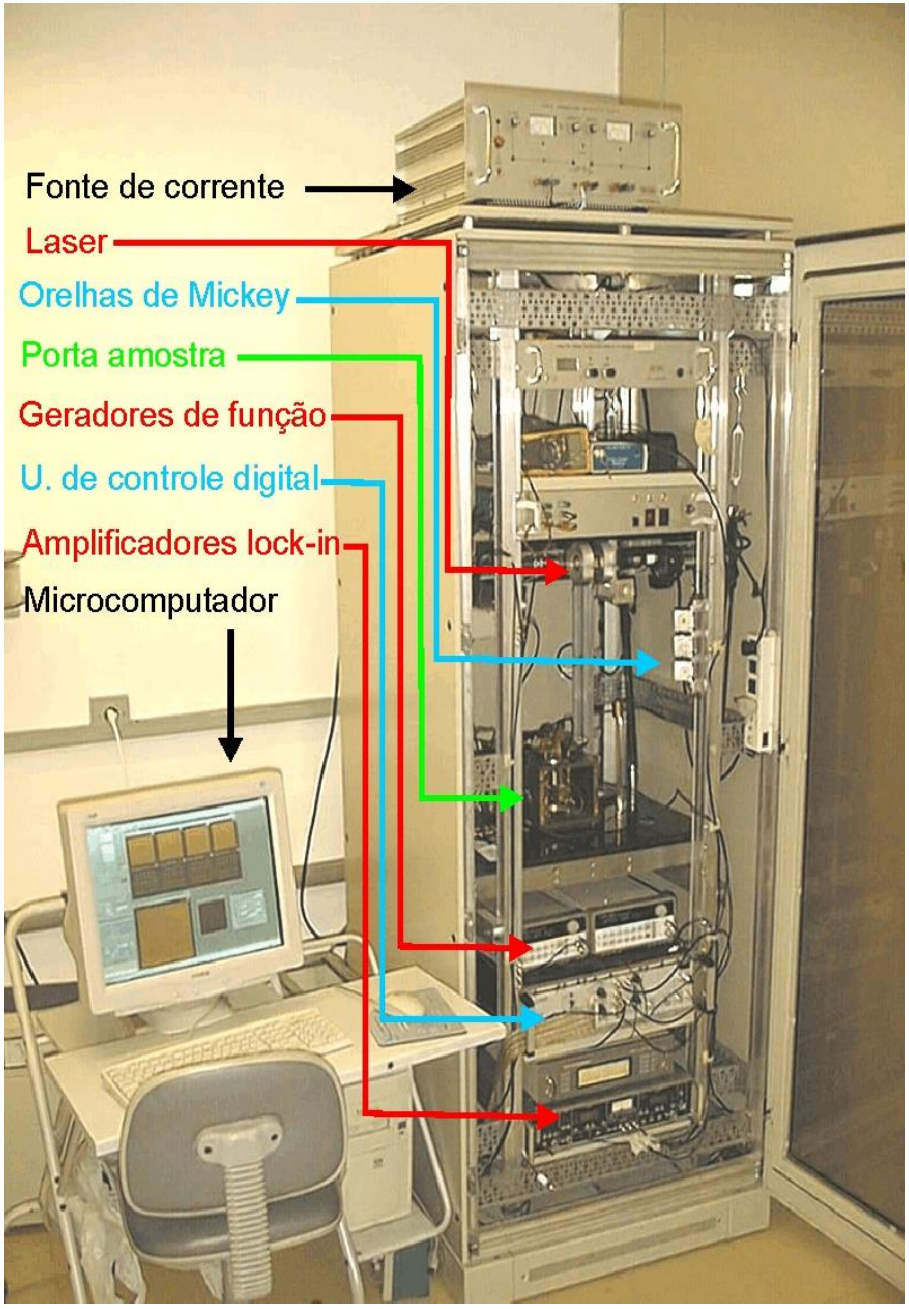
Fonte de corrente
Laser
Orelhas de Mickey
Porta amostra
Geradores de função
U. de controle digital
Amplificadores lock-in
Microcomputador

MO-SNOM

Amostras

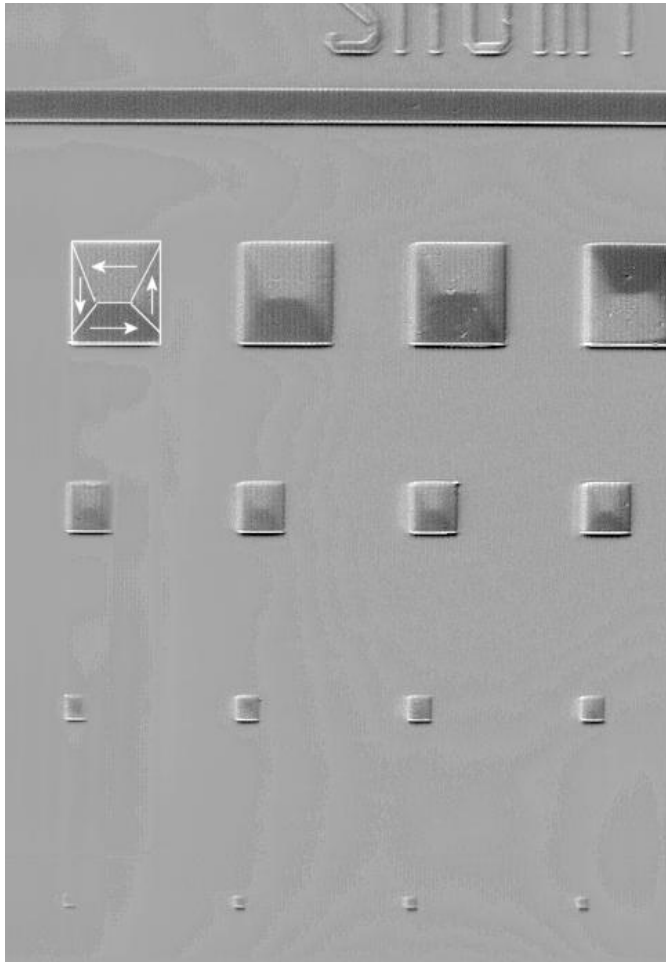

Litografia por feixe eletrônico e sputtering.

Objetos de CoFeSiB amorfo sobre substrato de Si.

Tamanhos entre 0,5 e 16 µm.

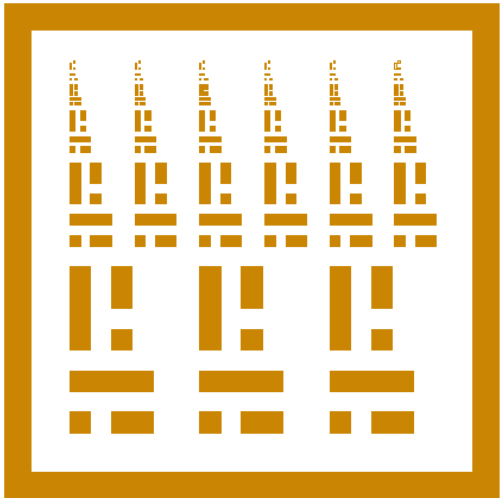

MO-SNOM (alguns resultados)

Objeto de 16x16x0,08 μm^3 de CoFeSiB amorfo sobre substrato de Si

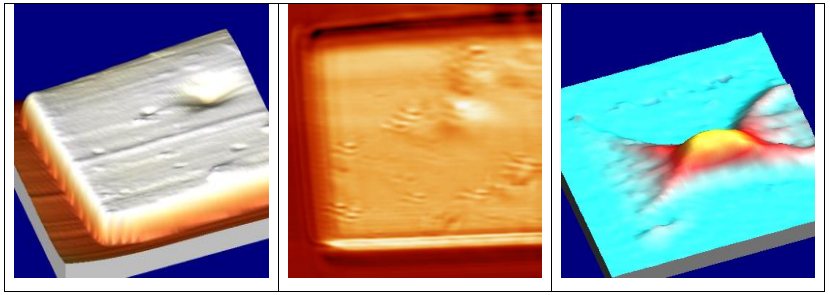

Topográfica (AFM) | Otica (SNOM) | Magnetoótica (MO-SNOM)

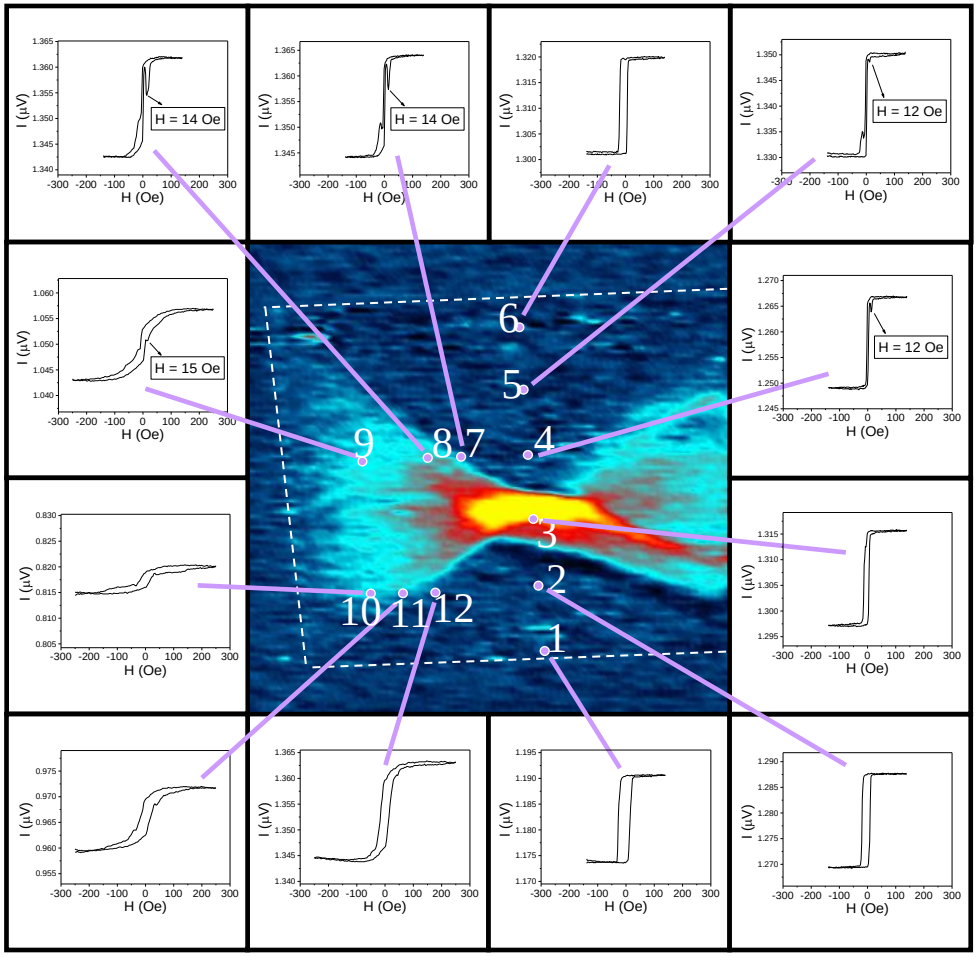

J. Microscopy, **214-1** (2004) 22

Obtenção de curvas de histerese no SNOM

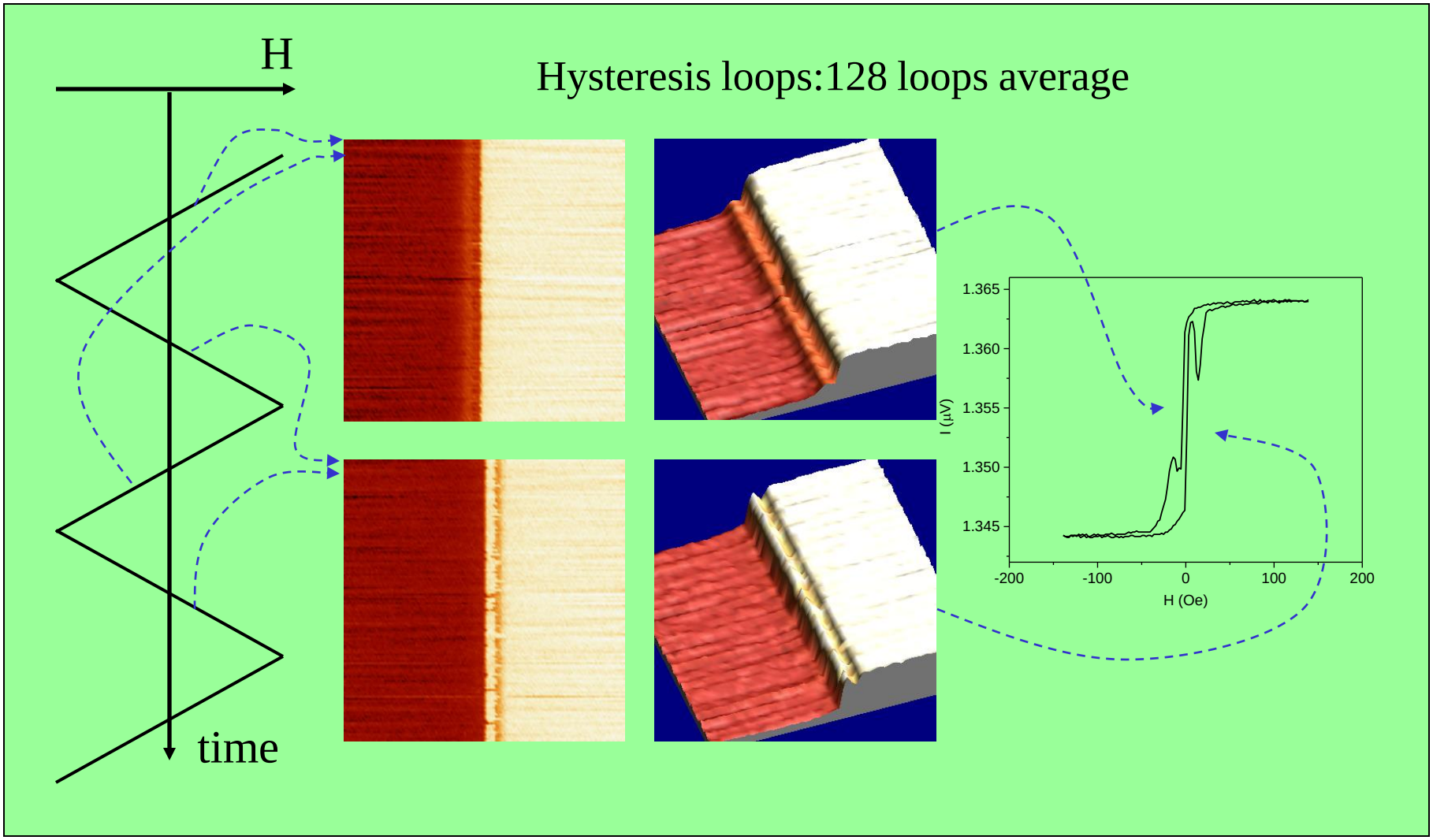

Local Hysteresis Loops

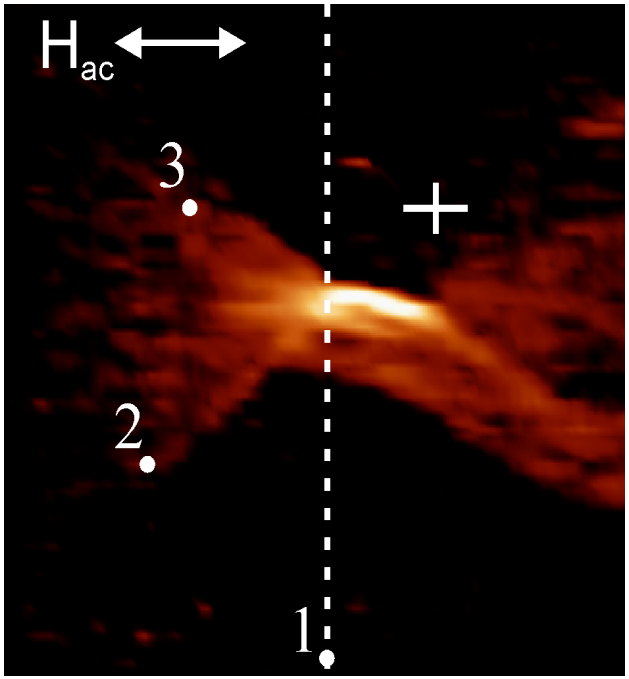

MODS image

(Magneto-Optical Differential Susceptibility)

freq. 155 Hz

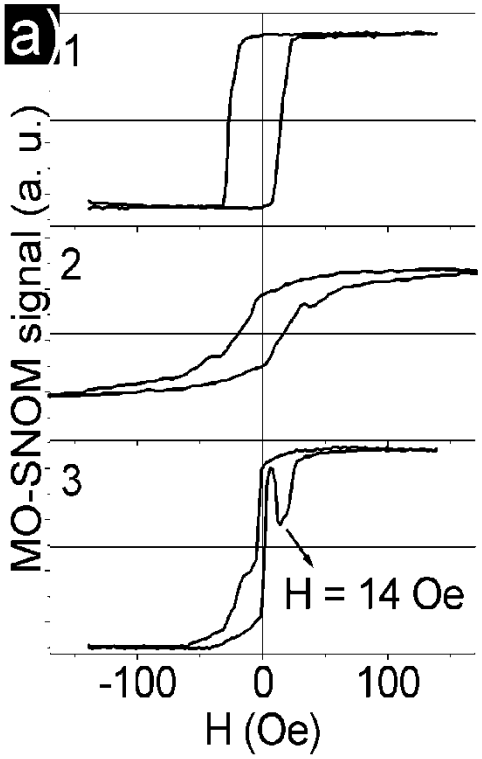

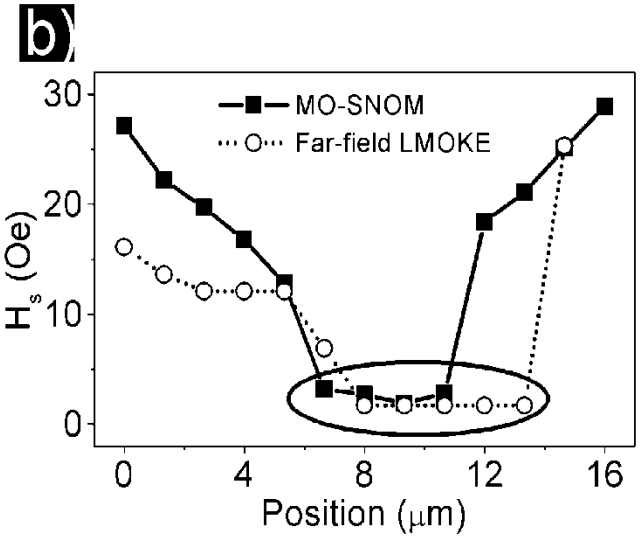

LHL

(Local Hysteresis Loops)

H_{max}: 450 Oe

Freq: 0.4 Hz

J. Appl. Phys. ***98*** (2005) 86108

Estudo Magnetoóptico em um objeto de 10x30 μm²

Estrutura de domínios

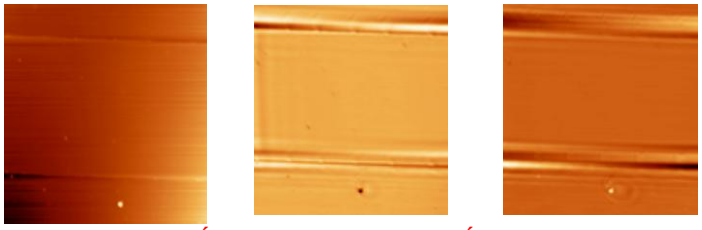

Topográfica 20 microns Óptica Kerr Transversal Óptica Kerr Longitudinal

Amplitude do sinal kerr transversal

Fase do sinal kerr transversal

Amplitude do sinal kerr longitudinal

Campo AC:

600mV

300mV

500mV

250mV

450mV

200mV

400mV

150mV

350mV

100mV

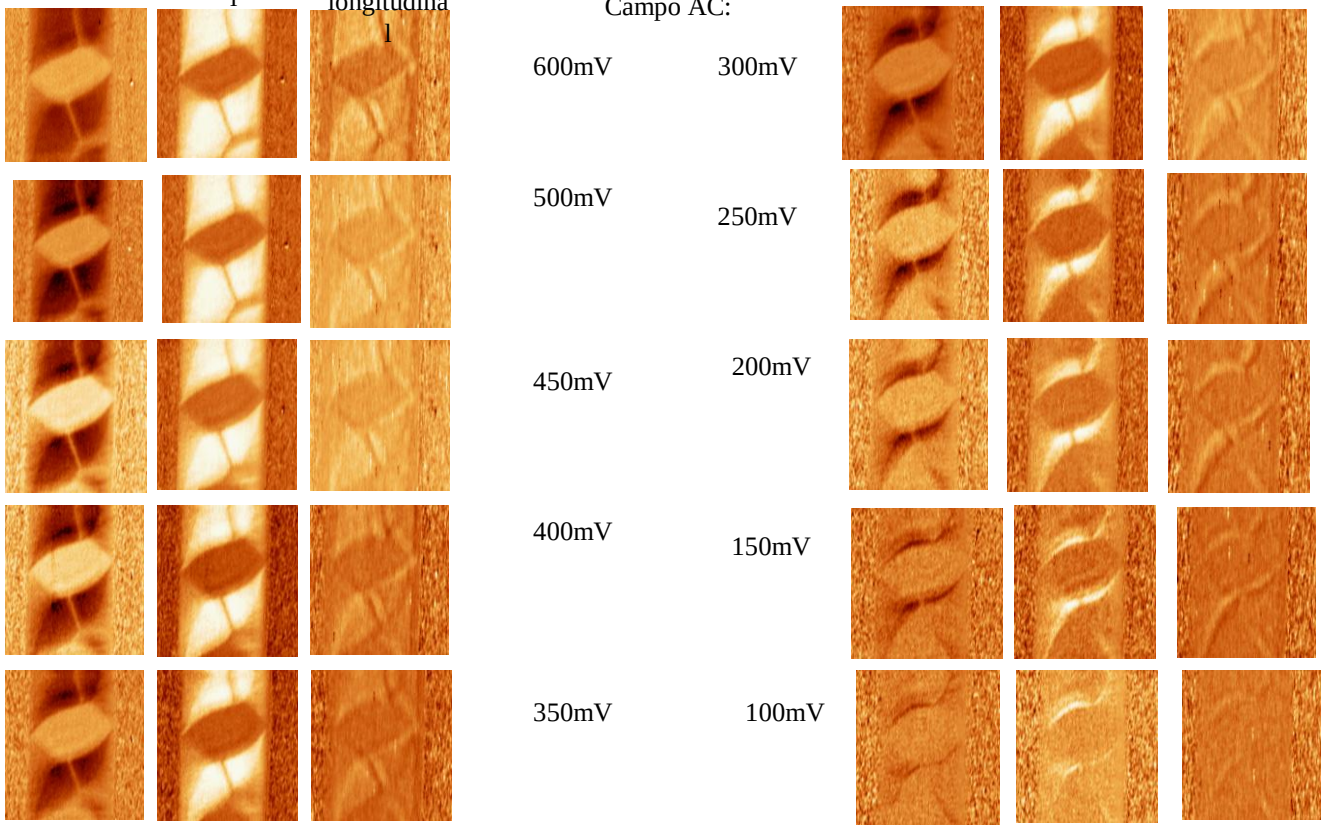

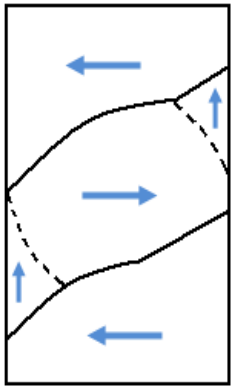

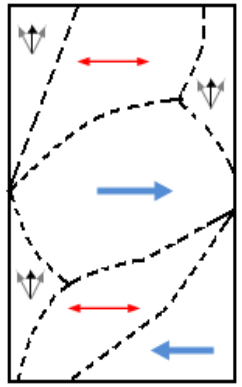

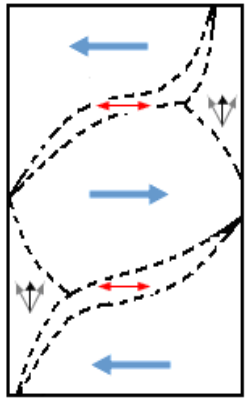

Magnetic Field Spectroscopy

Remanence MODS images (16x16 μm^2 particle)

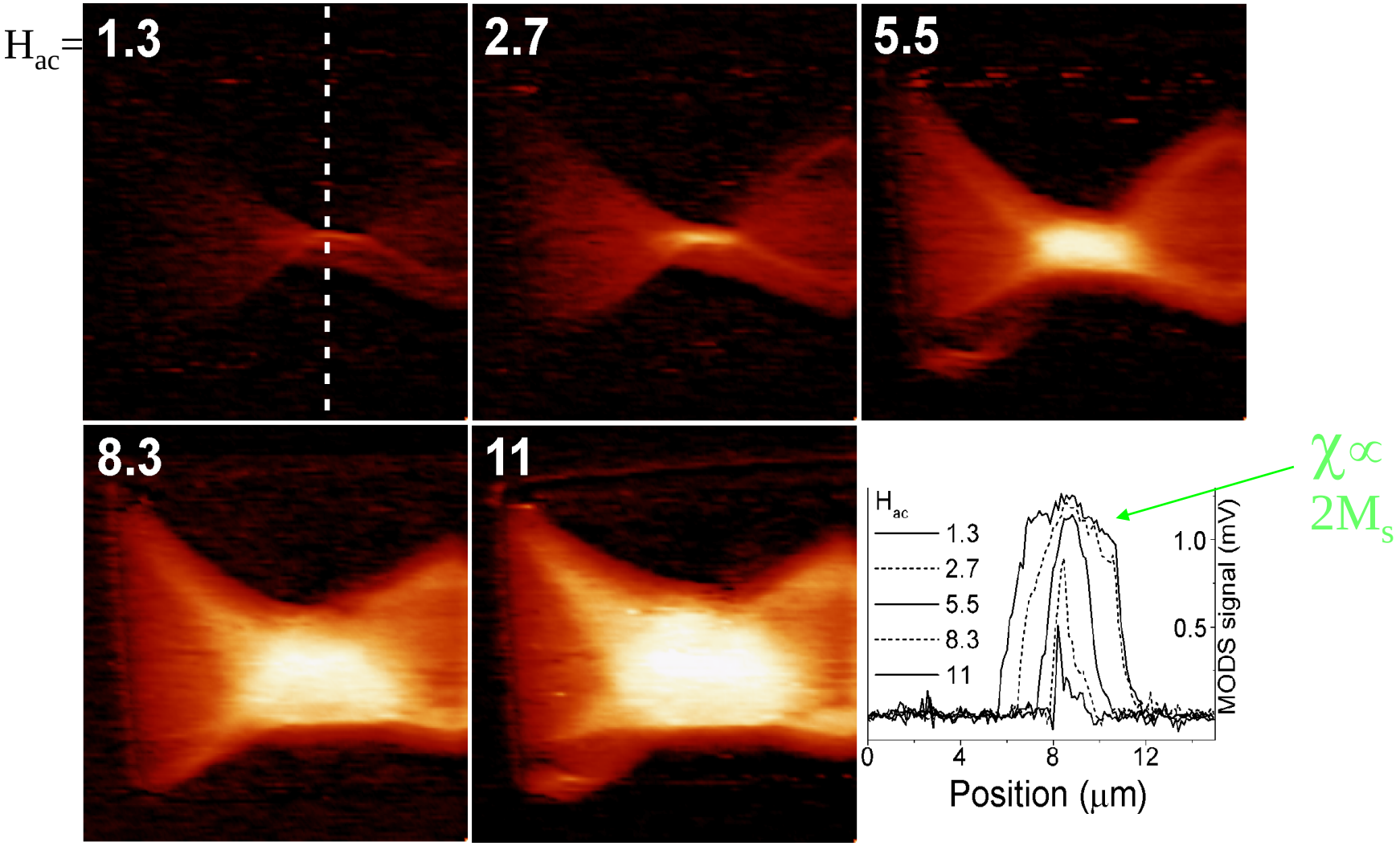

Magneto-optical Differential Susceptibility (MODS) Images

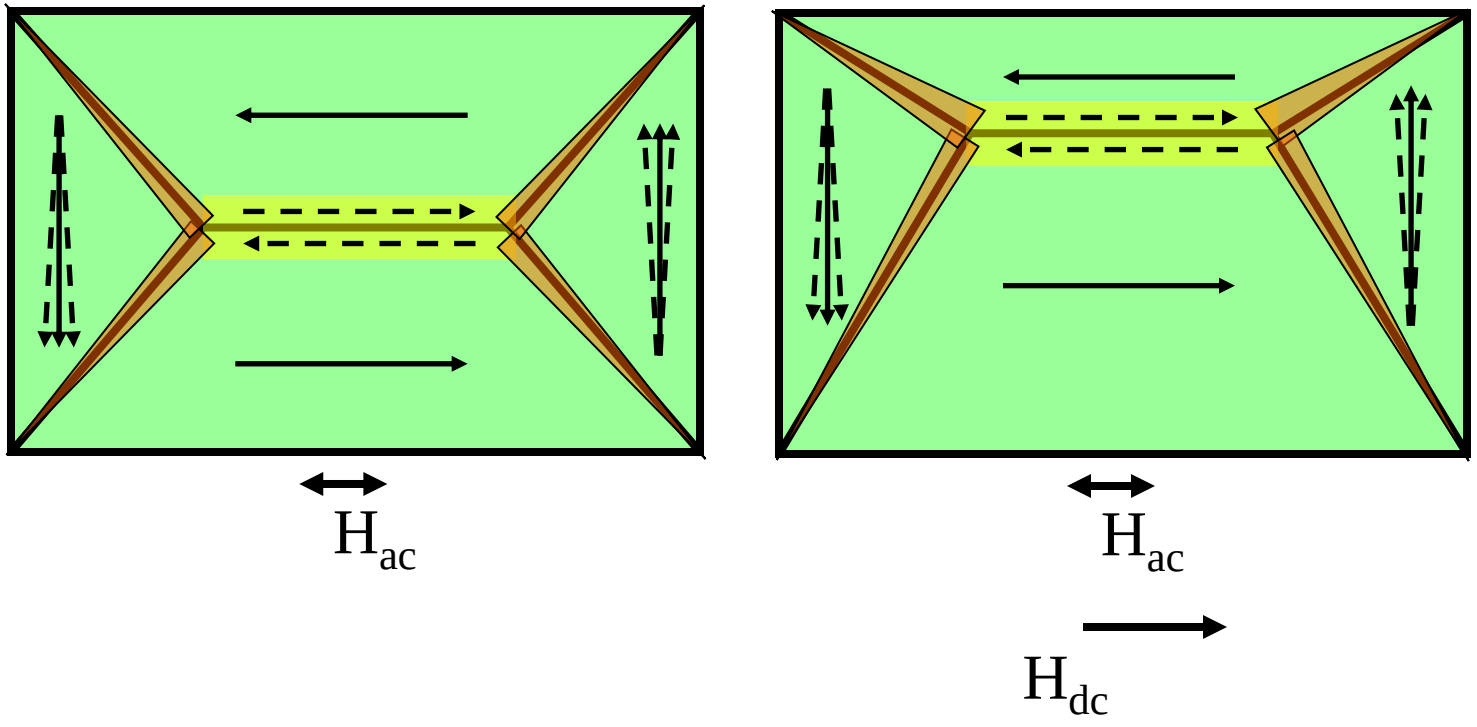

MODS Images:

Frequence:155 Hz and H_{dc} = 0 Oe

PADS (20 µm X 100 µm)

H_{ac} =

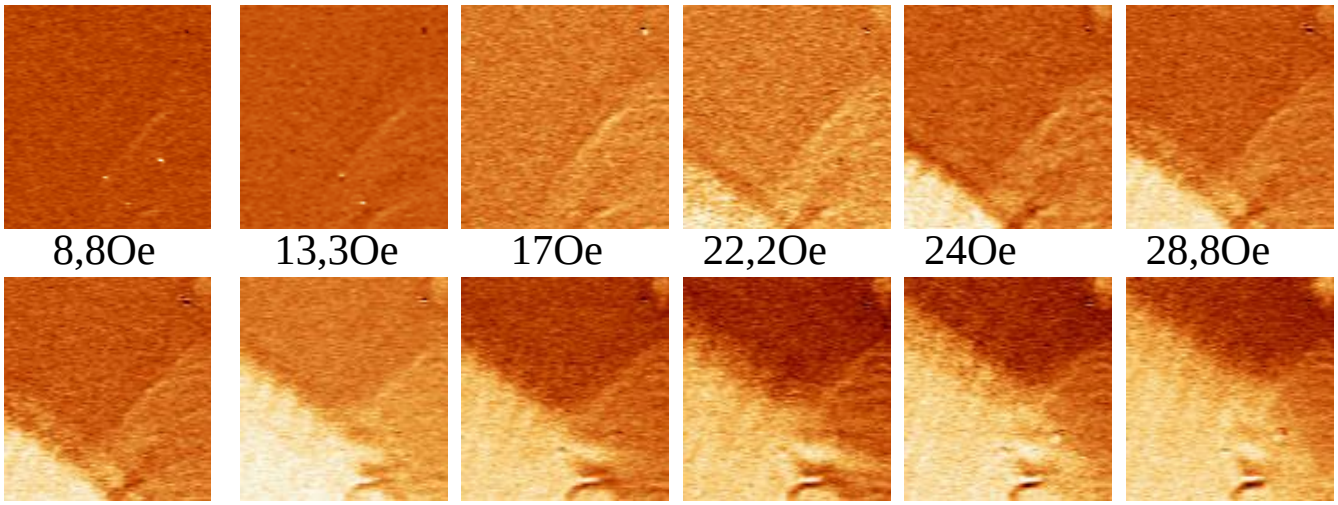

CoFeSiBNb

amorphous film

15x15 µm^2 images

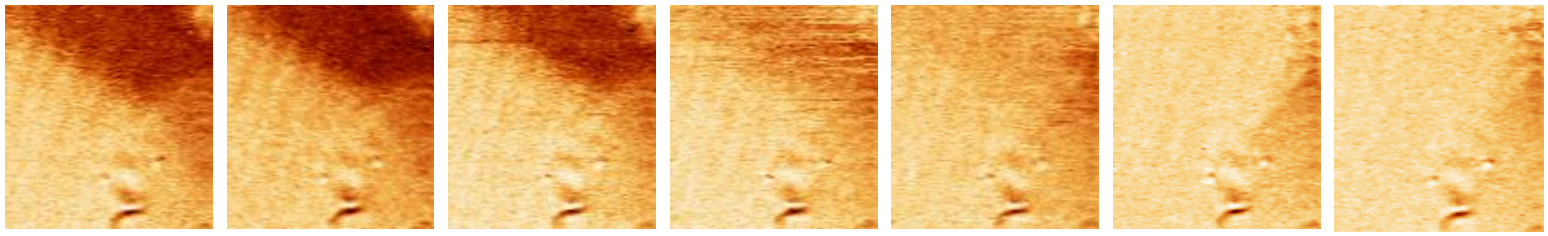

MODS Images

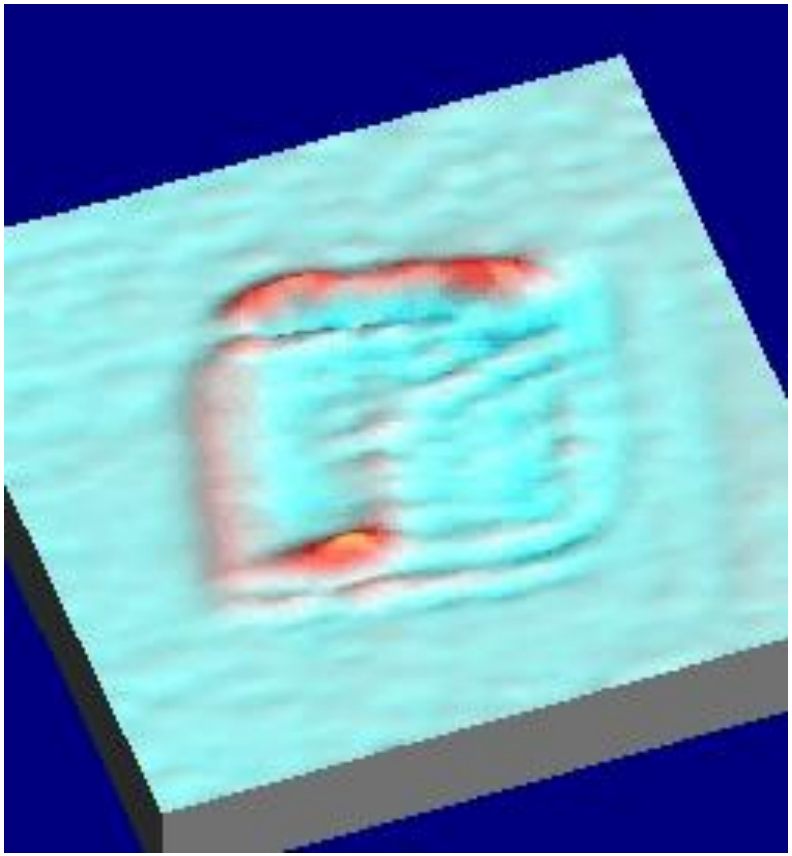

Partícula de 4x4x0,08 μm^3 de filme amorfo de CoFeSiB sobre substrato de Si

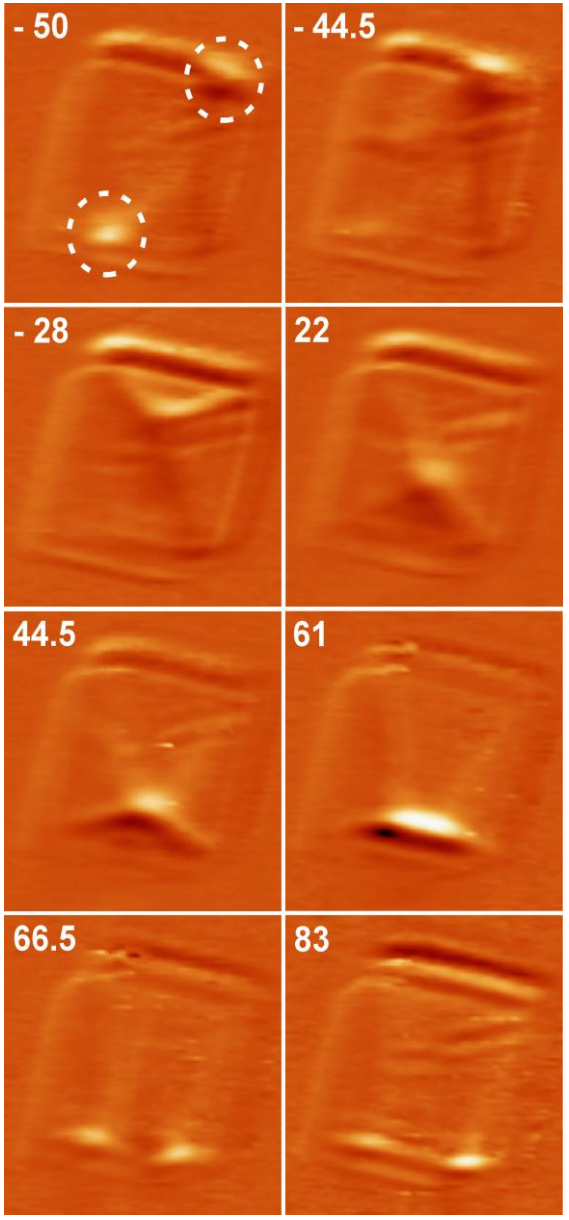

Appl. Phys. Lett., **88** (2006) 62506

Some MO-SNOM results

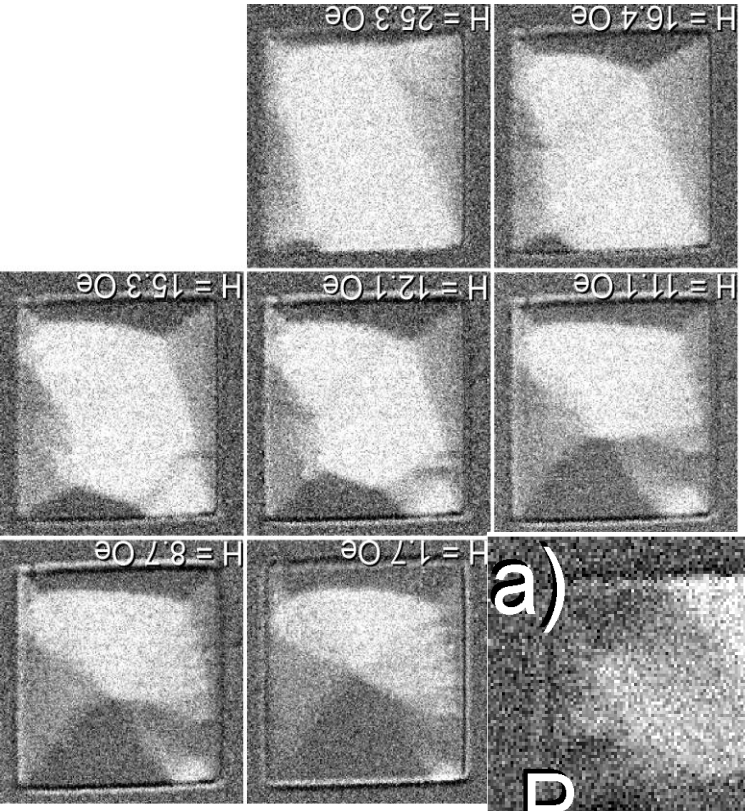

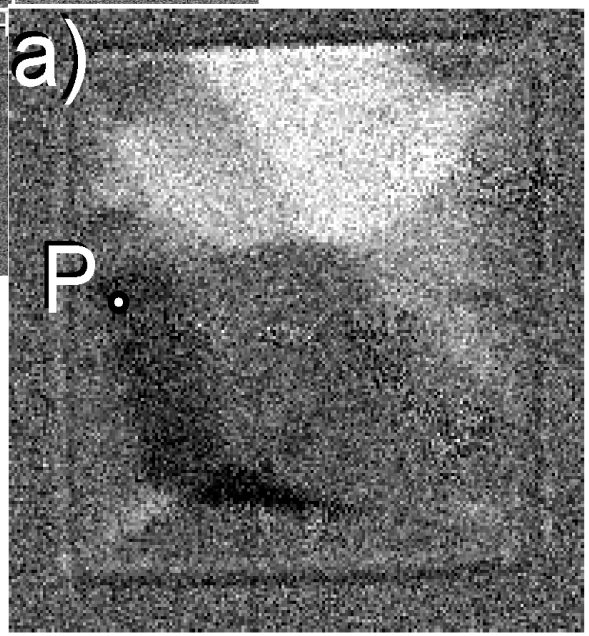

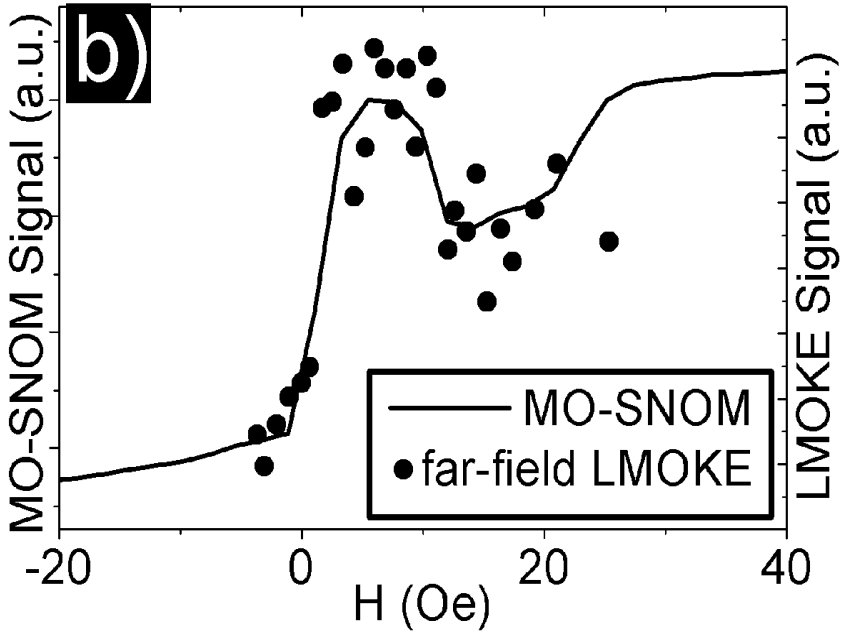

Microscopia Kerr longitudinal em campo-distante

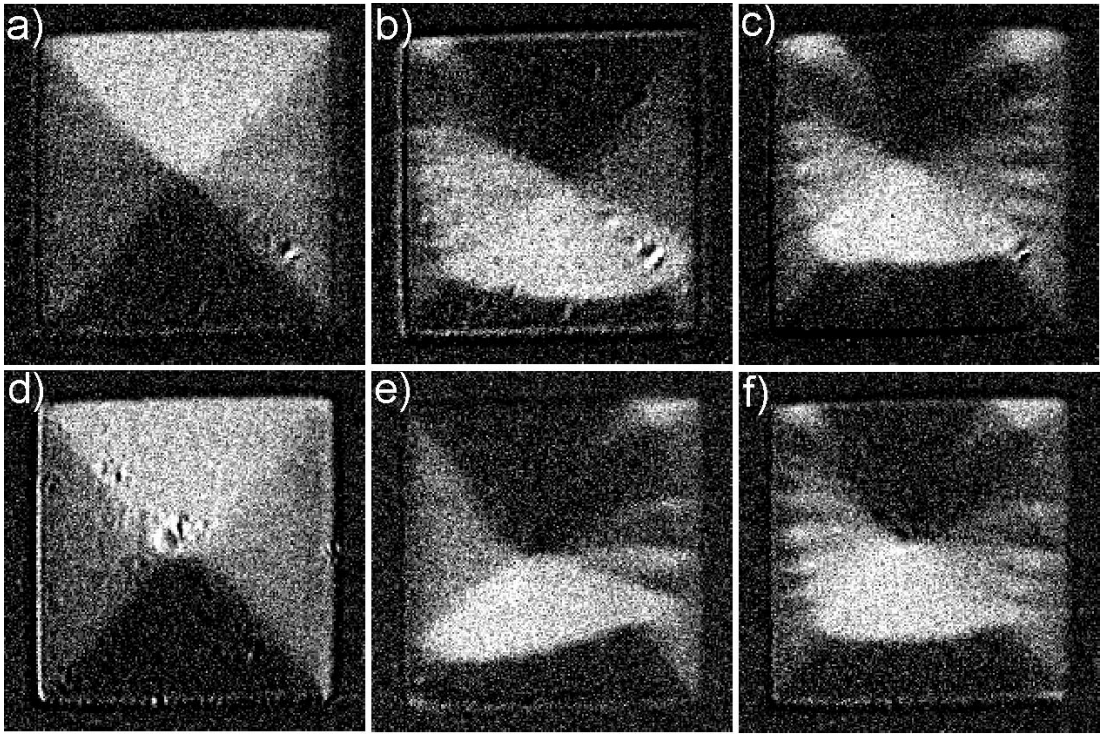

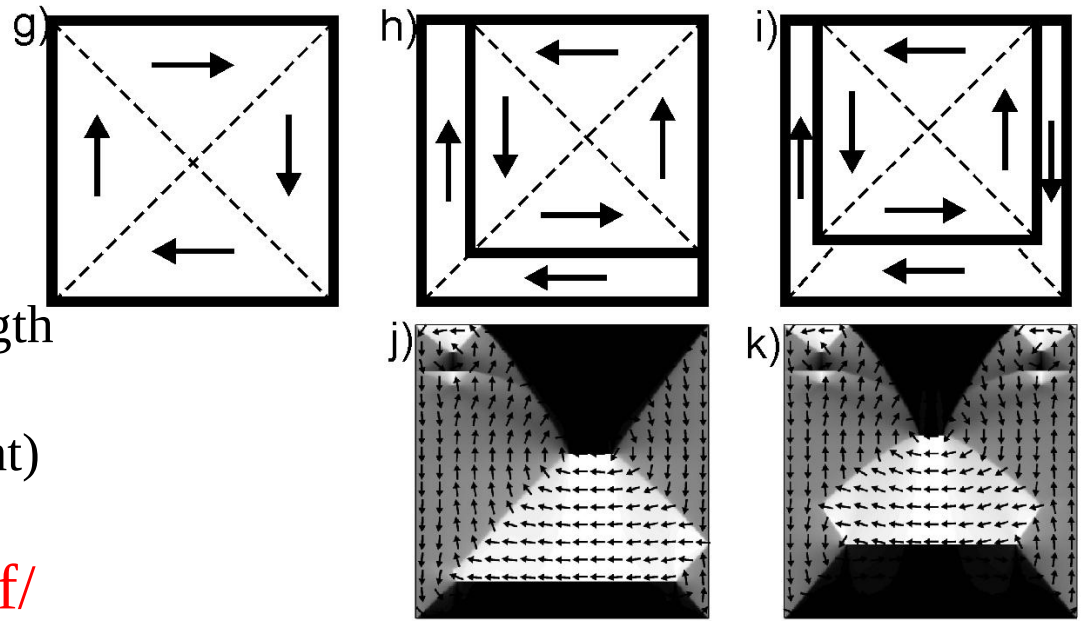

Programa OOMMF

320.000 cubic cells - 40 nm length

M_s = 800 kA/m

A = 10 pJ/m (Exchange Constant)

K = 600 J/m^3 (15 Oe)

http://math.nist.gov/oommf/

Simulações

Programa OOMMF

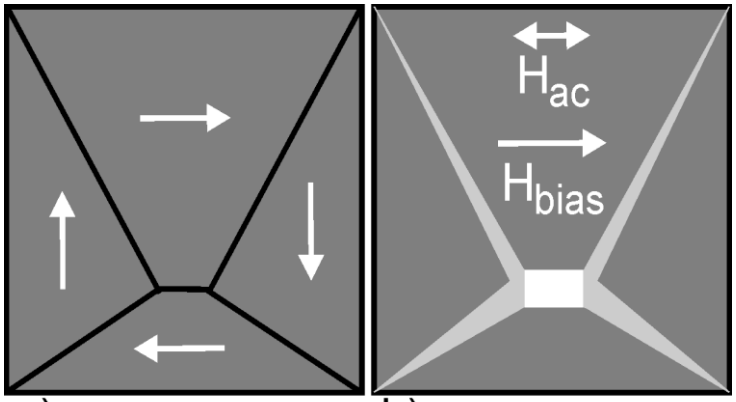

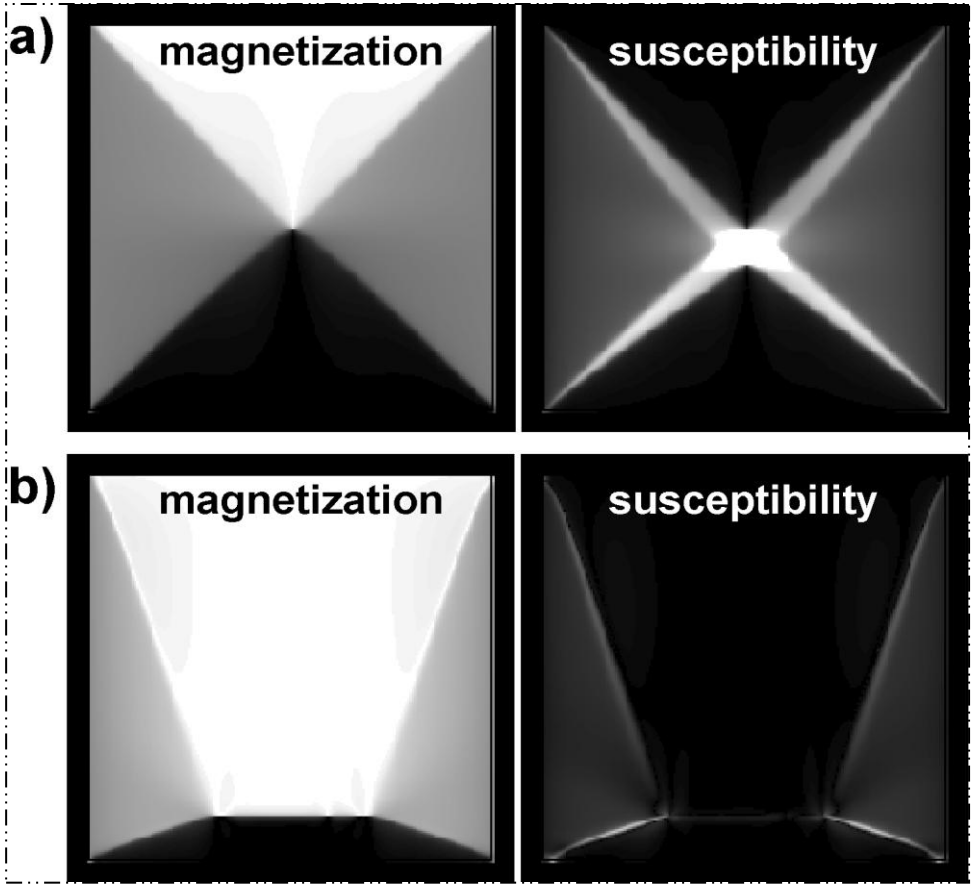

Simulações

Programa OOMMF

Imagens de susceptibilidade

Direção da Magnetização

Partícula de 2x2 μm^2

64 LHL

8x8 posições

Δl=125 nm

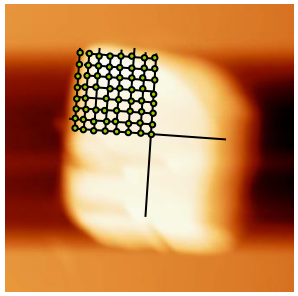

Sinal MOKE Longitudinal

e

Transversal

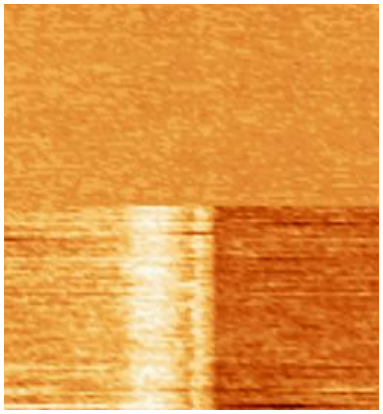

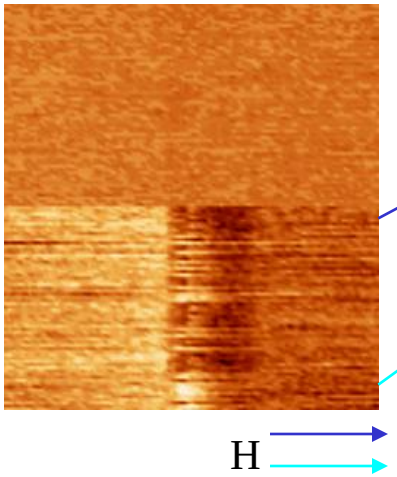

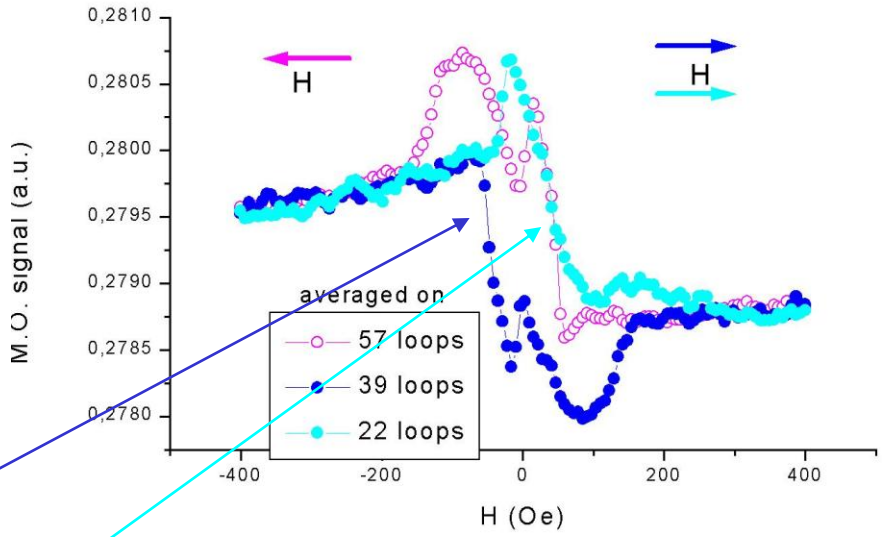

64 LHL
8x8 posições
Δl=125 nm

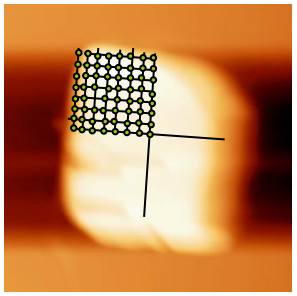

Direção da Magnetização

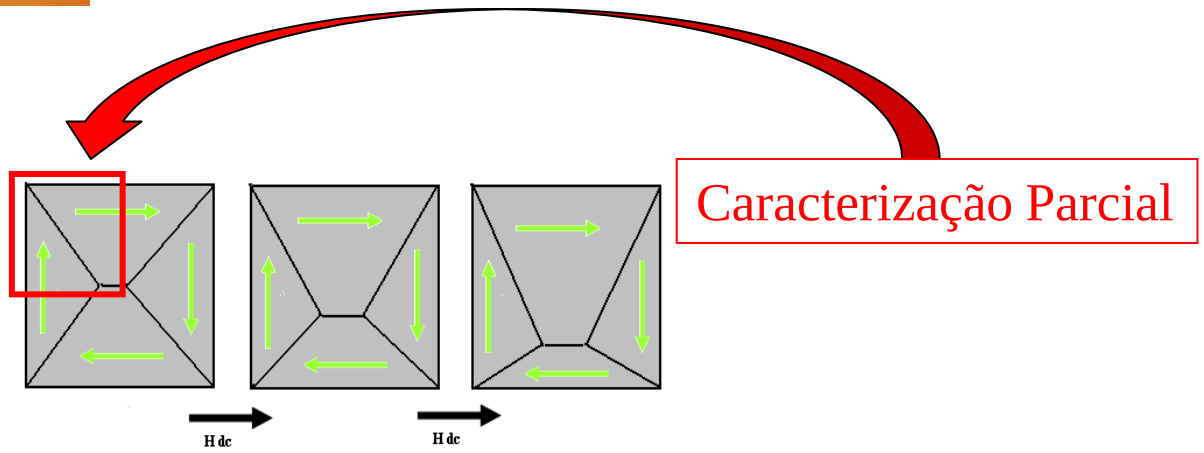

Duas quiralidades para a estrutura de domínios

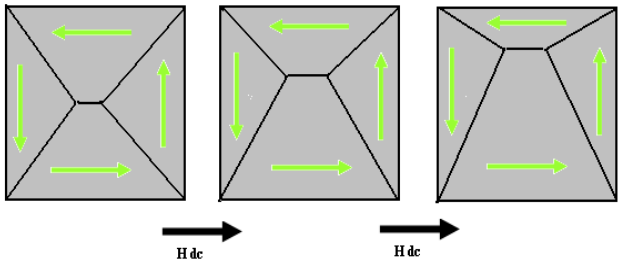

Gedanken Experiment:
particle with no coercivity

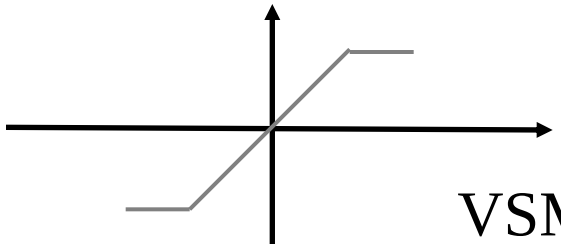

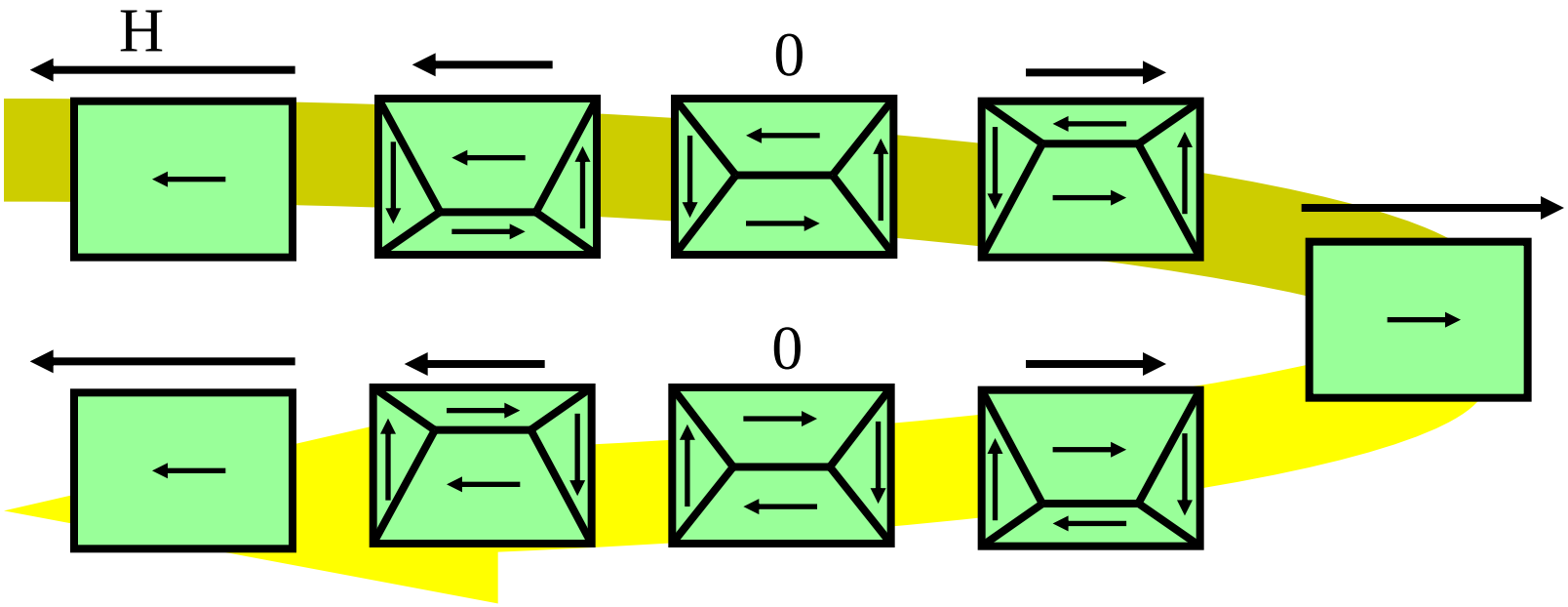

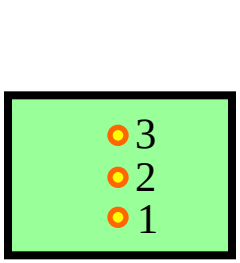

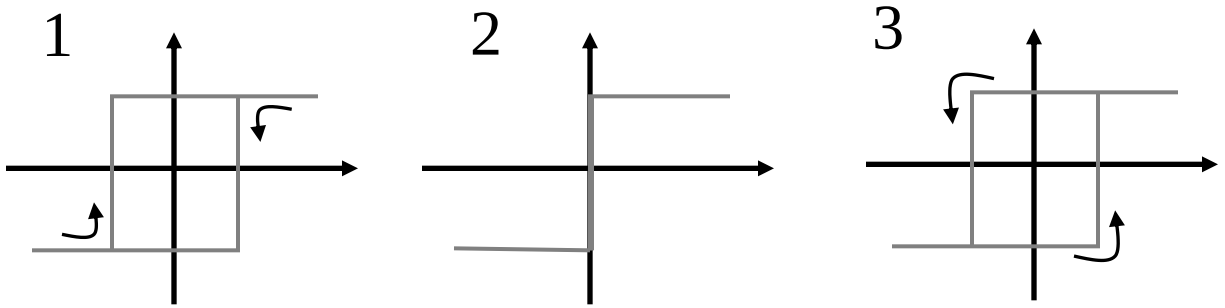

64 LHL
8x8 posições
Δl=125 nm

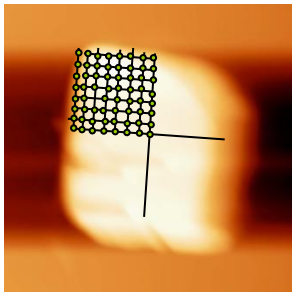

Direção da Magnetização

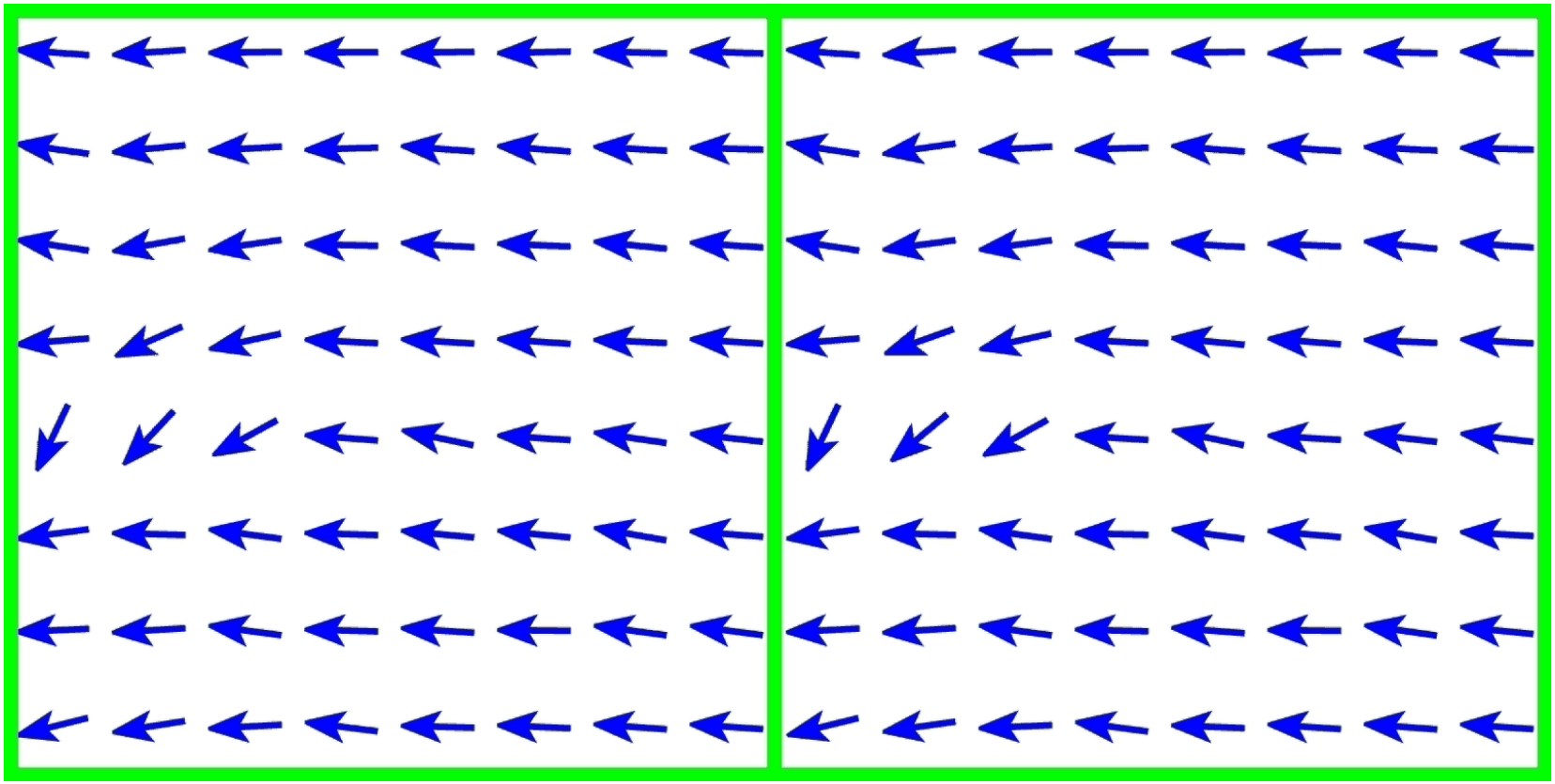

Energia Zeeman

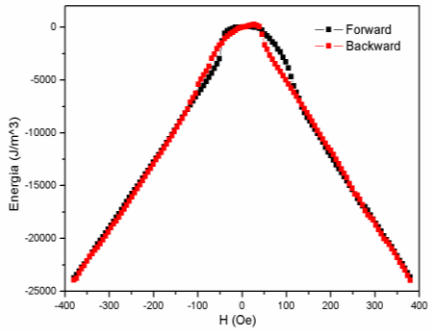

Energia de troca

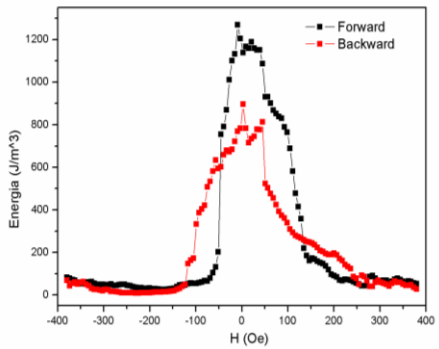

Campos de Reversão

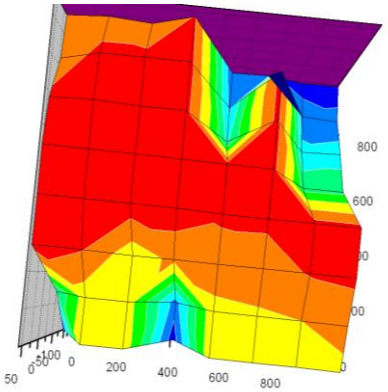

Ramo ascendente

Energia de anisotropia

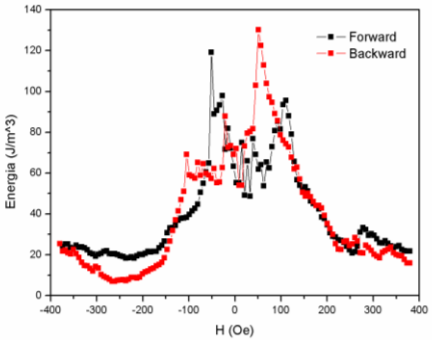

Energia desmagnetizante

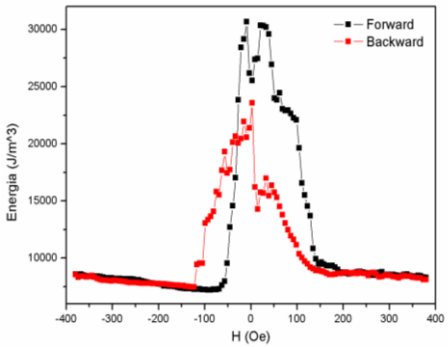

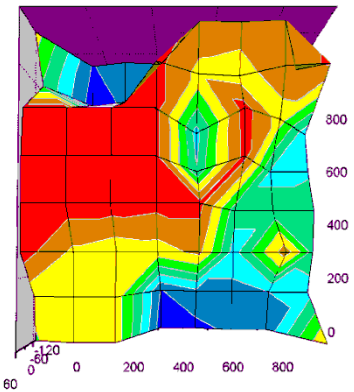

Ramo descendente

Energia total

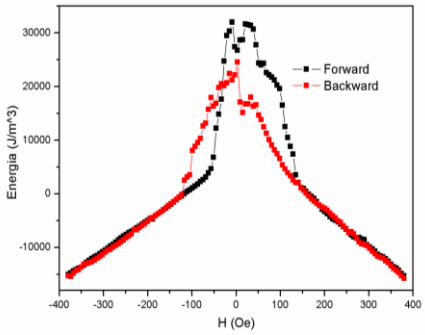

Sumário Parcial (MO-SNOM)

- Imagens topográficas (AFM) + óticas (SNOM) + magnetoóticas (MODS).
- Medidas de Curvas de Histerese Locais (LHL).
- Resolução lateral $< \lambda/6$.
- Alta sensibilidade magnetoótica ($\sim 10^{-12}$ emu).
- Determinação da direção da magnetização

=> **Micromagnetismo experimental**

Novos projetos com o SNOM

- Litografia ótica de escrita direta
- Caracterização de Surface Plasmons
- Uso em fotoluminescencia, Raman e Magnetoótica

Corte transversal em fio de cabelo

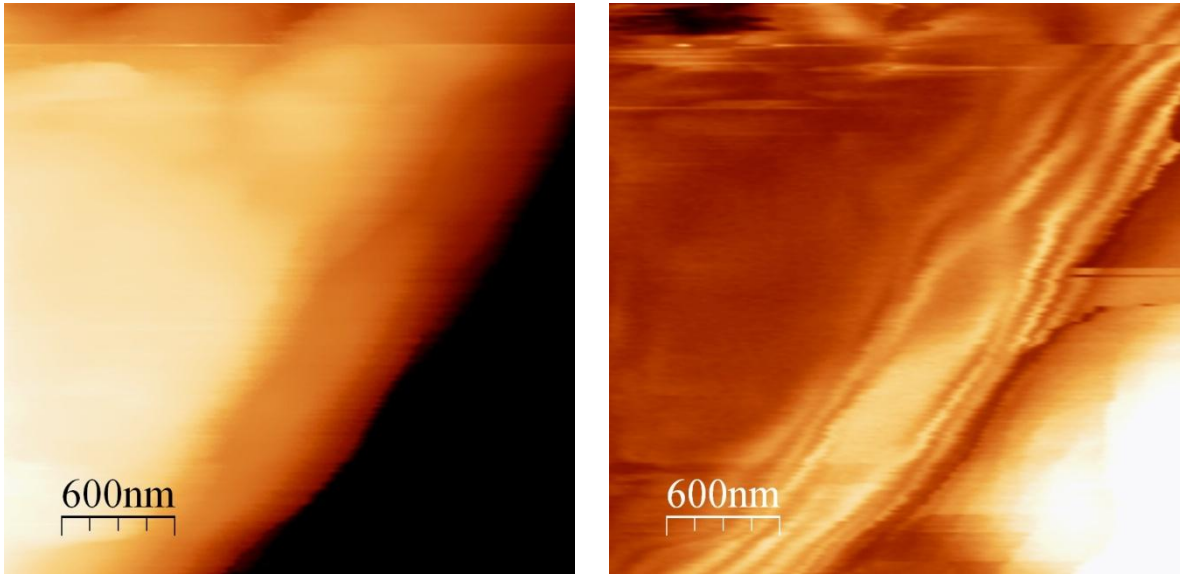

Resolução lateral
~ $\lambda/10$

Superresolução !!!

Uma pequena provocação !!!

Grupo do L. Novotny

SNOM + Plasmons de superfície + Confocal + Raman

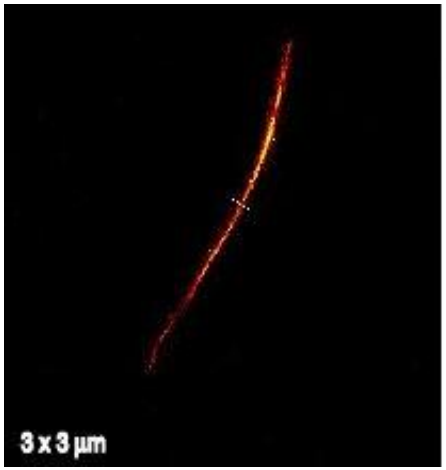

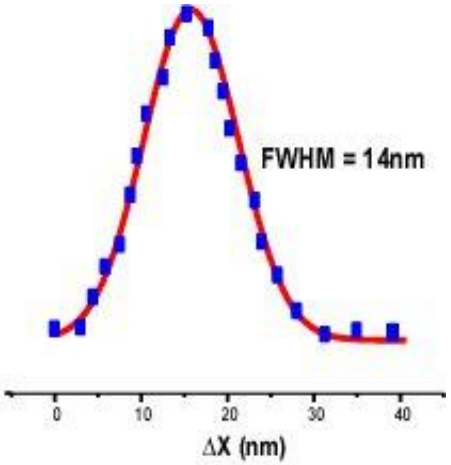

Resolução lateral
~ λ/50

Superresolução !!!

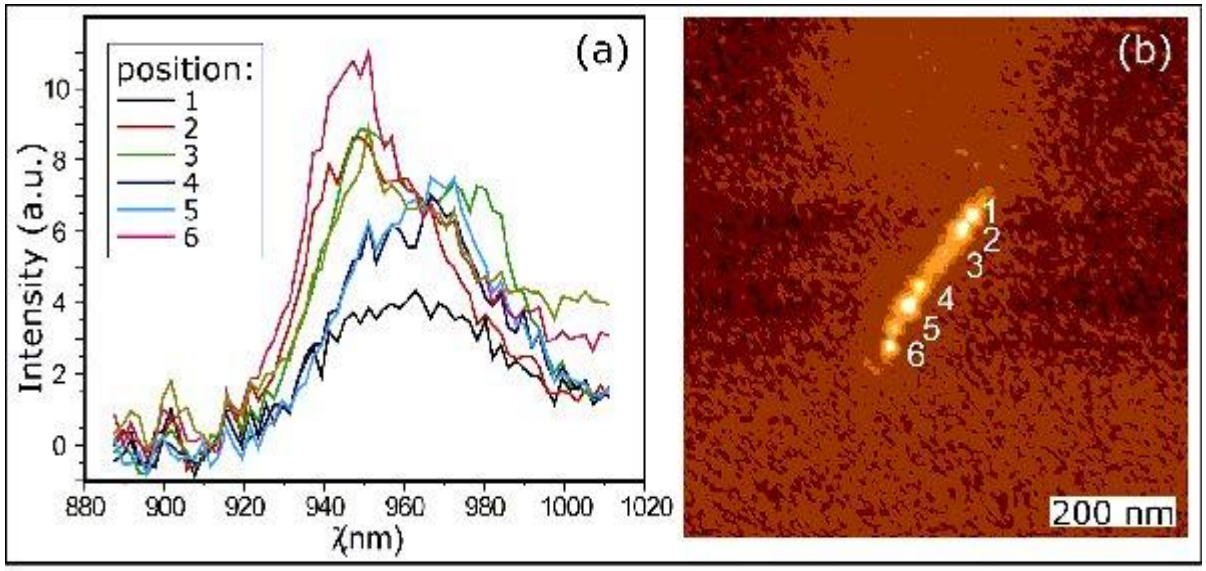

- Microscopia de tunelamento eletrônico

exemplos

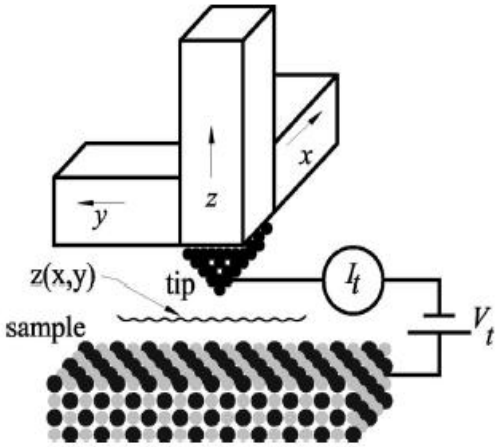

FIG. 2. A scanning tunneling microscope (schematic).

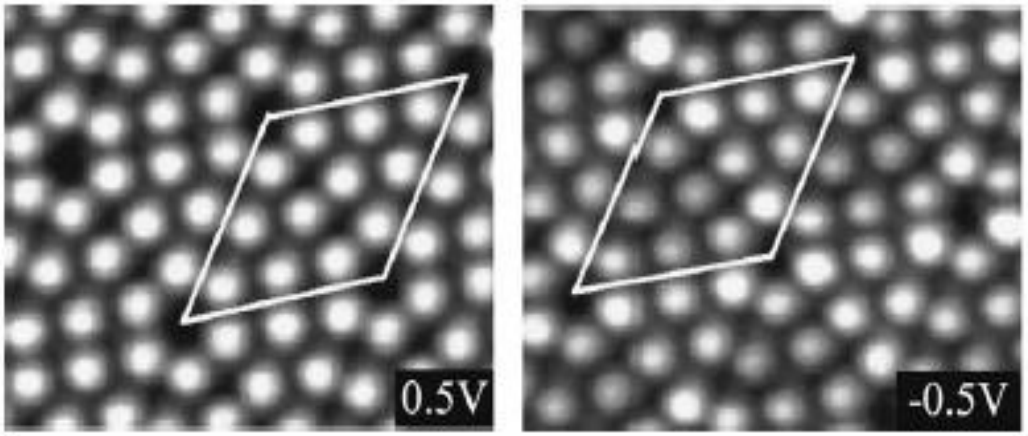

Figure 4. Atomically resolved STM images of the Si(111)7 × 7 surface. Bias voltage: +0.5 V (left), −0.5 V (right). A unit cell is outlined in the images, the size of the unit cell is 2.7 nm × 2.7 nm.

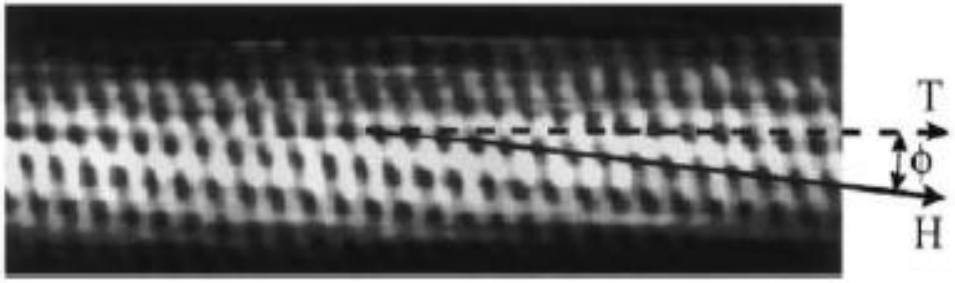

Figure 25. Atomically resolved STM image of individual single-walled carbon nanotubes. The lattice on the surface of the cylinders allows a clear identification of the tube chirality. Dashed arrows represent the tube axis T and the solid arrows indicate the direction of nearest-neighbour hexagon rows H. From the image, it can be determined that the tube has a chiral angle $\varphi = 7°$ and a diameter $d = 1.3$ nm. (From Ref. 53)

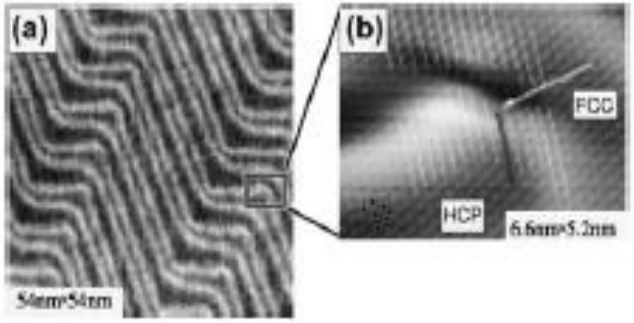

Figure 18. STM images of Au(111)-(23 × √3) surface. (a) "herringbone structure", image size: 54 nm × 54 nm. (b) atomic resolution image at the bending point (6.6 nm × 5.2 nm). (From Ref. 37)

Microscopia Eletrônica de Varredura e de Transmissão

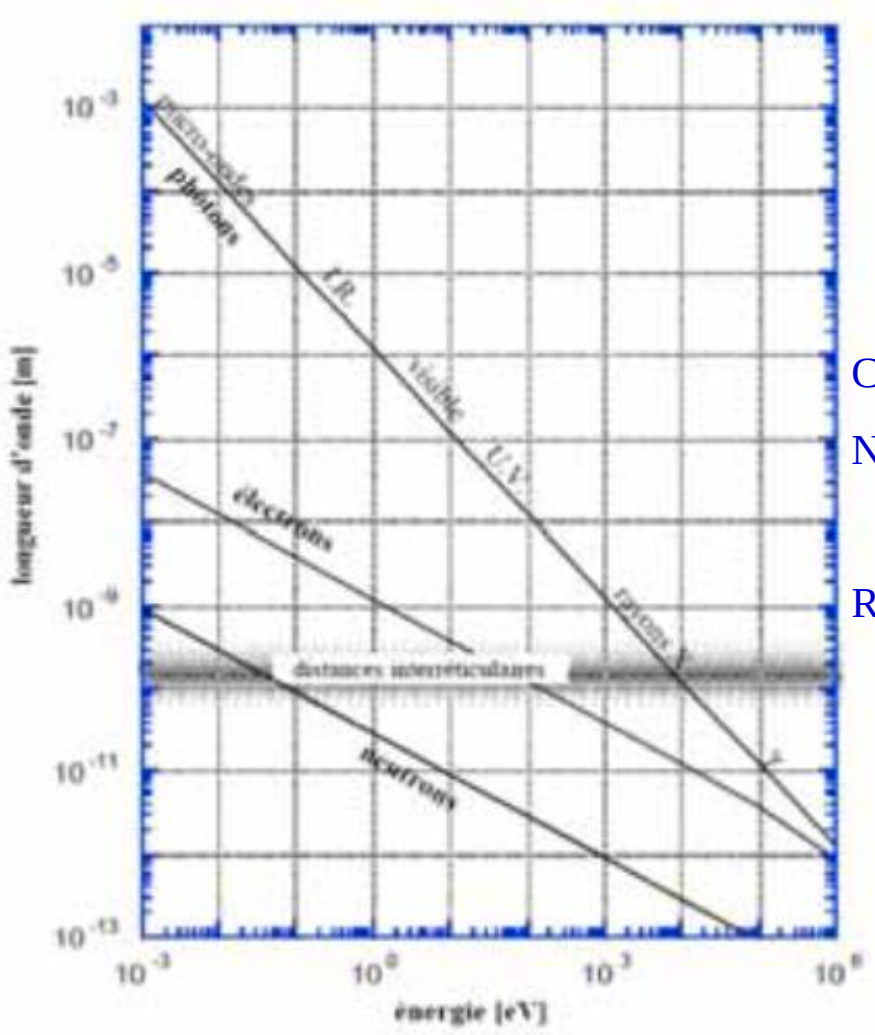

Comprimento de onda para radiação eletromagnética

Desde 10^{-14} m (raios ©) até ~km (rádiofrequência)

$$\lambda = hc / E$$

Comprimento de onda para partículas

Não relativístico

$$\lambda = h / p$$

Relativístico:

$$\lambda = h / \sqrt{2m_0 K(1 + K / 2E_0)}$$

E (eV)	λ (nm)
$1x10^6$	0,00122
$1x10^4$	0,0122
$1x10^2$	0,122
1	1,22

STM ⟶

- Resolução e superresolução ótica

O critério de Rayleigh estabelece para um microscópio ótico tradicional a resolução:

$$\Delta x > \frac{0,61\lambda}{n\sin\theta}$$

onde, λ é o comprimento de onda da radiação, n é o índice de refração do meio e θ é a semi-largura angular definida pela abertura da lente objetiva.

Considerando –se que o módulo do vetor de onda é dado por:

$$\left|\vec{k}\right| = n2\pi/\lambda$$

Sendo a variação da componente x do momento dada por:

$$\Delta p_x = \hbar 2n\sin\theta(2\pi/\lambda)$$

Assim, o critério de Rayleigh se assemelha ao Princípio da Incerteza:

$$\Delta x \Delta p_x > h$$

Como, para uma onda homogênea, todas as suas componentes de k serão inferiores ou iguais a $n2\pi/\lambda$.

Consequentemente, a resolução espacial em cada componente fica limitada ao critério de Rayleigh.

- Resolução e superresolução ótica

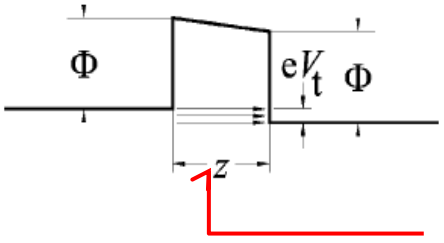

Mas, se tivermos a componente z da onda com carater evanescente, o valor da componente de k nesta direção será imaginário.

Assim, podemos escrever que: $k_x^2 + k_y^2 + k_z^2 = \left(n2\pi/\lambda\right)^2$

Com $k_z^2 < 0$

e $k_x^2 + k_y^2 > \left(n2\pi/\lambda\right)^2$

Portanto, Δp_x e Δp_y ↑

e Δx e Δy ↓

O que permite uma melhor resolução lateral !!!

(comparativamente ao que seria obtido com uma onda plana de mesmo comprimento de onda)

- Princípio da incerteza de Heisenberg

Como o critério de Rayleigh e o Princípio da incerteza de Heisenberg são formalmente semelhantes, esperamos o mesmo comportamento para a resolução de imagens construídas com elétrons.

Se os elétrons forem descritos por uma onda com uma componente evanescente, teremos uma resolução lateral melhor do que se trabalharmos com uma onda plana.

Esta condição é exatamente atendida na situação de tunelamento eletrônico.

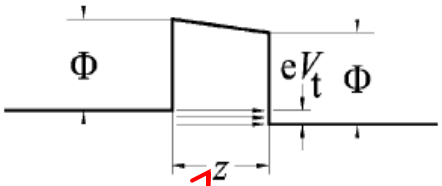

Onda evanescente

Vigoureux & Courjon, Appl. Opt., 31-16 (1992) 3170

STM e SNOM

- Trabalham com ondas evanescentes em uma direção, o que permite melhorar a resolução das imagens nas direções transversais.
- plasmons de superfície fornecem um importante mecanismo de amplificação de sinal ótico, permitindo a obtenção de imagens com alta qualidade e melhor resolução lateral.

==> NOVAS METODOLOGIAS !

(como Raman, fotoluminescência, magnetoótica, litografia, etc, podem explorar este potencial)

O Princípio da Incerteza precisa ser adequadamente interpretado na presença do tunelamento eletrônico !